

**Skoltech**

Skolkovo Institute of Science and Technology

Skolkovo Institute of Science and Technology

DEVELOPMENT OF CORE-SHELL FIBER COMPOSITE BASED ON POLYVINYL  
ALCOHOL MODIFIED WITH GRAPHENE OXIDE AND SILICA FOR  
BIOMEDICAL APPLICATIONS

*Doctoral Thesis*

by

YULIYA  
KAN

DOCTORAL PROGRAM IN MATERIALS SCIENCE AND ENGINEERING

Supervisor  
Professor Alexander M. Korsunsky

Moscow - 2022

© Yuliya Kan 2022

I hereby declare that the work presented in this thesis was carried out by myself at Skolkovo Institute of Science and Technology, Moscow, except where due acknowledgement is made, and has not been submitted for any other degree.

Candidate (Yuliya Kan)

Supervisor (Prof. Alexander M.  
Korsunsky)

## Abstract

Coaxial electrospinning is a versatile solution in the field of tissue engineering and drug delivery systems. An inherent feature of technology is the availability of commercial installations and the production of polymer fibers with varied dimensions and compositions. The obtained fibers could be implemented for the production of textile composites.

Polyvinyl alcohol (PVA) has the reproducible fiber ability and intrinsic properties such as biocompatibility and non-toxicity of decomposition products under physiological conditions. The main issue of PVA fibers is fast hydrolytic degradation that is suggested to control with the structure modifications.

This thesis is dedicated to the investigation of coaxial fiber composite, considering the impacts of silicon dioxide nanoparticles, graphene oxide (GO) as modifying additives and the polymer blend of PVA and polyethylene glycol (PEG). During the study, the working parameters of synthesis were developed to receive the continuous fibers with nanoscale dimensions. The produced fibers were characterized with the electron and fluorescent confocal microscopy to observe the fiber diameter and core-shell structure.

The silicon dioxide nanoparticles as codelivery vehicles are uniformly integrated in the multicomponent PVA-PEG-SiO<sub>2</sub> core fiber by the optimization of the PEG ratio. The crosslinking effect of nanoparticles by newly formed bonds were detected with the Fourier-transform spectroscopy. The effect of silica incorporation results in the reduced fiber diameter compared with the PVA-PEG blend. Due to the rapid dissociation of hydrophilic

core compound in an aqueous medium a protective shell based on graphene oxide is introduced.

Graphene oxide changes the physical properties of the composite including water uptake, resistance to the tensile strength. This component alters the matrix permeability for solvent molecules due to the increased swelling capacity and a hydrogel formation. The mechanical properties of the polymer matrix are improved by the presence of interactions between the oxygen containing groups of graphene oxide and the hydroxyl groups of PVA. Notably, the addition of GO facilitates the fiber formation with a smaller dimension compared to a base polymer. Hence, the modification with GO crucially contributes the features of core-shell fiber composite.

The effect of modifying additives is accompanied by a study of pharmacokinetics for the produced textiles loaded with medical agents. The ability of separate encapsulation is proved by the fluorescent labeling of core and shell compounds. In vitro studies demonstrate the release behavior of the antibacterial agents, antibiotics and fluorescent dyes placed in the core of coaxial fibers. The absorption properties of PVA-GO shell are performed by the removal of the fluorescent dye after the full dissolution of the fiber. The efficiency of dye absorption allows to broaden a method of targeted delivery with subsequent purification of the medium from dyes.

The GO assisted crosslinking helps to change the dissolution mechanisms of PVA originated fiber mat. High water uptake of GO accelerates the transfer from the glassy polymer fiber to a hydrogel. This transformation massively affects the nature of drug immobilization resulting in the prolonged release time. Higuchi and Korsmeyer – Peppas

mathematical models are found to be the optimal to describe the release mechanisms. The core-shell fibers show the release of drug governed by the non-Fickian mechanism, defining the rate of polymer relaxation relatively to molecule diffusions. While the GO-based hydrogel degrades slower to prolong the diffusion of drug in the medium.

The obtained results provide the deep understanding of the correlations between the fabrication parameters and nano additives, which interactions occur in the composition, affecting the fiber morphology, degradation and release kinetics of Chlorhexidine, Doxorubicin as a model of drug. This work concludes the feasibility of fiber technologies in the field of biodegradable drug loading composites. Findings of this research provide the information for the further exploration and a sustainable design of the medicated fiber fabrication.

## Publications

1. [Under Review] German, S. V.; Abalymov, A. A.; Kurochkin, M. A.; **Kan, Y.**; Gorin, D. A.; Novoselova, M. V. Plug-and-Play Lymph Node-on-Chip: Metastasis Modeling By Combination Of Cell Spheroid, Collagen Sponge and T-cells. *International Journal of Molecular Sciences* 2022, 23, doi: 10.3390/xxxxx.
2. **Kan, Y.**; Bondareva, J. V.; Statnik, E. S.; Cvjetinovic, J.; Lipovskikh, S.; Abdurashitov, A. S.; Kirsanova, M. A.; Sukhorukhov, G. B.; Evlashin, S. A.; Salimon, A. I.; Korsunsky, A. M. Effect of Graphene Oxide and Nanosilica Modifications on Electrospun Core-Shell PVA–PEG–SiO<sub>2</sub>@PVA–GO Fiber Mats. *Nanomaterials* **2022**, *12*, 6. doi: [10.3390/NANO12060998](https://doi.org/10.3390/NANO12060998).
3. **Kan, Y.**, Salimon, A. I., & Korsunsky, A. M. On the electrospinning of nanostructured collagen-PVA fiber mats. *Materials Today: Proceedings* **2020**, *33*, 2013–2019. doi: 10.1016/J.MATPR.2020.07.621.
4. **Kan, Y.**; Cvjetinovic, J.; Statnik, E. S.; Ryazantsev, S. V.; Anisimova, N. Y.; Kiselevskiy, M. V.; Salimon, A. I.; Maksimkin, A. V.; Korsunsky, A. M. The fabrication and characterization of bioengineered ultra-high molecular weight polyethylene-collagen-Hap hybrid bone-cartilage patch. *Materials Today Communications* **2020**, *24*. doi: 10.1016/J.MTCOMM.2020.101052.

## Conferences

1. [Talk] Kan, Y.; Statnik E. S.; Cvjetinovic J.; Salimon A. I.; Korsunsky A. M. Fibrous biomaterials for local drug delivery. Presentation. II International Scientific and Practical Conference Fundamental Science for Practical Medicine 2021. Additive Technologies, Modern Materials and Physical Methods in Medicine 2021, Moscow, Russia.
2. [Conference paper] **Kan, Y.**; Salimon A. I.; Korsunsky A. M. On the recent developments in electrospinning to produce hierarchically organized composites for separator membranes. *Proceedings of the Skoltech Energy PhD Seminar 2020/2021* **2020**, Moscow, Russia.
3. [Talk] **Kan, Y.**; Salimon A. I.; Korsunsky A. M. Piezoelectricity of Collagen Based Materials for Biomedical Applications. *Smart Nanomaterials Advances, Innovation and Applications* **2019**, Paris, France.
4. [Poster] **Kan, Y.**; Salimon A. I.; Korsunsky A. M. Piezoelectricity in hierarchical collagen-hydroxyapatite hybrid materials. *4th International school-conference of young scientists, Topical problems of modern electrochemistry and electrochemical materials science* **2019**, Moscow, Russia.
5. [Conference paper] **Kan, Y.**; Cvjetinovic, J.; Salimon, A. I.; Statnik, E. S.; Ryazantsev, S. V.; Korsunsky, A. M. Collagen-based Composite and Hybrid Bone Implant Materials: Structure and Property Characterization. *Lecture Notes in Engineering and Computer Science* **2019**, 2240, 356–364.

## **Acknowledgements**

I wish to acknowledge my supervisors Prof. Alexander M. Korsunsky and Dr. Alexei I. Salimon for the valuable mentorship and support. I also would like to express my gratitude to the staff, faculty and board of Skolkovo Institute of Science and Technology for the technical consultation and funding.

Special thanks to the specialists from BioImaging and Spectroscopy Core Facility, Advanced Imaging Core Facility located at Skolkovo Institute of Science and Technology for their involvement in this work.

## Table of Contents

Abstract.....	3
Publications.....	6
Conferences.....	7
Acknowledgements.....	8
Table of Contents.....	9
List of Symbols, Abbreviations.....	12
List of Figures.....	14
List of Tables.....	19
Chapter 1. Actuality and Problem Statement.....	20
Chapter 2. Literature Review.....	24
2.1 Electrospun polymer materials as a drug carrier system.....	24
2.2 The dissolution and degradation mechanism support drug release.....	34
2.3 Modifying agents of fiber mats.....	41
2.4 Crosslinking with Nanoflakes of GO.....	42
2.5 Crosslinking with Nanosized Silica.....	44
Chapter 3. Experimental section.....	47
3.1 Materials.....	47
3.2 Instruments and Fabrication Techniques of Core-Shell Fibers.....	47
3.3 Spinning solution preparation loaded with the drug.....	49
3.4 Electrospinning of the solutions.....	50
3.5 Patterning of fiber mat.....	51

3.6 Crosslinking of fiber mats with methanol.....	52
3.7 Dip-coating of films.....	52
3.8 Spinning solution characterization.....	52
3.9 Wettability and Water Uptake measurements.....	53
3.10 Morphology.....	53
3.11 Spectroscopic characterization.....	55
3.12 XRD .....	55
3.13 ToF-SIMS .....	56
3.14 Differential Scanning Calorimetry (DSC) .....	56
3.15 Micromechanical test.....	57
3.16 UV-Vis Spectral Analysis of Fiber Mats .....	58
3.17 Antibacterial test .....	60
3.18 Cell Viability Assay.....	60
3.19 Statistics .....	62
Chapter 4. Results .....	63
4.1 Viscosity and conductivity.....	63
4.2 Confocal Laser Fluorescence Microscopy .....	63
4.3 SEM .....	64
4.4 STEM and EDX.....	75
4.5 Contact angle and Fiber Diameter after Methanol Treatment .....	77
4.6 Raman Spectroscopy.....	80
4.7 FTIR spectroscopy .....	85

4.8 ToF-SIMS of Fiber Loaded with Drug .....	88
4.9 XRD .....	89
4.10 Differential Scanning Calorimetry (DSC) .....	91
4.11 Mechanical Tests .....	93
4.12 UV-Vis Spectral Analysis of Fiber Mats .....	96
4.13 Antibacterial Test.....	104
4.14 Cell Viability Assay .....	106
Chapter 5. Future Prospects .....	107
Chapter 6. Conclusion.....	110
Supplementary Materials .....	116
Bibliography .....	130

## **List of Symbols, Abbreviations**

BSE – Backscattered Electron (BSE) Mode

CHX – Chlorhexidine Gluconate

DCM – Dichloromethane

DIC – Digital Image Correlation

DMF – Dimethylformamide

DMSO – Dimethyl sulfoxide

DOX – Doxorubicin

DSC – Differential Scanning Calorimetry

EDX – Energy-Dispersive X-ray Analysis

FabLab – FabLab and Machine Shop Shared Facility

FAM – 5(6)-Carboxyfluorescein

FITC – Fluorescein Isothiocyanate

GO – Graphene Oxide

HAADF STEM – High-Angle Annular Dark-field Scanning Transmission Electron  
Microscopy

HA – Hydroxyapatite

HPMC – Hydroxypropyl-Methyl-Cellulose

ICG – Indocyanine Green

MB – Methylene Blue

NPs – Nanoparticles

PAA – Polyacrylic Acid

PBS – Phosphate-Buffered Saline

PCL – Polycaprolactone

PEG – Polyethylene Glycol

PEO – polyethylene oxide

PLGA – Poly (lactic-co-glycolic acid)

PLLA – Poly (L-lactic acid)

PVA – Polyvinyl Alcohol

PVA-PEG-SiO<sub>2</sub>@PVA-GO-1x CHX – *core-shell fiber composite derived from PVA, PEG, GO with CHX loading in the precursor solution (10 mg/mL)*

PVC – Polyvinyl Chloride

PVDF – Polyvinylidene Fluoride

PVP – Polyvinylpyrrolidone

PVP-I – polyvinylpyrrolidone-iodine complex

rGO – reduced Graphene Oxide

Rh B – Rhodamine B

SEM – Scanning Electron Microscopy

TEM – Transmission Electron Microscopy

TEOS – Tetraethyl Orthosilicate

ToF-SIMS – Time-of-Flight Secondary Ion Mass Spectrometry

XRD – X-ray Diffraction

## List of Figures

Figure 1. The representation of laboratory setup of electrospinning .....	48
Figure 2. Representative fluorescence microscopy images collected from (a) core-shell PVA-PEG-SiO <sub>2</sub> @PVA-GO fibers with the labeled core-shell structure; (b) green core labeled with FAM; (c) red shell labeled with Rh B .....	64
Figure 3. SEM imaging of fibers: (a) pristine PVA; (b) PVA-PEG core; (c) PVA-PEG-SiO <sub>2</sub> core; (d) shell PVA-GO 10%; (e) core-shell PVA-PEG@PVA-GO); and (f) core-shell PVA-PEG-SiO <sub>2</sub> @PVA-GO .....	68
Figure 4. SEM imaging of crosslinked fibers with methanol: (a) pristine PVA; (b) PVA-PEG core; (c) PVA-PEG-SiO <sub>2</sub> core; (d) shell PVA-GO; (e) core-shell PVA-PEG@PVA-GO); and (f) core-shell PVA-PEG-SiO <sub>2</sub> @PVA-GO .....	70
Figure 5. SEM images of (a) core fiber PVA-PEG-SiO <sub>2</sub> -CHX; (b) core-shell PVA-PEG-SiO <sub>2</sub> @PVA-GO-CHX fibers; and after dip-coating with PHB: (c),(d) methanol crosslinked core-shell CHX fibers .....	72
Figure 6. SEM imaging of as-received, crosslinked and soaked fiber mats after the incubated in water medium for 2 h .....	74
Figure 7. HAADF-STEM images of (a) PVA-PEG-SiO <sub>2</sub> with PVA:PEG (90:10); (b,c) PVA-PEG-SiO <sub>2</sub> with PVA:PEG (70:30); (d) EDX analysis of PVA-PEG-SiO <sub>2</sub> with PVA:PEG (90:10) with compositional mapping of O, Si, and C elements .....	76
Figure 8. The contact angle of (a) as-received fibers and (b) methanol crosslinked fiber mats; (c) water uptake of shell PVA-GO 10% and core-shell fibers; (d) electrospinning efficiency.....	79

Figure 9. Raman spectra of PVA-based and GO-derived fiber mats in the range of 200 – 3400 $\text{cm}^{-1}$ .....	81
Figure 10. Raman spectroscopy of the synthesized core fiber PVA-PEG-SiO <sub>2</sub> and the constituents of spinning solutions in the range of 200–3400 $\text{cm}^{-1}$ .....	84
Figure 11. FTIR spectra of the fiber mats: <b>(a)</b> PVA 10 wt.% fiber; <b>(b)</b> shell PVA-GO; <b>(c)</b> core PVA-PEG-SiO <sub>2</sub> ; <b>(d)</b> core-shell PVA-PEG-SiO <sub>2</sub> @PVA-GO; <b>(e)</b> PVA-PEG-SiO <sub>2</sub> @PVA-GO-1x CHX .....	86
Figure 12. ToF-SIMS spectra obtained in the negative ion mode of core-shell PVA-PEG-SiO <sub>2</sub> @PVA-GO (a); core fibers PVA-PEG-SiO <sub>2</sub> -1x CHX loaded with CHX (b); core-shell PVA-PEG-SiO <sub>2</sub> @PVA-GO-1x CHX (c); SEM image of ion beam-milled PVA-PEG-SiO <sub>2</sub> @PVA-GO sample(d) .....	88
Figure 13. XRD spectra of the components of <b>(a)</b> PVA powder; <b>(b)</b> PVA fiber; <b>(c)</b> core PVA-PEG-SiO <sub>2</sub> fiber; <b>(d)</b> shell PVA-GO fiber; <b>(e)</b> GO; <b>(f)</b> PEG powder; <b>(g)</b> Silica .....	90
Figure 14. DSC curves of samples with the following compositions: shell PVA-GO fiber mat; core PVA-PEG-SiO <sub>2</sub> fiber mat; core-shell PVA-PEG-SiO <sub>2</sub> @PVA-GO fiber mat ..	92
Figure 15. Core-shell fiber mat mounted in Deben device <b>(a)</b> ; stress-strain curves with the cross-sectional areas of fiber mats: PVA-GO shell <b>(b)</b> ; PVA-PEG-SiO <sub>2</sub> core <b>(c)</b> , PVA-PEG-SiO <sub>2</sub> @PVA-GO core-shell <b>(d)</b> .....	95
Figure 16. Fluorescence spectra excited with the different sources for the shell PVA-GO 5 % fibers <b>(a)</b> ; shell PVA-GO 10 % <b>(b)</b> ; core-shell PVA-PEG-SiO <sub>2</sub> @PVA-GO <b>(c)</b> ; crosslinked core-shell PVA-PEG-SiO <sub>2</sub> @PVA-GO <b>(d)</b> .....	97

Figure 18. Absorbance spectra of core, core-shell, methanol crosslinked core-shell fiber loaded with CHX .....	99
Figure 19. Loading efficiency of PVA-PEG-SiO <sub>2</sub> @PVA-GO core-shell with the initial loading of CHX in the core <b>(a)</b> ; Encapsulation efficiency of PVA-PEG-SiO <sub>2</sub> @PVA-GO-1x CHX against PVA-PEG@PVA-GO-1x CHX core-shell fibers .....	100
Figure 20. CHX release of PVA-PEG-SiO <sub>2</sub> @PVA-GO-1x CHX fitted to <b>(a)</b> Zero Order; <b>(b)</b> First Order; <b>(c)</b> Higuchi model; <b>(d)</b> Korsmeyer – Peppas model .....	101
Figure 21. CHX release of PVA-PEG @PVA-GO-1x CHX core-shell fibers fitted to <b>(a)</b> Zero Order; <b>(b)</b> First Order; <b>(c)</b> Higuchi model; <b>(d)</b> Korsmeyer – Peppas model .....	102
Figure 22. Disc diffusion assay of core-shell fibers PVA-PEG-SiO <sub>2</sub> @PVA-GO (C-); PVA-PEG-SiO <sub>2</sub> @PVA-GO-1x CHX (S1, S2); PVA-PEG@PVA-GO-1x CHX (P); cellulose disk (C0); cellulose control with doxycycline (C+) against <i>S. aureus</i> .....	104
Figure 23. Cell viability assay of PVA-PEG-SiO <sub>2</sub> @PVA-GO core-shell fibers (CHF) and methanol crosslinked core-shell fiber mats (MCHF).....	106
Figure 24. Interaction mechanisms within electrospun fibers. ....	112
Figure S1. Dependence of the tip-to-target distance and mean diameter of PVA fibers	119
Figure S2. Dependence of PVA-PEG-SiO <sub>2</sub> core composition and mean diameter of fiber .....	119
Figure S3. Dependence of tip-to-target distance and mean diameter of the PVA-PEG-SiO <sub>2</sub> @PVA-GO core-shell fiber.....	120

Figure S4. SEM imaging of patterned fiber mat core-shell fibers: <b>(a)</b> , <b>(b)</b> etched pattern on Si wafer; <b>(c)</b> patterned fiber mat; <b>(d)</b> laser ablated aluminum plate; <b>(e)</b> patterned fiber basket mat .....	120
Figure S5. HAADF-STEM images of PVA-PEG-SiO <sub>2</sub> with PVA to PEG (90:10) ratios .....	121
Figure S6. Calibration curve of CHX in the medium of 0.01 M PBS (pH 7.4).....	121
Figure S7. Calibration curve of GO in the medium of 0.01 M PBS (pH 7.4) .....	122
Figure S8. Calibration curve of DOX in the medium of 0.01 M PBS (pH 7.4) .....	122
Figure S9. Calibration curve of MB in the medium of 0.01 M PBS (pH 7.4).....	122
Figure S10. Calibration curve of ICG in the medium of 0.01 M PBS (pH 7.4).....	123
Figure S11. CHX release of PVA-PEG-SiO <sub>2</sub> -0.1x CHX core fiber and PVA-PEG-SiO <sub>2</sub> @PVA-GO-0.1x CHX core-shell fiber in the medium of 0.01 M PBS (pH 7.4): <b>(a)</b> Zero Order; <b>(b)</b> First Order; <b>(c)</b> Higuchi; <b>(d)</b> Korsmeyer – Peppas models.....	123
Figure S12. GO release of PVA-PEG-SiO <sub>2</sub> @PVA-GO core-shell fibers fitted to: <b>(a)</b> Zero Order; <b>(b)</b> First Order; <b>(c)</b> Higuchi model; <b>(d)</b> Korsmeyer – Peppas model .....	124
Figure S13 Antibacterial activity of CHX loaded core-shell PVA-PEG-SiO <sub>2</sub> @PVA-GO with concentration (0.1x, 1x) .....	125
Figure S14. Absorbent property of GO observed in the core-shell fibers loaded with ICG <b>(a)</b> ; fluorescent label MB <b>(b)</b> .....	125
Figure S15. DOX release of core-shell DOX fiber mats during 22 h.....	126
Figure S16. DOX release of core-shell fibers fitted to the models: <b>(a)</b> Zero Order; <b>(b)</b> First Order; <b>(c)</b> Higuchi model; <b>(d)</b> Korsmeyer – Peppas model .....	127

Figure S17. CHX release of dip-coated crosslinked core-shell fibers fitted to the models:

**(a)** Zero Order; **(b)** First Order; **(c)** Higuchi model; **(d)** Korsmeyer – Peppas model.... 128

## List of Tables

Table 1 Drug Release Models.....	34
Table 2. Release exponent defines the drug release mechanisms.....	37
Table 3 The list of spinning solutions.....	49
Table 4 The characterization of solutions.....	63
Table 5. The contact angle of PVA-GO 5%, PVA-GO 10%, and PVA-PEG-SiO <sub>2</sub> @PVA-GO before and after crosslinking.....	78
Table 6. Raman bands assignments of GO, PVA, PEG, CHX, SiO <sub>2</sub> .....	82
Table 7 FTIR bands attributed to the silica, graphene oxide and PVA .....	87
Table 8. Diffraction peaks of fibers and components.....	91
Table 9. Degree of crystallinity and melting temperature of fiber mats.....	92
Table 10. The tensile properties of PVA-PEG-SiO <sub>2</sub> @PVA-GO, PVA-PEG-SiO <sub>2</sub> (core), and PVA-GO (shell) fibers .....	93
Table 11 Release mechanisms of medicated nanofibers.....	101
Table S1. The reference table of PVA-derived compositions of fibers.....	116
Table S2 Release mechanisms of medicated nanofibers .....	128

## Chapter 1. Actuality and Problem Statement

Electrospinning is a robust and versatile method of fiber fabrication with a wide range of operational parameters. This method implements an electrostatic force to elongate the polymer solutions from the drop into the continuous fiber. The conventional setup consists of a high voltage power supply, a syringe pump, a conductive capillary spinneret, and a target for fiber collection. The high variability of setup modifications and spinning solutions diversifies the method. The operational parameters include *a fiber target with different topography, a tip-to-target distance and applied voltage of power supply, spinneret nozzle, and flow rate of spinning solution* [1]. To support stable fiber fabrication, the value of electrostatic force must prevail the surface tension of spinning solutions to form a Taylor cone. Accordingly, the characteristics of spinning solutions based on the *chemical composition, molecular weight, concentration, and conductivity* diversify the synthesis of products. The concentration of spinning solutions affects the viscosity that directly relates to the fiber *diameter, morphology and spinnability* [2]. The fiber properties depend on the various polymers, which differ in their biodegradability, hydrophobicity, and solubility [3], [4], [5]. The broad functionality of produced fiber composites is reported in the biomaterials field. The Chapter 2 explores the features of fiber composites derived from polymers and nanomaterials.

With the development of electrospinning, a coaxial spinneret is discovered owing to the encapsulation ability of the specified agents within the polymer core-shell structure [6], [7], [8]. The advantage of coaxial approach is to combine the polymers with different solubility in organic solvents and water. The availability of solvents broadens the area of

applications by loading the drug with poor solubility [9], small molecule drugs [10], proteins, and nucleic acids [11]. Along with this, the drug release of system could be controlled by the diffusion mechanism of the selected polymer for electrospinning [12].

Various aspects of electrospinning technology impede the investigation of nonwoven materials that could be considered as a reliable carrier for medical cases such as transdermal and oral drug administration. The abundance of polymers and excipients directly affects the rate of decomposition of fiber composites with the induced drug release. The electrospinning supports the composite engineering from a monolithic fiber to the layered coatings with the intricate design. The purpose of this work is to characterize electrospun materials in the scope of the fabrication parameters and the product characterization; to identify the *in vitro* pharmacokinetics of a core-shell fiber mat.

Addressed to the degradability issue, an aim of this work is to define the correlation between the fiber parameters such as a diameter, wettability, chemical composition and measured dissolution profiles. The findings of this study contribute to the understanding of developed composite in terms of the existing demand for new drug delivery systems [13]. In this work the coaxial electrospinning was used to build the layered structure of fiber composite. Fabrication route includes the stages of design, manufacturing, testing and data analysis for several compositions. This thesis implements the different characterization methods to observe the electrospun composite as the hierarchically organized material. The route of research was organized based on the experimental observations included in the Supplementary Materials and reviewing the relevant works. The availability of synthetic polymers covers the vast areas of application oriented to the textile and composite

technologies. Considering the actual studies, this thesis aimed to investigate the hydrophilic fiber composite as a medicated fiber mat with the hydrogel transitions.

The development of electrospun fiber composites is oriented to renovate the approaches of wound treatment. There are several long-healing cases associated with problems of bacterial contamination, minimization of surgical interventions that take into account approaches to encapsulation of drugs, biodegradation and moisture permeability.

One of the long-healing cases is a diabetic ulcer that relates with the risks of high bacterial infection accompanying the biofilm formation [14]. Diabetic ulcer, burns and periprosthetic infections tend to the formation of hard-to-treat biofilm. The hyperglycemic environment facilitates the bacteria colonization and damage of the vascular network that prevents repair of diabetic wounds.

Hence, the wound dressing should perform antibacterial activity to support the healing. Biodegradation of coating is aimed to treat the inflammatory stages avoiding the change of bandage and keep the optimal conditions for healing. A change of wound dressings is an invasive procedure that leads to the scar formation during the tissue remodeling. The constant detachment of dressing causes the risk of damage and inflammation that facilitates long healing in the presence of metabolic disorders.

Moisture regulation is an important feature for healing while the exudate is produced during the healing. The balanced level of moisture supports the migration and growth of epithelial cells in the wound bed rather than in the dried condition [15]. Considering this issue, the hydrogel is a promising approach to retain the hydration of wound bed. Chen et al. introduced the PEG-based hydrogel preventing the bacterial

contamination of wound, where encapsulated angiogenetic drug provided the angiogenesis [16]. One of commercial solutions is a nonwoven fiber dressing Exufiber® on the base of Carboxymethyl cellulose using the hydrogel technology to prevent the bacterial propagation in the wound [17].

Abundance of spinnable polymers leverages the development of fiber composites for wound dressings. Hydrophilic polymers such as polyvinyl alcohol (PVA), polyethylene glycol (PEG) are considered for this application due to the ability to retain the moisture, biodegradation and non-toxicity [18]. PVA shows a high potential to promote cell growth and travel that is required for wound healing [19]. Among these features, the synthetic polymers are reproducible to form the numerous compositions of fiber textiles.

In the relevant study, Wen et al. suggested a hydrophilic core-shell fiber composite with the anti-inflammatory function [20]. In the research by Kataria et al., PVA based nanofiber composite with sodium alginate provide the sustainable drug release and in vivo studies performed better regeneration compared with the pure PVA fibers [21].

In this thesis electrospun hydrophilic fiber composite were considered for the antibacterial application. The strategy of core-shell fiber supports drug encapsulation and the transfer to hydrogel after the contact with the moisture. Fiber-hydrogel composite equipped with antibacterial agent is a feasible approach for wound dressing materials.

## Chapter 2. Literature Review

### 2.1 Electrospun polymer materials as a drug carrier system

Previously mentioned in the introduction, the increasing abundance of fibrous biomaterials relates to the wide range of ‘spinnable’ biocompatible polymers that serve as a framework for nonwoven composites. The main advantage of using biodegradable polymers is to deliver a less invasive therapy to patients by the electrospun drug carrier systems, due to their safe decomposition products under the physiological conditions [22–24]. The biocompatible polymers PVA, PCL, PLA, PVP are considered for the fabrication of the fiber films in wound dressing, drug carrier systems and tissue engineering fields. In this work the main focus is the polyvinyl alcohol (PVA) derived composites. The examples of composites are collected in Supplementary Materials, Table S1, with the main operational parameters of spinning included.

PVA  $[\text{CH}_2\text{CHOH}]_n$  is known as a base for the nanofiber composites where the miscibility and high repetitive spinnability introduced in the following studies [25–27]. This linear water-soluble polymer is suitable for building composites with medical applications such as rapid drug delivery systems [12], [28], wound dressings [29], and scaffolds for tissue engineering [30], [31] and functional coatings.

Among the vast application area of biomaterials, the surgical wound dressings are optimal for the electrospun nonwoven mats due to the requirements to treat large areas of injuries and sutures against bacterial adhesion and infections. The fiber mats are considered robust wound dressing materials that could be used for medicated antibacterial [24], disinfecting [32], and cancer treatments [28]. A variety of drugs including antibiotics,

enzymes, growth factors, and anticancer drugs could be loaded into electrospun nanofibers for the specified remedies [33], [34], [35]. For instance, the miscibility of PVA-based spinning solutions was investigated to build the oral nanocarrier system with poor-soluble drugs [33], [34]. As a model of poor water-soluble and pH sensitive drug, valsartan in PVA fibers demonstrated pH independent release of drug over the PVP and hydroxypropyl-methyl-cellulose (HPMC) fiber carriers [36]. Apart from this application, the fiber mat is considered as a potential scaffold for tissue engineering to treat the nerve diseases [37], cardiac implants [38] that should mimic the morphology and biochemical composition close to the genuine extracellular matrix. The fibers on the base of natural polymers such as silk and collagen and chitin are investigated in terms of tissue engineering. The diverse cases of applications are angiogenic, cardiovascular and bone tissues promoting the growth of ventricular cardiomyocytes, human dermal fibroblasts, osteoblasts, human vascular smooth muscle and mesenchymal stem cells [39], [40], [41], [42]. The approach of green electrospinning received the recognition that focused on the hydrogel forming and water uptake capacity of the electrospun fibers made of natural polymer [43].

Despite the biochemical relevance and demand, the natural polymers have some limitations such as low mechanical strength, low temperature of degradation, resulting into the drug loading incompatibility. These factors impede the fabrication and functionality of composites from natural origin. The synthetic polymer meshes including PVA as a binder encompass the bioactive properties of collagen and biodegradable polymer in the collagen-PVA composite [44]. Some of the commercialized polymeric grafts such as polyvinyl caprolactam-polyvinyl acetate-polyethylene glycol (Soluplus®) [45] is considered as a

hydrophilic base of oral drug loading system for the hydrophobic anti-inflammatory medicine. *Pisani et al.* noted the influence of polymer concentration on the fiber diameter and importance of nanosized fibers for the tableted form of drug loading [46]. To pursue the better drug dissolution, the preference was given to the nanoscale fibers due to the higher surface area and better contact with the environment. The tablet produced from the electrospun fibers with the size of  $330 \pm 140$  nm showed faster immobilization of drug compared with the commercial example Mobic® for 2 h in the varied pH conditions (1.0, 4.5, 6.7, 7.5). Hence, another application of hydrophilic polymer fibers follows to control the drug solubility by the select of certain pH conditions [47]. The hydrophilic polymers are involved in the numerous studies dedicated to the oral administration [46,47] and ocular healing techniques due to the required fast dissolution rate for these lesions of treatment [48,49].

Another application of the artificial polymers arises as the bone tissue regenerative materials [50–52] heart valve prosthesis [53], [54], tendons [55], vascular grafts [56] and drug delivery vehicles [6], [8], [12], [28]. The insightful concept of the layered composite suggests the combination of PLGA fiber coating and collagen-hydroxyapatite fiber mat as a bone tissue engineering scaffold [52]. Another synthetic polymer blend is recognized as a wound healing remedy, where PEG serves an outer shell of the three-layered fiber composites (PVP, PCL, PEG) loaded with antibiotic, metronidazole [57]. The wettability of PEG shell is well noted as a remedy reducing the contamination of wound and moisture regulation by the gel coating. The tissue engineering substrate could be enriched with the

drug to induce the cell growth. The enhanced therapeutical functionality is a solution applicable for the wound dressings and suture materials [50–57].

Hydrophilic and hydrophobic polymer combinations of collagen and PCL help to provide the sustained drug release of the transdermal patch to treat the wound lesions [58]. The swelling capacity of the fibers was observed to trace the effect of medium and polymers on the dissolution of drug. The PCL-collagen nanofiber samples with the higher ratio of PCL (9:1) showed the decreased swelling ability and weight loss after the incubation in PBS for 24 h in room temperature and demonstrated the prolonged drug immobilization.

Considering these studies, the artificial polymers have the potentials as the tunable components among a variety of biocompatible composites. The referenced study [55] suggests the PCL/cellulose acetate fiber functionalized with the insulin-like growth factor-1 (IGF-1). This composite is introduced as the tendon engineering scaffold. The scaffold seeded with the mesenchymal stem cells (MSC) was used to treat the Achilles tendon of rat. The proliferation of mesenchymal stem cells demonstrated good cell attachment to the scaffold. The IGF-1 and insulin are known as the growth factors that initiate the tendon phenotypic development of MSC within the polymer scaffold [59]. The comprehensive assessment of the fiber composite demonstrated the prudent integration of the growth factor immobilization in the tissue engineering field.

The rich fiber morphology and physical properties as a tensile strength are important in terms of cell engineering. The cell attachment and processes related with the living cells such as proliferation, differentiation correlate with the porosity, fiber dimension

and mechanical properties of scaffold. A lot of studies point out the dependence between fiber orientation, surface topology for the formation of seeded cells [60–66]. These parameters are under the studies in terms of the high applicability of fiber composites.

The mentioned synthetic polymer composites provide the opportunity to include the different drugs dissolved with the corresponding organic solvents such as chloroform, dimethylformamide (DMF), or the deionized water for hydrophilic PVA and PEG. PVA-based fiber blends are conventional hydrophilic composition, that is applicable in the scope of the wound-healing, antibacterial, anti-scarring material [8,12,48,67,68]. PVA operates as a binder, providing the repetitive electrospinning as productive as for the pure PVA, and for the polymer blends. The numerous nonwoven biomaterials could be synthesized from the polymer PVA dissolved in the deionized water under heating up to 80 °C. The spinning solutions of PVA have the high miscibility due to –OH groups that expands the variety of composites and encapsulation of drugs. In the next studies the several polymer meshes such as PVA-PEG [69], PVA-PCL [70], and PVA-PHB [71] were introduced for the fiber formation. In the case when the additional component is the nanomaterial presented in the powder of flakes, the blend could be easily prepared with help of a PVA base solution.

Various protocols of substance encapsulation are available for the PVA-based drug carrier systems manufactured by the coaxial electrospinning [8,72]. The coaxial method allows to combine of the different types of polymers and nanomaterials in one fiber. The following advantages of coaxial spinning were discussed in the referenced study [48], where the separate encapsulation of medicines was delivered in the bilayer fiber with the

release of anti-scarring pirfenidone from the PLGA outer shell and an antibiotic moxifloxacin HCl from the PVP core.

A highly effective non-antibiotic, antiseptic chlorhexidine (CHX) is used as a drug model in wound dressing studies that could easily be dissolved in the spinning solutions and monitored with spectroscopic techniques. It is well adapted to treat the wound lesions due to its bactericidal and bacteriostatic properties. Hydrophilic drugs like chlorhexidine are effectively encapsulated within polymer fibers including PVA [73], [74]. Despite its widespread this drug is still on demand due to its availability and easy to operate. Actual referenced studies claim the applicability of CHX to treat burns and healing of human gingival tissues [75],[76].

Doxorubicin is actively used in the cancer therapy and could be dissolved with the distilled water [77]. The challenge of the cancer treatment is to reduce its toxic influence on the health lesions. The electrospun materials received the recognition by arranging the effect of medicine in the limited locality. Some works conduct the study dedicated to this area of application. For instance, there are the PVA, PLGA, PVP derived nonwoven fibers considered as robust vehicles for chemotherapy [28], [78], [79].

Hydroxyl groups of PVA are responsible for the strong interaction with the modifying components such as nanoparticles produced by the inter- and intramolecular hydrogen bonding [80], [81]. PVA is easily dissolved with deionized water but it is quite stable in organic solvents. To alter the water degradation of PVA materials, the various modifying protocols were suggested.

The referenced study [25] demonstrated the water absorption and swelling behavior of PVA films with the molecular weight of PVA starting from 13,000 – 124,000 g/mol. After the crosslinked and non-crosslinked samples were stored in the distilled water for 2 h, the swelling capacity of films were compared. The crosslinking protocol with citric acid efficiently reduced swelling capacity of PVA films in two times. The analgesic complex of agents was loaded in the PVA films to monitor the drug kinetics for 4 h. The film of PVA with molecular weight 84,000-124,000 g/mol immobilized the 80 % of agent after 4 h in the distilled water. Compared with as-received samples, the crosslinked ones showed an increased release rate of encapsulated drug due to the reduced number of – OH bonds providing the interaction of drug within the polymer matrix. The mentioned study claimed that the different molecular weight of PVA films did not affect the drug release, whereas the chemical crosslinking promoted the sustained one.

The chemical and physical crosslinking are aimed not only affect the pharmacokinetics but to strengthen the produced fiber by means of strong intramolecular or intermolecular interactions within the structure [82]. Crosslinking of polymer could be divided in intramolecular and intermolecular types organized by the same molecules and opposite ones, respectively. In the case of PVA, the physical crosslinking occurs via hydrogen bonds between hydroxyl groups or covalent bonds for chemical crosslinking. There are several conventional methods of physical crosslinking known as the thermal treatment [77] and methanol vapor treatment and freeze-thawing [82–84]. For the chemical crosslinking, the functional groups of the polymer are stabilized in the presence of modifying agents. Considering the modifying agents, some polymer blends include the

chitosan and glutaraldehyde treatment to improve hydrolytic degradation [49]. Where the glutaric aldehyde facilitates the structure stabilization with acetal bonds. Another approach of chemical crosslinking demonstrated that, the hydrophilicity of PVA coatings is a solution for the wettability modification of the electrospun PVDF fiber membrane. The obtained material was subjected to acid-catalyzed crosslinking with glutaraldehyde prior to the formation of a polyamide active layer on the PVDF membrane via interfacial polymerization [85]. As the modifying agents the various chemicals could be applied: glutaric dialdehyde solution [86], [87], citric acid [88]. But their inclusion could reduce the biocompatible properties of the composite.

Methanol assisted crosslinking is simple to implement and suitable to the encapsulated fibers compared to the heating physical crosslinking. *Miraftab et al.* assessed the methods of physical crosslinking to improve the structure integrity of PVA-based composite in the study [82]. The experiments included the comparison of the methods of annealing of polymer up to 180 °C and methanol vapor treatment. The high impact on the mechanical properties was concluded for the heat treatment. However, based on the wound healing application the methanol protocol is feasible due to the higher swelling degree and low temperature of processing, that allows to operate with biological agents.

The advantage of physical crosslinking is the process facilitated by the hydrogen bonds within the PVA monomers whereas the chemical crosslinkers are formed by the covalent bonds between the crosslinkers and hydroxyl groups of PVA. Considering the medical applications, the composite should meet the requirements of the accurate dosage of chemicals and inorganic substances to preserve the safety for biology of human

organism. One of the potential solutions is to include the emerging crosslinkers such as a graphene oxide and silica or the biocompatible polymer in the composite. This method of strengthening polymer network is considered in this thesis. After the review of numerous sources there are a lot of solutions that convey the actuality of the polymer fiber composites in scope of the pharmacy and for bioimaging.

#### *Conclusions and Findings of Chapter*

- PVA provides high electrospinning ability and wettability not only for pristine PVA composition, but also for polymer blends.
- Electrospun fiber mats possess applicable characteristics such as simultaneous medicated therapies, and simple and cost-effective encapsulation. The large surface area with the loading of lower concentration of drugs decreases the toxicity and side effects. These features allow to design the fiber biomaterials, particularly drug carrier systems [89].
- The coaxial electrospinning supports the administration of poor soluble and pH sensitive agents [36].
- The diversity of spinning polymers suggests many models of drug release controlled by the drug-in-polymer interactions, polymer-in-polymer interactions.
- The chemically and physically modification of fiber composite could be provided by crosslinking agents and precursors of spinning solutions. The different molecular weight of PVA does not significantly affect the drug release, when the chemical crosslinking of structure by new covalent bonds is a crucial contributing

factor to the release profile. But the addition of chemicals is not favorable due to the biocompatibility requirements.

- One of the feasible approaches is considered with help of the nanosized graphene oxide and silica. Their comprehensive applicability is considered in the Chapter 2.3 – 2.5.

## 2.2 The dissolution and degradation mechanism support drug release

Fiber degradation is a key feature of fiber composite in the biomedical field. After the contact of the composite with the medium, the solution molecules spread around the polymer matrix, causing the mechanisms of degradation of the fiber. Towards the model of drug dissolution, the vision of mechanism is simplified to the constant diffusion with the concentration gradient of drug. The medium of dissolution is assumed as two layers: the stagnant layer that is enclosed to the drug surface; and bulk liquid as the full volume of solvent. In case the drug carrier is no swellable and degradative system, the release is defined by the flux and initial concentration. Where the drug molecules start distribution from high concentration to the less ones ruled by the Fick's law known as the Case I (1), where  $J$  – 'flux' known as an amount of substance passing perpendicularly through a unit surface area per time.  $D_f$  is the diffusion coefficient;  $\frac{dc}{dx}$  is the concentration gradient.

$$J = -D_f \frac{dc}{dx} \quad (1)$$

For the Case I, the diffusion within the non-swellable polymer matrix is regulated by the flux of Fick's law, but another Case II mechanism exists, where the *polymer interactions of matrix* determine the diffusion of drug molecules by the sorption and swelling of mechanisms [90].

Table 1 Drug Release Models

Formula	Name	Description
$\frac{M_t}{M_\infty} = Kt \quad (2)$	Zero-order	$\frac{M_t}{M_\infty}$ – fraction of drug released at time; K – slope of the linear plot of cumulative release versus time

$\ln \frac{M_t}{M_\infty} = -Kt \quad (3)$ $\log M_t = \log M_\infty - \frac{Kt}{2.303} \quad (4)$	First-order	$M_t$ – concentration of drug dissolved in time $t$ ; $M_\infty$ – initial concentration of drug $-\frac{K}{2.303}$ – slope of the linear plot of log cumulative percentage of drug remaining versus time
$\sqrt[3]{\left(1 - \frac{M_t}{M_\infty}\right)} = -Kt \quad (5)$	Hixon – Crowell (1931)	$M_\infty$ – the initial amount of drug; $M_t$ – the remaining amount of drug; the dissolution curve is built as a plot of cube root of drug percentage remaining in matrix versus time
$M_t = M_\infty + K\sqrt{t} \quad (6)$	Higuchi (1963)	$K$ – slope of the curve plotted as cumulative percentage drug release versus square root of time
$\frac{M_t}{M_\infty} = Kt^n \quad (7)$ $\log \frac{M_t}{M_\infty} = \log K + n \log t \quad (8)$	Korsmeyer – Peppas (1983)	$\frac{M_t}{M_\infty}$ – fraction of drug released at time; the dissolution curve is built as a plot of log cumulative percentage drug release versus log time, where $n$ value is a slope of the plot
$M_t = \frac{4KA}{l} t \quad (9)$ $\frac{M_t}{M_\infty} = \frac{2K}{C_0 l} t \quad (10)$	Ritger and Peppas (1987)	$M_t$ – amount of drug release at time from the thin film with: $l$ – thickness; $A$ – surface of film; $C_0$ – drug concentration

Drug release denotes a complex phenomenon merging the drug and polymer solubility in medium and induced drug diffusion. Table 1 represents the conventional mathematical models of drug kinetics, where the main parameters are the cumulative drug release in percentage ( $Q$ ) or in fraction ( $\frac{M_t}{M_\infty}$ ) of released drug in the time ( $t$ ), a release constant ( $K$ ) and a release exponent ( $n$ ).

The dissolution profiles of drug are divided into a burst, long-term, biphasic, ultrasound and light triggered. Prevailing burst or rapid release profile is characterized by the high concentration of immobilized agent and generally interpret the initial stages of release profiles. Due to the high dosage of cumulative release, the burst release is not feasible and safe for administration of high toxic and targeted medicines.

Long-term release with the gradual dosage of agent is mainly one of the most demanded pharmacokinetic models, where the profile is characterized by the slow rate of release with the gradual dosage.

Biphasic drug release embraces the combination of two stages with the differentiated release behavior: burst release and long-term dissolution mechanisms.

Triggered release mechanism is induced by the ultrasound, light and mechanical stress exposure and other impulse of influence for the sample. These methods provide the control of the release processes and maintain the predictable treatment.

The mentioned factors divide the representation of release profiles into the several major types such as Zero-order, First-order and the various mathematical models such as Korsmeyer – Peppas [91], [92], Higuchi model [93], [94]. The abundance of the kinetic models is explained by the numerous parameters in the drug dissolution experiments defined by the cases of administration and dosage forms [95–97].

*Zero-order kinetics* is described when a constant dose of a drug is released per unit of time, but the release rate does not depend on the loaded concentration of the drug. Zero-order release has the potential to overcome the issues of burst and first-order systems by releasing the portion of drug with a constant rate to retard the dissolution process within the period of therapy.

*First-order kinetics* occurs when the drug release rate directly correlates with the drug concentration. The hazard of first-order release is the overdose of drug associated with the cumulative concentration.

*Sustained or long-termed release* meets the requirement of the careful drug administration due to the slow and gradual release of a medicine over an extended period after the initial administration [98]. However, the burst release is on demand for the development of oral and ocular forms for drug administration.

Fitting of the collected data to the mathematical models helps to describe the mechanism of drug dissolution. Mathematical models reflect the structural and geometric characteristics of the carriers, and the diffusional mechanism defined by a release exponent  $n$ . The release exponent  $n$  value is important to characterize different mechanisms given in Table 2 [95]. This indicator defines the dependance of release rate on time, swelling of matrix, diffusion rate. If  $n$  value is equal to 1, that corresponds to the linear representation of the Zero-order release where the time of release is independent from the drug concentration.

Table 2. Release exponent defines the drug release mechanisms

Release exponent (n)	Drug diffusion mechanism	Rate as a function of time	Drug release mechanism
$n < 0.45$	Quasi-Fickian diffusion	$t^n$	Non swellable matrix diffusion
0.45	Fickian diffusion	$t^{-0.45}$	Non swellable matrix diffusion
$0.45 < n < 1$	Non -Fickian diffusion	$t^{n-1}$	Both diffusion and relaxation
1	Case II transport	Time independent	Zero order release
$n > 1$	Super case II transport	$t^{n-1}$	Relaxation/erosion

Hixon – Crowell model has the application for the tableted carrier systems where the dissolution proportionally occurs in planes with the preserving the geometrical form [99]. The surface area to volume ratio of PVA oral dosage form was discovered as the crucial factors for the dissolution profiles.

Peppas models investigate the dependence of release for swellable polymeric films and transfer mechanisms [100,101]. Where the Ritger – Peppas model describes the immobilization of drug from a thin bulk film with thickness  $l$ .

The profiles of fiber materials were best fitted to the Korsmeyer – Peppas model among the different kinetic models. As the crucial factors there are the drug-in-polymer miscibility and interactions within the polymer base. As an example of polymer interactions, the decomposition time of PLGA polymer composite is related to the ratio of the monomer constituents of PLGA as lactic and glycolic acids, which causes a different release time of the encapsulated substance in the referenced study [102]. The measured pharmacokinetics of hydrophobic drug encapsulated in the PLGA (85:15) fiber showed slower degradation rate with prolonged gradual release compared with PLGA (50:50) over 28 days. The release profiles of PLGA and PCL samples were best fitted to the Korsmeyer – Peppas and Higuchi models. The Korsmeyer– Peppas model considers the processes of drug diffusion within the microfiber matrix including the diffusion of medium, polymer swelling and cumulative drug release. In opposite, the dissolution model of the PLLA fiber composite is well correlated with the Higuchi model. Where the drug diffusivity is assumed to be constant; the initial drug concentration is much higher than drug solubility in medium; polymer swelling and dissolution are negligible. Higuchi kinetic model performed better

correlation in the other study with the antibiotic dissolution from PLA-PCL based fiber films [103].

Identifying specific combinations of drug carrier matrix, there were different release profiles observed for the electrospun composites loaded with a hydrophobic drug in the work [102]. The release curves of dexamethasone from the PLGA 50:50, PLGA 85:15, PCL, and PLLA fibers were significantly different over the 28 days of experiment. The PCL fibers exhibited a burst release of 98 % of drug within 24 h, when the cumulative release of drug from the semi-crystalline PLLA was gradual throughout the entire time of study. The release kinetics of PLGA fibers with the different amount of meshes showed the cumulative release of 39 % and 26 % for 50:50 and 85:15, respectively. Comparing the release profiles there was the obvious difference in the release rate between the same polymer but with the different ratio of monomers of PLGA.

Addressed to the reference [102], the release rate directly correlated with the diameter dimension of fibers, where the higher diameter of fibers provided slower cumulative release between 1 and 7 days. The studies of the effect of fiber features accumulate the experience to build a drug carrier system with the expected drug kinetics.

One of the approaches towards the controllable release is to provide the multilayered fiber structure with the protective hydrophobic PHB shell [104]. This strategy allows to control the release rate of proangiogenic agent by the higher thickness of shell. *Wang et al.* noted that the first stage of dissolution profiles was mainly attributed to the burst release for all compound of multilayered fibers. Where the time of release was directly affected by the location of encapsulated drug (core/shell) and type of polymer.

However, the parameters of shell contributed to the second stage of release, whereas the slow rate of release correlated directly with higher thickness of protective shell.

The review of relevant studies conveys the attention to the structure and composition modifications with the formation of intermolecular and intramolecular interactions. Chemical crosslinking and physical crosslinking are designed to improve the features of materials in the co- and postprocessing stage. According to the results of study [77], the effect of physical crosslinking was investigated for PVA/PAA bilayer nanofiber composite with incorporated of doxorubicin (DOX) as a model of drug. After the being annealed in the 100 °C, the electrospun material showed the retarded hydrolytic degradation of composite films.

The goal of this work is to study a drug carrier system made of medicated fibers. Considering this application, the destruction of the polymer matrix is an important feature to reveal the drug dissolution [105]. All mentioned factors make impact on the drug release kinetics throughout the entire release period characterized by the rate of polymer degradation. In conclusion of this section, there are following highlights for the interpretation of release profiles for fiber materials.

- The drug-polymer interactions make the crucial input to the rate of fiber dissolution with the consequent change of dissolution profiles.
- The hydrophobicity, swelling, the monomeric composition, and dimension and morphology of fibers and the place of encapsulation (core/shell) contribute to the release rate of incorporated drug.

- Enormous types of release models could be implemented, where the prolonged and gradual release rate is mostly preferred and called as a sustained model of release.

### **2.3 Modifying agents of fiber mats**

To regulate the fabrication route, there are following parameters of produced materials that are pursued. The composition of spinning solutions should be considered to design the continuous fibers. The inherent factors are given in the list and directly affect the product of electrospinning:

- Composition of fibers (polymer, nanomaterials);
- Molecular weight of polymer base;
- Distribution of nanoparticles;
- Hydrophilic and hydrophobic properties of components;
- Solubility of drug and dispersion of assisted additives;
- Coaxial structure of the fiber;
- Crosslinking with chemical agents and physical crosslinking;

Polymer interactions of spinning solutions define the fiber fabrication including the morphology and defects such as beads and spin-like fibers [106]. Two major factors are polymer-in-polymer molecular bridges such as electrospinning of interacting polymer blends, and polymer-small molecule/nanoparticles interactions including agents or particles in the polymer compound. Towards the elaboration of chemical crosslinking, *Nishiyabu et al.* modified the PVA with including a boronic acid-appended fluoroalkane

[107]. The new compound showed the enhanced water repellency of surface with the contact angle of 85°. The mechanism of this crosslinking procedure is based on the boronate etherification occurred between the boronic acid precursors and the hydroxyl groups of PVA [107], [108]. The nanosized crosslinkers facilitate the stability of polymer chains and viscosity of solutions. Inclusion of nanoparticles and small molecule crosslinkers facilitates the strong intramolecular interactions. This increases the capability of electrospinning for solutions with the low concentration and low molecular weight of pristine polymer. Crosslinking protocol is an important stage of processing to impart mechanical strength and chemical and physical stability to the nonwoven mats. Among the mentioned functions, the nanomaterials such as silica and graphene oxide are considered as the medicine vehicles in the scope of drug delivery.

#### **2.4 Crosslinking with Nanoflakes of GO**

Nanomaterials such as graphene oxide and nano-silica are prospective modifying compounds of the composites. The potential of the composite consisting of the polymer network with embedded nanomaterials is the enhancement of the fiber structure and functionality. Graphene oxide (GO) can be used to improve the mechanical properties and sorption ability of non-woven electrospun fiber mats as membranes for battery and water cleansing fields [109]. The reinforcement of PVA-based composites with graphene oxide has already been proposed in the following biomedical realms [110–112]. The high surface area and structure contribute to a high level of interaction of GO in aqueous solution, miscibility and absorbent functions of GO composites [113]. The hydrophilicity of GO is

suitable for water-soluble polymers such as PVA and PEG to form strong hydrogen bonds within the composite, providing mechanical stability to the core-shell fiber. Chemical structure of GO has the oxygen-containing chemical groups included hydroxyl, epoxide and carboxyl ones. This feature supports the incorporation of hydrophilic as well as hydrophobic agents, revealing the amphiphilic nature of GO. There are studies dedicated the feature of GO oxidized chemical groups to build the attachment of the biological molecules like proteins, DNA, and RNA [114], [115]. In general, high swellable or degradable GO-derived fiber composite could be used to modify the drug release, biosensors and innovative textile solutions [116], [117].

Additionally, the GO and GO-derived nanomaterials have adjustable fluorescence properties that are applicable for bioimaging of tumors and other biomedical therapies with the encapsulation of drug molecules [118], [119].

The large specific surface area of GO is assumed the ability to attach drugs via surface adsorption [120]. Due to the various functional groups, such as phenol, hydroxyl, epoxide and carboxyl groups, the structure of GO provides strong molecular interactions using hydrogen bonds with ketoprofen as a model of drug [121] with polymer mesh composite [122], [123].

The results of GO toxicity remain controversial, and still, the working concentration is under investigation. The feasible wound dressing application is confirmed in the study of GO and PVA derived composite [124]. Where the electrospun fiber composite showed high antibacterial efficiency and good results for 3T3 fibroblast cell proliferation. In some studies, the lowest concentration reaches 1.56  $\mu\text{g/mL}$  for the viable cell response of

epithelial lung cells [125]. According to the study [126], the upper limit of GO concentration, 25  $\mu\text{g/mL}$  in distilled water, caused a 50 % decrease in the cell viability of human skin fibroblasts in the assay after 24 h. Hence, the operational concentration should be carefully considered to create biocompatible core-shell fibers.

The filter application of GO containing membranes is widely considered to purify the waste water from heavy metals and dyes. But the next study [127] suggested the PVC based composition with GO as the membrane to reduce the organic compounds such as Ibuprofen. It is an ongoing task in the pharmaceutical application to control the drug concentration in the aqueous medium minimizing the toxicity.

In conclusion of literature review, graphene oxide is a welcoming agent to the composite studies, due to the listed features and potentials. The effect of this component in the nanofiber composition was studied in this work.

## **2.5 Crosslinking with Nanosized Silica**

Nanoparticles are introduced as an additional crosslinking mechanism to the polymer structure. Multivalent ions can be used to form ionically crosslinked chains as an approach to maintain spinning stability [106]. The crosslinking ability of silica NPs has been used to tailor the viscosity of spinning solutions and polymer concentration [128]. This effect of nano additives results in the morphology of fibers and electrospinning stability that expands the potential polymer compositions.

In regards to the targeted drug delivery, a polymer matrix could serve as a carrier that localized the drug distribution reducing the side effects for the health tissues. This type

of therapy has potentials for malignant tumors, but the drug-in-polymer solubility should be considered carefully. In case the drug dissolves poorly in the polymer, then some auxiliary agent is required. One of the supportive components, the nano silica is considered as a co-delivery container for drug loading due to its high surface area and biocompatibility [129]. There is an opportunity to place the agents selectively, for instance, the water-soluble (Rhodamine B) and hydrophobic dyes (Fluorescein) could be loaded in silica and the polymer matrix separately [130], [35]. Nanomaterials has the broad application in spite of their drawbacks such as a tendency to agglomeration. Thus, the stabilization of nanoparticles is important to provide. The hydrophilic polyethylene glycol (PEG) is suggested as a stabilizing agent that controls the aggregation of nanoparticles from the referenced studies [131]. The study reports that the interaction of silica-PVA leads to the crosslinking mechanism through newly formed chemical bonds Si-O-C [128]. This modification affects the integrity of the composite and expands a variety of nonwoven materials by alternating the rheology of spinning solutions. This effect of including silica should be explored for the case of PVA derived fiber composite.

In this work, the following concept of coaxial electrospinning was used to fabricate the nonwoven fiber mats consisting of core-shell fibers PVA-PEG-SiO<sub>2</sub>@PVA-GO. The dual modification with silica nanoparticles and graphene oxide is expected to provide the crosslinking of the core-shell fiber structure. PVA-GO is a shell of fiber, where graphene oxide improves the mechanical properties and extends the elasticity of composite. PVA-PEG-SiO<sub>2</sub> composite is a core of the fiber, where silica nanoparticles can enhance the structure of the polymer matrix and be involved into the codelivery of drug molecules. The

core-shell fiber mat with the pattern topography is aimed to expand the functional and adhesive properties in the scope of medical applications.

## **Chapter 3. Experimental section**

### **3.1 Materials**

PVA powder with the molecular weight (MW) 72000 g/mol, the degree of hydrolysis 85–89 % and PEG 8000 BioChemica with MW 7000–9000 g/mol were supplied from AppliChem GmbH (Darmstadt, Germany). Polyhydroxybutyrate (PHB) with MW 550000 g/mol, phosphate buffered saline (PBS), doxorubicin (DOX), fluorescent agents: 5(6)-Carboxyfluorescein (FAM), and Rhodamine B (Rh B) were purchased from Sigma-Aldrich (St. Louis, MO, USA). Indocyanine green (ICG) was supplied from MP Biomedicals (USA). Methylene blue (MB) and chlorhexidine gluconate (CHX) were received from Rushim (Russia). Methanol ( $\geq 99.5\%$ ) and dimethylformamide ( $\geq 99.9\%$ ) were supplied from Chimmed, Moscow, Russia. Chloroform ( $\geq 98.5\%$ ) was supplied from Ekos-1 (Moscow, Russia).

The ready-to-use suspensions of silicon oxide nanoparticles (NPs) with a concentration of 0.8 g/L and graphene oxide with a concentration of 30 g/L were courtesy of Dr. S. Evlashin with the fabrication method mentioned in the referenced papers [132,133].

### **3.2 Instruments and Fabrication Techniques of Core-Shell Fibers**

The laboratory setup of electrospinning was constructed by the FabLab and Machine Shop Shared Facility (FabLab) of Skoltech, Moscow, Russia [134].

The laboratory apparatus consists of a syringe pump and a 22 kV high-voltage direct-current power supply with the positive electrode connected to the syringe needle

(Figure 1). The electrospinning setup has two types of fiber collectors: a rotating mandrel and the holder for the flat aluminum target. The rotating mandrel was placed at the tunable distance between the syringe pump. The electric field was applied to the connected electrodes between the syringe needle and mandrel. The polymeric solution was loaded into the syringe and was ejected at the defined flow rate by the syringe pump. The flow rate of the pump was 1 mL/h, and the tip-to-collector distance was varied in a range of 14, 17, 21 cm.

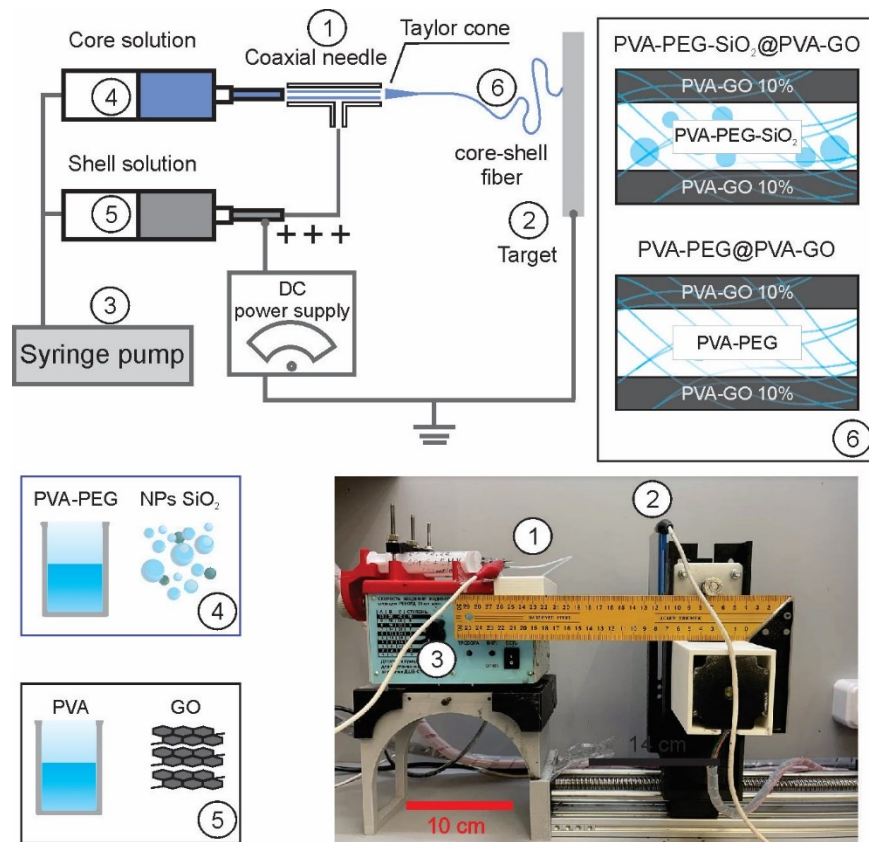


Figure 1. The representation of laboratory setup of electrospinning

### 3.3 Spinning solution preparation loaded with the drug

The following lists of the spinning solutions were prepared (Table 3). The mixture of PVA and PEG powders with the mass ratio 70:30 was dissolved in the MilliQ water, where the polymer part was 12 wt. % of the core spinning solution homogenized at 70 °C, 600 rpm in the magnetic stirrer Hei-Standard (d = 145 mm, Heidolph Instruments GmbH & Co. KG, Schwabach, Germany) for 2 h. The obtained solution was cooled down to room temperature. The silica suspension was sonicated for 5 min and added to the solution where the fraction of silica suspension was 7.5 wt. %. The core solution with the fraction of nanoparticles of silica was 0.005 wt. % was sonicated in the ultrasound bath for 10 min and stirred for 12 h. The solutions were degassed and cooled down to room temperature. The final concentration of NPs of silica was 0.049 mg/mL in the whole PVA-PEG-SiO<sub>2</sub> solution.

For the shell solution, the graphene oxide was mixed with the base polymer solution of the PVA 10 wt. % prepared at 80 °C with a stirring rate of 250 rpm for 2 h. As-received graphene oxide solution was sonicated in the ultrasonic bath Elmasonic S10H (Elma Schmidbauer GmbH, Singen, Germany) for 10 min and added to the PVA solution with the loading of 5 and 10 wt. %. The concentration of GO was 0.5 mg/mL and 1 mg/mL for PVA-GO 5% and PVA-GO 10%, respectively. The final concentration of GO in PVA-GO solutions was calculated from the absorbance spectra in Chapter 4.12.

Table 3 The list of spinning solutions

Name	Mass Ratio			
	Liquid Part, wt. %	PVA, wt. %	PEG, wt. %	SiO <sub>2</sub> , wt. %
PVA 10%	90.0	10.0	-	

	Core composite			
PVA-PEG	88.0	8.4	3.6	
PVA-PEG-SiO <sub>2</sub>	87.995	8.4	3.6	0.005
	Shell composite			
	Water, wt. %	PVA, wt. %	GO, mg/mL	
PVA-GO 10%	90.0	10.0	1.0	
PVA-GO 5%	90.0	10.0	0.5	

### 3.4 Electrospinning of the solutions

The series of fiber composites were prepared from the spinning solutions which properties were studied in the Chapter 4. Chlorhexidine (CHX) as a model of drug was placed in the core solutions PVA-PEG and PVA-PEG-SiO<sub>2</sub> with the concentration 10 mg/mL. The obtained core solutions were used to synthesize the medicated core-shell fiber mats PVA-PEG-SiO<sub>2</sub>@PVA-GO-1x CHX and PVA-PEG@PVA-GO-1x CHX.

- Core solution facilitated the fibers: (PVA-PEG, PVA-PEG-SiO<sub>2</sub>);
- Shell solution originated the fibers: (PVA-GO 5%, PVA-GO 10%);
- Core-shell fibers: (PVA-PEG@PVA-GO, PVA-PEG-SiO<sub>2</sub>@PVA-GO with PVA-GO 10% used);
- Chlorhexidine-encapsulated core-shell fibers: (PVA-PEG@PVA-GO-1x CHX, PVA-PEG-SiO<sub>2</sub>@PVA-GO-1x CHX)

The prepared core and shell solutions were placed in the syringes equipped with a coaxial nozzle. The tip-to-target distance was varied from 14, 17 and 21 cm to assess the effect of tip-to-target distance on the fiber morphology of PVA, PVA-PEG-SiO<sub>2</sub> and PVA-PEG-SiO<sub>2</sub>@PVA-GO fibers. *Section 4.3 Fiber mat characterization* reveals the

dependence of tip-to-target distance versus mean diameter of produced PVA-based fibers. The fiber collector was a flat alumina plate that was placed at a distance of 14 cm from the tip of syringe needle. This distance was set based on the observation of electrospinning performance included in the Section 4.3. and Supplementary Materials (Figure S1-S3).

The core and shell solutions were delivered through the coaxial needle with the flow rate of 1 mL/h. After the synthesis for 3 h, the fiber mats were detached from the target and exposed to the emission of ultraviolet germicidal lamp with the wavelength of 253.7 nm for 1 h.

Electrospinning efficiency was calculated using the formula:

$$\text{Electrospinning Efficiency} = \frac{M_{\text{fiber mat}}}{M_{\text{polymer}}} \times 100 \% \quad (11)$$

where  $M_{\text{fiber mat}}$  is a mass of fiber mat;  $M_{\text{polymer}}$  is a mass of polymer concentration in the core and shell compositions.

### 3.5 Patterning of fiber mat

Two different fiber targets with the applied patterns were used. Lithography etched Si wafer as a pattern mold was generously obtained from Dr. E. A. Gosteva (NUST MISIS, Moscow) [135]. Another target was received from the laboratory of Prof. G. B. Sukhorukov [136,137], where the pits were laser engraved in the aluminum plate with the following parameters: laser wavelength 532 nm and 20 pulses per pit, where each pulse is 50  $\mu\text{J}$ , 1.9 ns. The aluminum plate was polished at the electrolytic polishing machine LectroPol-5 (Struers, Ballerup, Denmark) for 35 s at the applied voltage of 48 V and temperature of 22  $^{\circ}\text{C}$ .

### **3.6 Crosslinking of fiber mats with methanol**

The core-shell fiber mats were collected from the target and crosslinked by soaking in methanol for 12 h. Afterward, the immersed fiber mats were collected in the Petri dish and dried at ambient temperature in the hood for 24 h.

### **3.7 Dip-coating of films**

The PHB granules were dissolved in the mixture of chloroform and dimethylformamide with a mass ratio of 9:1. The concentration of polymer was 4 wt. % of the whole solution. The PHB pellets were rapidly heated to 120°C within 5 min to melt the pellets and homogenized with the organic solvents at  $70 \pm 5$  °C under the stirring of 400 rpm for 5 h.

PVA-PEG-SiO<sub>2</sub>@PVA-GO core-shell fibers were immersed in PHB solution for 1 sec and lifted to exclude the rest of solution. After the immersion the samples were left on the glass slides to dry in the room temperature.

### **3.8 Spinning solution characterization**

Viscosity measurements of spinning solutions were conducted at room temperature using EMS-1000 (Kyoto electronics, Japan). The aluminum sphere ( $d = 2$  mm) was rotated by the induced electromagnetic field with the rate of 1000 rpm during 5 s for the PVA-GO 5 % and with 500 rpm during 5 s for PVA 10 %, 500 rpm during 10 s for PVA-GO 10 %, 500 rpm during 5 s at PVA-PEG, 500 rpm for 30 s at PVA-PEG-SiO<sub>2</sub>. The electrical

conductivity of the spinning solutions was measured with the portable conductometer ST10C-B (Ohaus, Switzerland) for the 10 ml of sample volume.

### 3.9 Wettability and Water Uptake measurements

Pristine PVA, PVA-GO 10% as a shell and PVA-PEG-SiO<sub>2</sub>@PVA-GO core-shell fiber mats were studied to reveal the effect of GO on the fiber composite. Fiber mats collected on a glass slide for 1 h of electrospinning were used for the wettability measurements. Five measurements per sample were conducted to determine the contact angle with the Krüss MBL2000 microscope (KRÜSS Optronic GmbH, Hamburg, Germany) and analyzed with the integrated software.

Effect of water uptake for PVA and PVA-GO 5%, PVA-GO 10% was analyzed with SEM to assess the morphology after the methanol assisted crosslinking and immersion of samples in MilliQ water for 2 h.

Water uptake of PVA-GO 10% as a shell and PVA-PEG-SiO<sub>2</sub>@PVA-GO core-shell fiber was calculated for 3 samples for each sample using formula (12), where  $m_0$  is an initial weight,  $m_n$  is the weight of sample after the water immersion as a function of time  $n$ .

$$\text{Water Uptake} = \frac{(m_n - m_0) \times 100 \%}{m_0} \quad (12)$$

The samples were stored in MilliQ water and weighted daily throughout the 9 days of experiment.

### 3.10 Morphology

The morphology of the obtained fibrous mat was studied with the optical microscope Altami MET 6T (Altami Ltd., St. Petersburg, Russia), scanning electron microscope (SEM) Tescan Vega3 (TESCAN ORSAY HOLDING, Brno, Czech Republic), and FEI Helios G4 Plasma FIB Uxe (Thermo Fisher Scientific, Landsmeer, Netherlands). The samples were preliminary gold-sputtered for 10 s with 25 mA at the Quorum Q150R ES coater (East Sussex, UK) to reduce the charging. At least 100 measurements per sample were collected with ImageJ open-source software (National Institutes of Health, Bethesda, MD, USA) to build the size distribution histograms and calculate the mean diameter.

For transmission electron microscopy (TEM) observations, the PVA-PEG-SiO<sub>2</sub> core fibers were collected for 5 min on top of the 300 Mesh Copper TEM support grid with lacey carbon films Agar Scientific Ltd. (Stansted, UK). Bright-field (BF) TEM and high-angle annular dark-field scanning transmission electron microscopy (HAADF-STEM) images, energy-dispersive X-ray (EDX) spectra, and compositional maps were taken on an aberration-corrected Titan Themis Z transmission electron microscope (Thermo Fisher Scientific, Landsmeer, Netherlands) equipped with a Super-X detection system and operated at 120 kV.

The core-shell structure was monitored with the fluorescence confocal laser scanning microscope LSM 800 with Airyscan (Carl Zeiss Microscopy GmbH, Jena, Germany) to claim the presence of a bilayer structure. The fluorescent dyes 6-FAM and Rhodamine B were added to the core and shell solutions with a 0.01 mg/mL concentration, respectively. The samples of fibers were synthesized on top of the glass slide for 3 min to obtain the discrete fiber network.

### 3.11 Spectroscopic characterization

#### Raman spectroscopy

The samples of the as-received electrospun mats and their components were studied to monitor the peaks attributed to the components and specific ‘fingerprints’ with DXR3xi Raman imaging microscope (Thermo Fisher Scientific, Waltham, MA, USA). Raman spectroscopy was conducted with the laser source 532 nm, where GO and PVA-GO samples were studied at the laser power of 3 mW and 5 mW, respectively. PVA-PEG-SiO<sub>2</sub> and freeze-dried NPs of SiO<sub>2</sub> solution were studied at 6 mW and 4.2 mW of laser power, respectively. Raman spectra of samples were captured in the range of 200–3200 cm<sup>-1</sup>.

#### Fourier-transfered infrared spectroscopy

Fourier-transfered infrared spectra of fiber mats were measured using a Bruker ALPHA II spectrometer (Ettlingen, Germany) with the attenuated total reflectance mode placed inside a nitrogen-filled glovebox.

### 3.12 XRD

X-ray diffraction data of SiO<sub>2</sub>, GO were collected at the Bruker D8 Advance (BRUKER AXS GmbH, Karlsruhe, Germany) by using radiation  $\lambda$  CuK $\alpha_1$ =1.54051 Å at 40 kV, 40 mA.

X-ray diffraction data of fibers mats and polymers were collected at the X-ray Powder Diffractometer Huber G670 (Huber Diffractionstechnik GmbH & Co. KG,

Rimsting, Germany) by using radiation  $\lambda$  CoK $\alpha_1$ =1.78892 Å at 40 kV, 30 mA with a time of scanning 2000 s.

The spectra were collected at a wide range of  $2\theta$  from 4 to 100 °. The background was preliminary subtracted from the data to finalize the peak fitting.

### **3.13 ToF-SIMS**

ToF-SIMS of fiber mats was performed using the instruments: FIB-SEM Tescan S9000: Solaris Ga-FIB (Tescan Orsay Holding, Czech Republic) adopted with ToF-SIMS detector (TOFWERK AG, Switzerland). The following parameters of regime were used for FIB: high voltage of 20 kV, current of 4 nA, 50  $\mu$ m field of view, ToF-SIMS: 512 x 512 pixels resolution, negative and positive modes, binning 4x4, dwell time 20  $\mu$ s. ToF-SIMS data was analyzed using the software TOFWERK Explorer, Switzerland.

### **3.14 Differential Scanning Calorimetry (DSC)**

Thermal behavior of core-shell, shell and core nanofiber mats was studied by a differential scanning calorimeter NETZSCH DSC 204F1 Phoenix (NETZSCH-Gerätebau GmbH, Selb, Germany). DSC thermograms of samples were received from 26°C to 240°C at a heating rate of 10°C/min.

DSC thermograms provide information about the melting temperature, the heat of melting ( $\Delta H_m$ ), and the degree of crystallinity. Melting ( $T_m$ ) temperature was calculated from the DSC curves. The degree of crystallinity ( $\chi_c$ ) was calculated by the formula

$$\chi_c = \frac{\Delta H_m \times 100\%}{\Delta H_c} \quad (13)$$

where  $\Delta H_m$  is the heat of melting calculated from the area under the melting peak;  $\Delta H_c$  is the heat required for melting 100 % crystalline PVA (138.6 J/g) used from the reference [82], [138].

### 3.15 Micromechanical test

The prepared specimens were tested by Deben Microtest 200 N Tensile Stage (Deben UK Ltd., Woolpit, UK) in tension mode with a permanent speed of 1.0 mm/min inside the chamber of Tescan Vega3 SEM (TESCAN ORSAY HOLDING, Brno, Czech Republic). In the experiment, a test sample with a double edge notch geometry was used, where the perimeter of the sample was 25 mm × 14 mm with 2 mm per incision. The thickness of fiber mats was measured with micrometer. The tension was parallelly synchronized with SEM images acquisition with the following settings: Back-scattered Electron (BSE) detector, resolution 1024 × 1024 pixels, 8-bit, scan speed 3.2 μm per pixel, and field of view 1 mm x 1 mm. Then, images were processed by the robust Digital Image Correlation (DIC) method to obtain true material deformations. The DIC technique was realized by open-source Matlab-based software Ncorr v.1.2 (GitHub, Inc., San Francisco, CA, USA) [139]. Two characteristics were determined, namely, elastic modulus and ultimate strength. The tested samples were weighed using the Ohaus analytical balances (Parsippany, USA), and the density of the samples was calculated based on the received mass and area.

### 3.16 UV-Vis Spectral Analysis of Fiber Mats

Fluorescence of GO-based fibers

PVA-GO 5 %, PVA-GO 10 %, core-shell PVA-PEG-SiO<sub>2</sub>@PVA-GO, methanol crosslinked core-shell PVA-PEG-SiO<sub>2</sub>@PVA-GO were incubated in 0.01 M of PBS with pH 7.4, at 37 °C for 24 h in the orbital mixer. After 24 h, the supernatants of solutions were placed in a 96-well plate (Corning 96-well Clear Flat Bottom UV-Transparent Microplate), and fluorescence spectra were recorded with an Infinite M Nano+ (Tecan Trading AG, Männedorf, Switzerland) dual-mode microplate reader. The fluorescent spectra were collected to study the effect of excitation wavelength on the fluorescent properties of GO-based fiber mats. The fluorescence from the samples was excited at 295 nm and 330 nm, 415 nm, and their emission was observed in the ranges 330 – 550 nm and 350 – 650 nm, 440 – 650 nm, respectively.

Loading and Encapsulation Efficiency

The loading and encapsulation efficiency of CHX was assessed for PVA-PEG@PVA-GO-CHX and PVA-PEG-SiO<sub>2</sub>@PVA-GO-CHX fibers with ten samples for each type. Loading efficiency was calculated by the formula (14), where  $m_d$  – total mass of released drug divided by the total weight of fiber mat  $m_f$ .

$$\text{Loading efficiency} = \frac{m_d \times 100\%}{m_f} \quad (14)$$

Encapsulation efficiency was calculated by the formula (15), where  $m_d$  – total mass of released drug divided by  $m_{d0}$  – total mass of drug added in the spinning solution.

$$\text{Encapsulation efficiency} = \frac{m_d \times 100\%}{m_{d0}} \quad (15)$$

The medicated core-shell fiber mats PVA-PEG-SiO<sub>2</sub>@PVA-GO-1x CHX and PVA-PEG@PVA-GO-1x CHX were cut in the sections 10 × 20 mm<sup>2</sup>. Specimens were incubated in 1 ml of PBS medium (pH 7.4, 37 °C) in the thermo-shaker TS-100 (BioSan, Riga, Latvia) at 350 rpm for 24 h. After the incubation, the supernatant was centrifugated to remove GO flakes in MiniSpin® (Eppendorf AG, Hamburg, Germany) at 10 rpm for 4 min. 200 µL of supernatants were placed in the UV-transparent microplate; the optic density of samples was collected at 230 – 400 nm intervals with the step of scan 2 nm and a number of flashes 5 in Infinite M Nano+ microplate reader (Tecan Trading AG, Männedorf, Switzerland). To calculate the concentration, the calibration curves were built from the series of UV absorbance spectra for CHX dissolved in PBS with the concentrations (0.004 – 0.063 mg/mL).

#### Kinetic Drug release

The release of CHX) was monitored for ten samples of each core-shell fiber composite PVA-PEG@PVA-GO-1x CHX and PVA-PEG-SiO<sub>2</sub>@PVA-GO-1x CHX (total 20 samples). Each sample corresponding to ~ 3 mg with 10 × 20 mm<sup>2</sup> was attached to the adhesive tape of Kapton, fitted into a test tube with 1 mL of 0.01 M PBS and stored in an incubation shaker TS-100 (BioSan, Riga, Latvia) at 37 °C and 100 rpm. These conditions were aimed to mimic the wound dressing in the skin conditions. Aliquot parts of 200 µL were withdrawn from the test tubes and measured in the UV-transparent microplate at 230 – 1000 nm intervals for the absorbance spectra with the step of scan 2 nm and a number of flashes 15 in Infinite M Nano+ (Tecan Trading AG, Männedorf, Switzerland). Then, the

supernatant was returned to the dissolution medium in a tube for each release measurement for at least 24 h of experiment.

### **3.17 Antibacterial test**

The antibacterial activity of the CHX-loaded core-shell fiber mats was assessed with *Staphylococcus Aureus* cultivated on a solid medium agar plate. CHX loaded core-shell fiber mats (PVA-PEG@PVA-GO-CHX and PVA-PEG-SiO<sub>2</sub>@PVA-GO-CHX) and as-prepared PVA-PEG-SiO<sub>2</sub>@PVA-GO fibers were formed at the disks with diameter of 6 mm. The fiber samples and a cellulose control with the Doxycycline were placed in the agar medium with the seeded colony of *Staphylococcus Aureus*. After static incubation at 37 °C for 1 day, the inhibition zones around the sample were photographed and measured to assess the bacterial sensitivity/resistivity parameter.

### **3.18 Cell Viability Assay**

Dulbecco's Modified Eagle Medium (DMEM; catalog no. 12491-015), fetal bovine serum (FBS; catalog no. 16000-044), antibiotic-antimycotic (catalog no. 15240-062), and 0.25 % trypsin/EDTA (catalog no. 25200-114) were obtained from Gibco, Thermo Fisher Scientific, USA. L-glutamine (catalog no. F032) and Versen (catalog no. F080) were received from Paneco, Russia. CellTiter-Glo 2.0 (catalog no. G7572) was supplied from Promega, USA.

Primary human fibroblasts passaged 3 times, were cultured in DMEM containing 2 mM L-glutamine and an antimycotic antibiotic solution (1x), with the addition of 10% (v/v) fetal bovine serum (Gibco, Thermo Fisher Scientific, USA) at 37 °C and 5% CO<sub>2</sub>. To transfer cells from the substrate, a Versen solution and a 0.25% trypsin/EDTA solution were used.

The cells were incubated at 37°C for 24 h using the extracts of dissolved core-shell fiber composites (PVA-PEG-SiO<sub>2</sub>@PVA-GO, methanol crosslinked PVA-PEG-SiO<sub>2</sub>@PVA-GO) in MilliQ water to prepare the culture medium. Cytotoxicity of core-shell fibers was assessed with CellTiter-Glo 2.0 system according to the protocol of biological evaluation of medical devices (GOST ISO-10993). Cells were seeded in 96-well culture plate at a concentration of  $1 \times 10^4$  cells per well. Each well contained 100 µl of cell suspension. The plate was incubated for 24 hours at 37°C in a humidified atmosphere with 5% CO<sub>2</sub> to obtain a monolayer cell culture. After 24 h, 200 µl of extracts was added to each experimental well and 200 µl of fresh culture medium was added to the control wells. Plates were incubated for 24 h and 72 h at 37°C in a humidified atmosphere with 5% CO<sub>2</sub>. After 24 h and 72 h, 250 µl of supernatant was withdrawn from each well with adding of 50 µl of CellTiter 2.0 and incubated for 15 min. Obtained solutions were placed in 96-well white opaque culture plate and luminescence was recorded with the Varioskan LUX Plate Reader (Thermo Fisher Scientific, USA). Wells containing a pure culture medium without cells were used to evaluate the background signal. Absolute luminescence values were normalized as follows: the luminescence signal of cells in control wells (in culture medium) was taken as 100% viability. Cell viability in the presence of extracts from PVA-PEG-

SiO<sub>2</sub>@PVA-GO as-received and methanol treated fibers was calculated as a percentage of their luminescence signals received from the experimental and control wells.

### **3.19 Statistics**

CHX release was measured from at least 10 samples separately for each core-shell composite. Antibacterial activity was carried out independently three times using two parallel groups of PVA-PEG-SiO<sub>2</sub>@PVA-GO and PVA-PEG@PVA-GO group. The data are presented as the mean  $\pm$  standard deviation.

## Chapter 4. Results

### 4.1 Viscosity and conductivity

The measurements were carried out at the room temperature as the electrospinning (Table 4). The impact of the dual polymer mixture was considered. The viscosity of PVA 10 wt. % base solution shows 1058.9 mPa·s at a shear rate of 3.1224 s<sup>-1</sup>. The smaller contribution of PVA (8.4 wt. %) for PVA-PEG against the 10 wt. % of the base shows the diminishing viscosity for PVA-PEG solution to 339.8 mPa·s. Notably, PEG with the ratio of 3.6 wt. % did not dramatically change the viscosity behavior of the compositions. Possibly, the increase of addition of silica suspension and PEG will affect dramatically on the viscosity, however even this negligible addition of silica (0.005 wt. %) were correlated with different morphology of produced fibers and drug release behavior discussed in Chapter 4.3 and 4.12, respectfully.

Table 4 The characterization of solutions

Name	Mass Ratio of PVA, wt. %	Viscosity, mPa·s	Shear Rate, s <sup>-1</sup>	Electrical Conductivity, μS·cm <sup>-1</sup>
PVA 10%	10	1058.9	3.1224	672
PVA-PEG	8.4	339.8	2.9594	538
PVA-PEG-SiO <sub>2</sub>	8.4	239.3	4.1350	1332
PVA-GO 10%	9	452.2	2.2462	653

### 4.2 Confocal Laser Fluorescence Microscopy

The core-shell structures were labeled with FAM for the core and Rh B for the shell, respectively. Figure 2 shows the bilayer structure including the core and shell colored green and red, respectively. The mean values for shell wall thickness and core were calculated 66 ± 18 nm and 173 ± 25 nm, respectively.

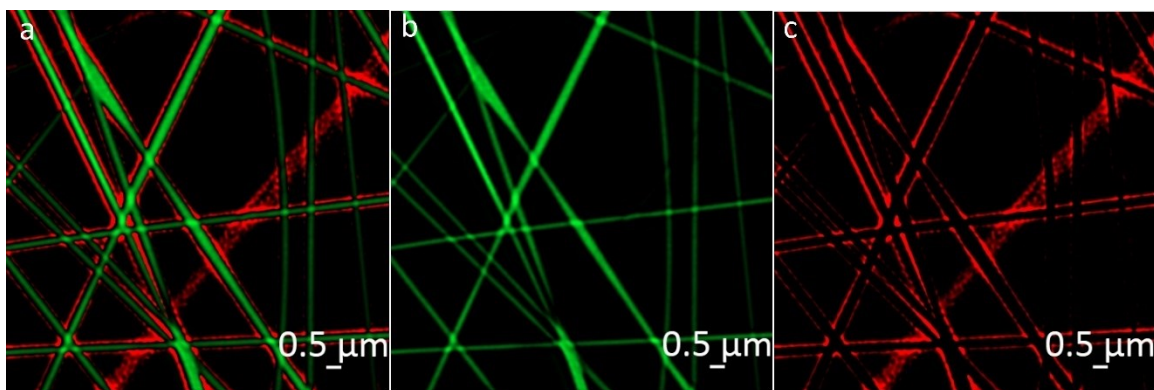


Figure 2. Representative fluorescence microscopy images collected from (a) core-shell PVA-PEG-SiO<sub>2</sub>@PVA-GO fibers with the labeled core-shell structure; (b) green core labeled with FAM; (c) red shell labeled with Rh B

### 4.3 SEM

#### *SEM Study of the As-Received Fibers*

##### *Pristine PVA Fibers*

As the preliminary parameter, the distance was varied from 14, 17, 21 cm, that produced the nanofibers with mean diameters  $386 \pm 81$ ,  $284 \pm 44$  nm,  $268 \pm 63$  nm (Supplementary Materials, Figure S1). It should be noted that all results were collected with fixed tip-to-target distance. Based on our observations of experimental data and referenced studies the tip-to-target distance was set 14 cm in this study as the optimal to build bead-free and homogeneous fiber coating.

The morphology of synthesized fiber mats was observed by SEM. The diameter of fibers from each fiber mat was calculated to monitor the effect of additives and methanol crosslinking. The as-received PVA fiber mat has a mean fiber diameter of  $386 \pm 81$  nm in Figure 3a.

#### *Core composition PVA-PEG-SiO<sub>2</sub>*

The design of core composition was based on the observations of the effect of PVA:PEG ratios on the size of fibers (Supplementary materials, Figure S2). The composition of PVA: PEG mesh (70:30) produces the fibers with mean diameter of  $417 \pm 76$  nm, where the concentration of PVA was 8.4 wt.% of whole solution. In opposite, the composition with the highest fraction of PVA has the mean fiber diameter of  $971 \pm 164$  nm, where the concentration of PVA reaches 10.8 wt.% in the solution. The higher concentration of PVA led to the increased dimension of core fibers in the same presence of silica and PEG. The fibers were collected from the same operational parameters such as voltage, distance, time of collection.

TEM claimed the polymer composition of core (70:30) supports the reduced agglomeration of nano silica. The results are provided and discussed in the Supplementary Materials, Figure S5 and in Figure 8, Section 4.4. The established composition with ratios of PVA to PEG (70:30) was used in the further studies as the rational core solution for coaxial spinning.

#### *Core-shell composition PVA-PEG-SiO<sub>2</sub>@PVA-GO*

The dependance of tip-to-target versus fiber morphology was preliminarily screened to produce continuous fibers with nanoscale dimensions without bead and spin defects. The results showed the optimal distance of 14 cm to produce the robust coating with fiber size of  $329 \pm 71$  nm (Supplementary material, Figure S3). That operational parameter was used to build the electrospun core-shell fibers for the following studies. Despite the distance of 17 cm showed rather uniform distribution, it was difficult to collect

the fiber mats due to the drops of non electrospun solutions after the 1 h of synthesis, in case of tip-to-target distance at 14 cm. Hence, we observed the ability to collect the synthesized fibers from target and to operate easily with them for further applications. Tip-to-target distance at 14 cm seems the golden mean in this regard.

### *Core Fibers*

In Figure 3b, PVA-PEG presents the bigger fiber size distribution with a mean fiber size of  $685 \pm 145$  nm. With the addition of SiO<sub>2</sub>, the mean size of core fiber was slightly decreased to  $381 \pm 131$  nm (Figure 3c). The presence of nanoparticles could reduce the movement of polymer chains by the emerging covalent bonds between silica and the polymer matrix that results in the formation of the diminished fiber size under the electric field. In Section 4.6-4.7 the effect of the silica nanoparticles was traced in the core PVA-PEG-SiO<sub>2</sub> fiber with help of Raman and FTIR spectroscopy.

Figure 3d illustrates the effect of GO content on the PVA-based fiber. PVA-GO demonstrates a decreased fiber diameter to  $174 \pm 31$  nm compared to the pristine PVA 10% fibers. The loading of GO results in the narrowing of fiber diameters for stable electrospinning of mats with the same operational parameters.

There is a tendency of fiber decreasing observed for the core-shell fibers PVA-PEG@PVA-GO and PVA-PEG-SiO<sub>2</sub>@PVA-GO given in Figure 3e and Figure 3f, respectively. At the same time, the mean diameters of the core-shell fibers of PVA-PEG@PVA-GO and PVA-PEG-SiO<sub>2</sub>@PVA-GO are  $535 \pm 112$  nm and  $261 \pm 51$  nm, respectively. The decreased fiber diameter could relate to the physical properties of

spinning solutions, such as viscosity and conductivity, mentioned in Table 4 The measurements of solutions.

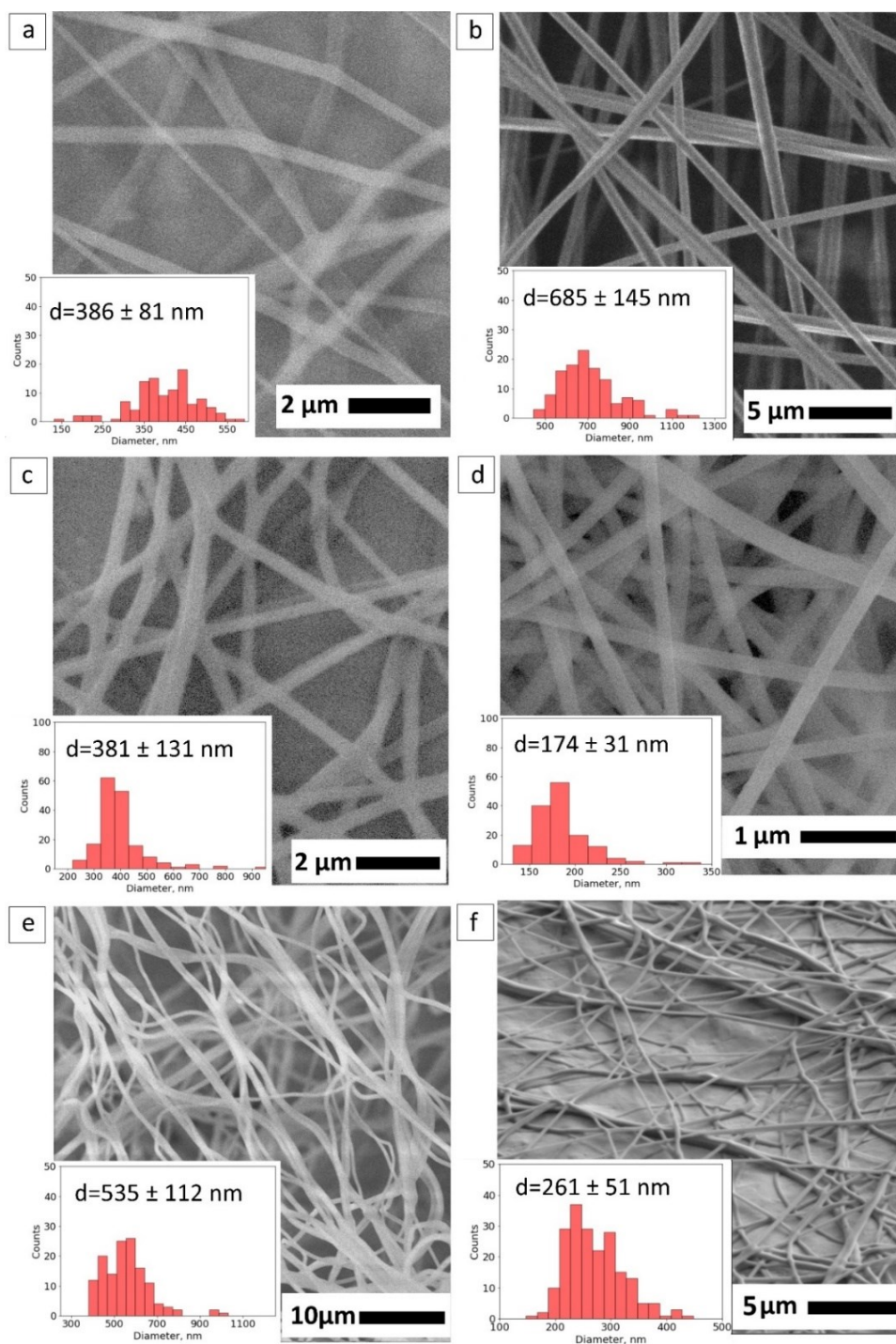


Figure 3. SEM imaging of fibers: (a) pristine PVA; (b) PVA-PEG core; (c) PVA-PEG-SiO<sub>2</sub> core; (d) shell PVA-GO 10%; (e) core-shell PVA-PEG@PVA-GO; and (f) core-shell PVA-PEG-SiO<sub>2</sub>@PVA-GO

### *SEM Study of the Crosslinked Fibers*

To increase the structural integrity of the PVA-based composite, the procedure of crosslinking with methanol was suggested. Considering the simplicity of the method mentioned in the study [82], crosslinking with methanol was chosen. Methanol evaporates in room conditions and is suitable for the robust fabrication of fiber mats. A crosslinked PVA fiber mat performs a mean diameter of  $415 \pm 88$  nm in Figure 4a.

Figures 5b–c demonstrates the morphology of crosslinked samples starting from the core compositions: PVA-PEG, PVA-PEG-SiO<sub>2</sub>. The crosslinked fibers of PVA-PEG retain the fibrous structure with a wide range of sizes starting from 400 nm to 1200 nm, shown in Figure 4b. The mean diameter of crosslinked PVA-PEG fibers is  $927 \pm 188$  nm. Figure 4c demonstrates the effect of silica added in core composition. The core solution PVA-PEG-SiO<sub>2</sub> provides the smaller size distribution of fibers with diameter  $711 \pm 132$  nm.

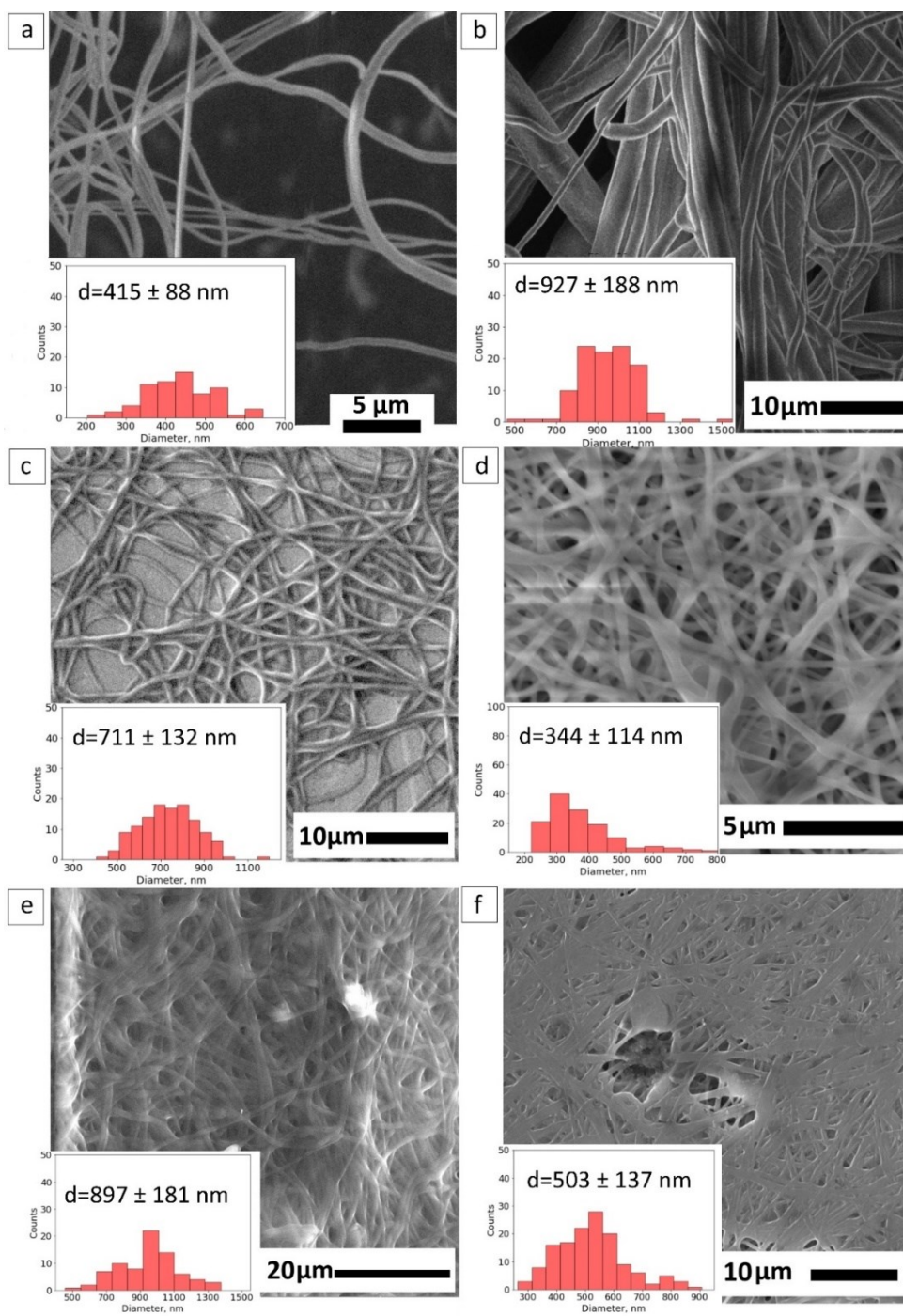


Figure 4. SEM imaging of crosslinked fibers with methanol: (a) pristine PVA; (b) PVA-PEG core; (c) PVA-PEG-SiO<sub>2</sub> core; (d) shell PVA-GO; (e) core-shell PVA-PEG@PVA-GO; and (f) core-shell PVA-PEG-SiO<sub>2</sub>@PVA-GO

The PVA-GO-based composite as the shell is presented in Figure 4d. The mean size of fibers changes to  $344 \pm 114$  nm after crosslinking treatment. Despite the GO's solubility in methanol, the presence of GO was claimed in the polymer matrix with the Raman spectroscopy in Section 4.6.

Figure 4e and Figure 4f demonstrate the same trend of the diameter diminishing for the crosslinked core-shell PVA-PEG@PVA-GO against PVA-PEG-SiO<sub>2</sub>@PVA-GO, with the mean diameter  $897 \pm 181$  nm and  $503 \pm 137$  nm, respectively. The methanol vapor treatment facilitates the crosslinking of polymer chains to maintain fiber morphology. Methanol plays the main role in stabilizing the polymer network due to the hydrogen bonds formed between pendant hydroxyl (-OH) groups in PVA chains.

The following SEM images were collected from the samples of fibers loaded with the CHX. Figure 5a demonstrates the produced core fibers with a mean diameter of  $666 \pm 256$  nm. Figure 6b shows that the core-shell fibers with CHX present the same trend as noticed for the core-shell fibers without any drug loading. The mean diameter of core-shell fibers  $283 \pm 51$  nm was close to the  $261 \pm 51$  nm of the pristine core-shell fibers. The effect of coaxial spinning was noticed to decrease the mean diameter of the core-shell fiber, indicating the same trend for PVA-PEG-SiO<sub>2</sub>@PVA-GO and PVA-PEG-SiO<sub>2</sub>@PVA-GO loaded with CHX.

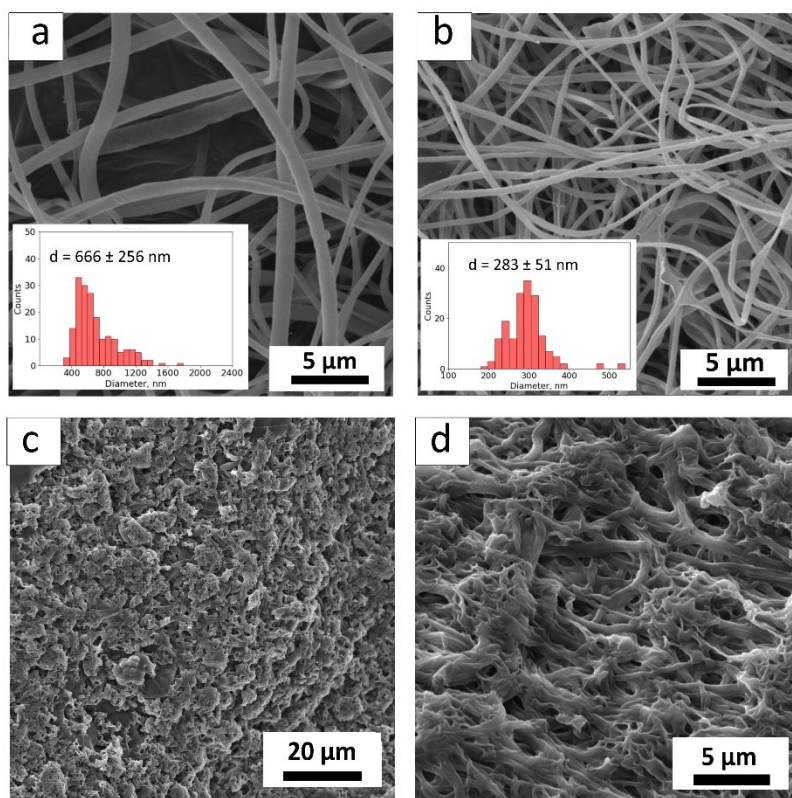


Figure 5. SEM images of **(a)** core fiber PVA-PEG-SiO<sub>2</sub>-CHX; **(b)** core-shell PVA-PEG-SiO<sub>2</sub>@PVA-GO-CHX fibers; and after dip-coating with PHB: **(c),(d)** methanol crosslinked core-shell CHX fibers

The morphology of crosslinked core-shell fibers was studied with SEM after the dip-coating protocol. In Figure 5c and Figure 5d the dip-coated fibers were presented. The morphology of fiber mats was altered by the thin coating of PHB polymer, this strategy was aimed to retain the fiber mat in the aqueous medium.

The topography of fiber mats is a crucial factor in case of the cell adhesion. The patterned targets produced with the lithography and laser ablation convey the different geometry to the nonwoven mats. SEM images of the targets and the processed fiber mats were included in this work to illuminate the potentials of fibers as coatings. Supplementary

Materials, Figure S4 shows that the patterned fiber coatings replicate the produced topography preserving the separate fibers.

#### *The Effect of Water Uptake on Fiber Diameter*

To analyze the impact of GO on the water uptake, the following experiment was carried out for PVA, PVA-GO 5%, PVA-GO 10 % with the use of SEM analysis of the fiber diameter. The samples were stored in distilled water for 2 h during the experiment to watch the fiber nearest degradation stage via SEM imaging. The short period of incubation relates with the light weight of sample to exclude the early disruption of thin films. PVA fiber mat was used as a control sample. Some samples of PVA fibers suffered depletion and full dissolution after 240 min because of the prolonged contact with the deionized water. The assessment of fiber size was difficult to handle for the experiments. Hence, to achieve the same evaluation time for all the films, the fibers were incubated for 240 min.

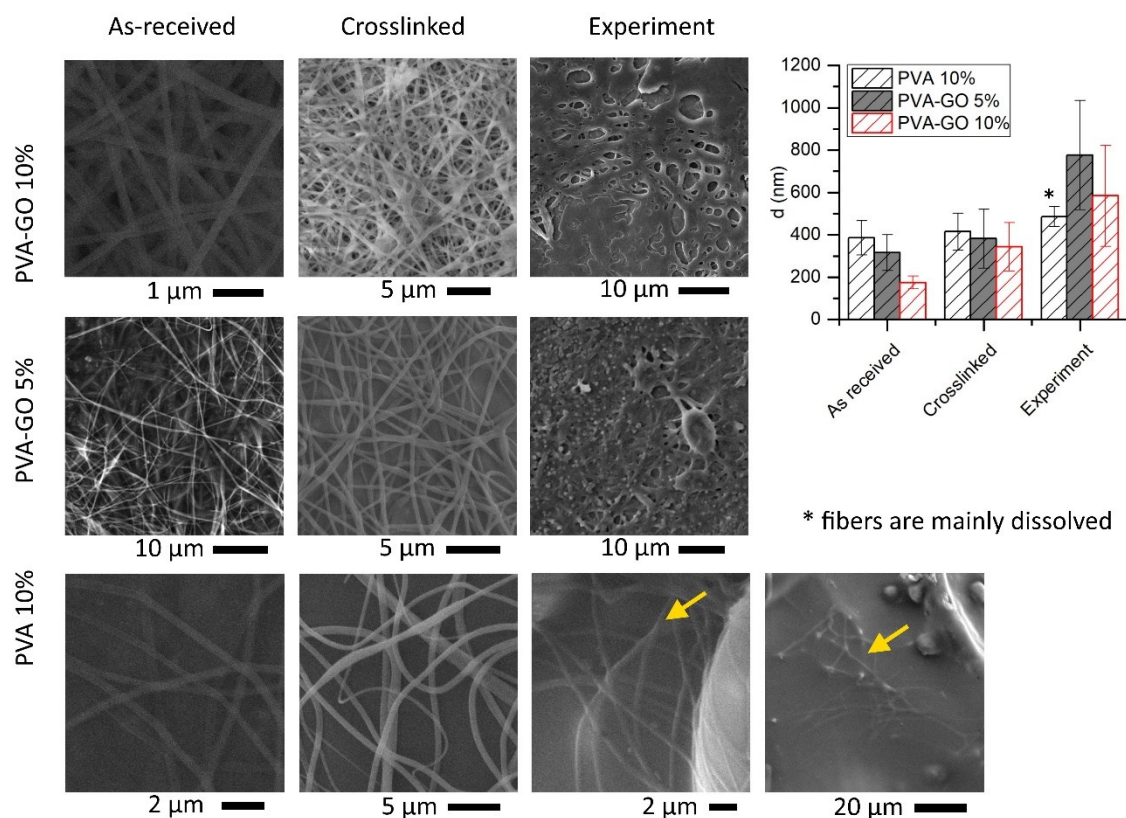


Figure 6. SEM imaging of as-received, crosslinked and soaked fiber mats after the incubated in water medium for 2 h

Figure 6 demonstrates that GO loading of 5 wt.% slightly increases the average fiber diameter after crosslinking. The bigger loading of GO 10 wt.% fabricated the decreased diameter of as-received fibers, but after crosslinking the fibers increased at two times. However, the addition of graphene oxide changed the fiber morphology at least two times after being kept in water for each PVA-GO composite. The results show that the addition of GO causes the bigger swelling of the PVA-GO fibers after the water immersion. The fiber mats were transformed into the hydrogel, when pure PVA film was completely dissolved after 2 h.

#### 4.4 STEM and EDX

Bright-field (BF) TEM and high-angle annular dark-field scanning transmission electron microscopy (HAADF-STEM) imaging were performed to monitor the distribution of silica nanoparticles in the fiber core. The histogram of silica nanoparticle size distribution is shown as an inset of Figure 7a. The average particle size distribution of silica was calculated from STEM images, where the size distribution ranges from 20 to 120 nm, and the mean diameter of silica  $d$  equals  $54 \pm 17$  nm. Blue arrowheads indicate the location of individual silica particles on the fiber. The individually separated nanoparticles within the fiber are observed in the PVA-PEG-SiO<sub>2</sub> (70:30) in Figure 7b, c, while they are mostly segregated in the sample with PVA-PEG mixed in a ratio of 90:10 in Figure 7a. EDX compositional maps were registered for O, Si, and C elements to detect the distribution of silica spheres in the core fiber PVA-PEG-SiO<sub>2</sub> (90:10) in Figure 7d.

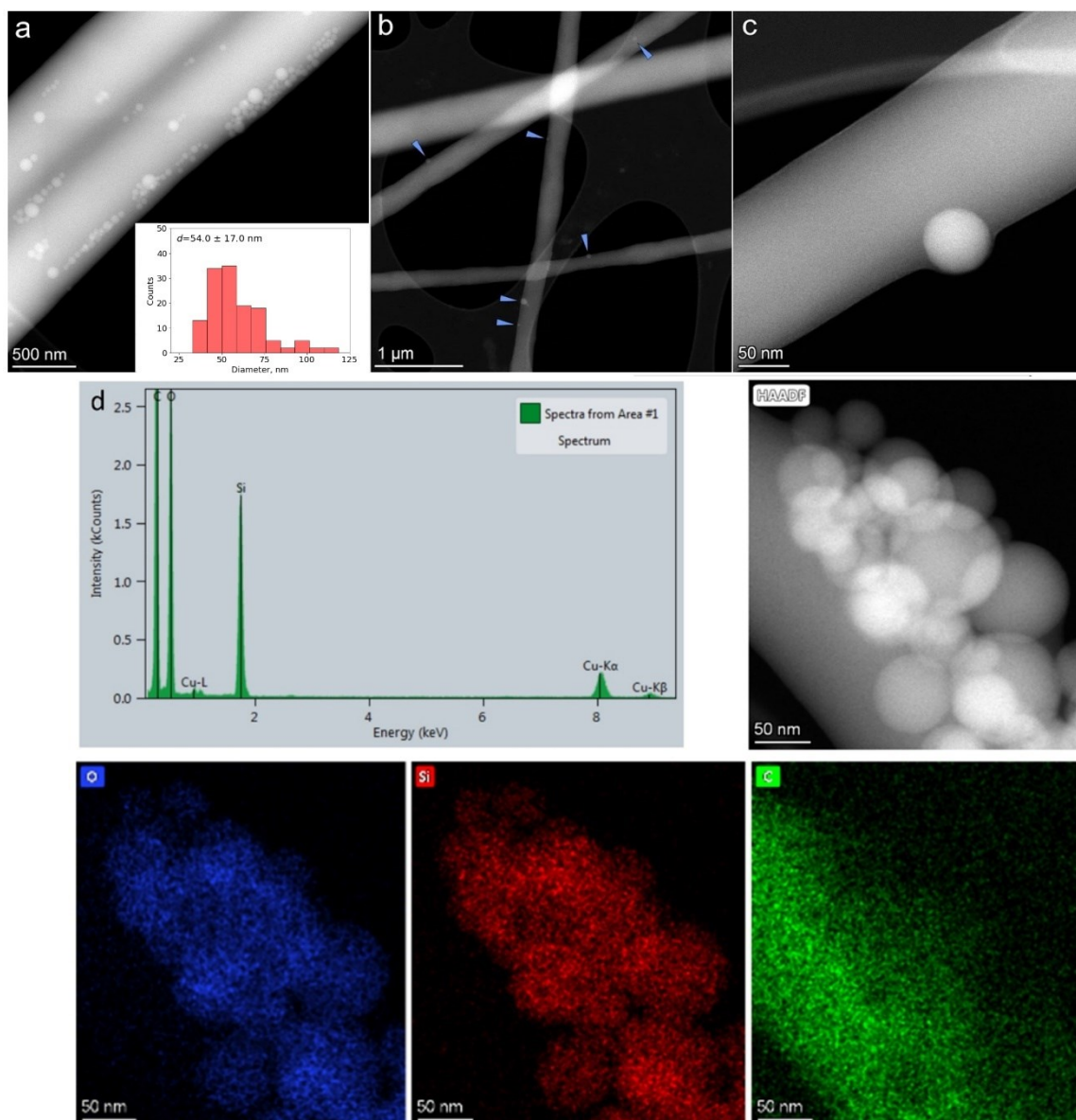


Figure 7. HAADF-STEM images of **(a)** PVA-PEG-SiO<sub>2</sub> with PVA:PEG (90:10); **(b,c)** PVA-PEG-SiO<sub>2</sub> with PVA:PEG (70:30); **(d)** EDX analysis of PVA-PEG-SiO<sub>2</sub> with PVA:PEG (90:10) with compositional mapping of O, Si, and C elements

During this study three different compositions were studied with TEM to find the optimal ratio of PVA and PEG for building of core fiber. The studied core fibers contain the different polymer graft of PVA and PEG in the 90:10 and 70:30 that were investigated with TEM (Supplementary Materials, Figure S5). The mixture of PVA and PEG with the

ratio of 70:30 was selected as a working composition of core for PVA-PEG-SiO<sub>2</sub>@PVA-GO core-shell fiber. The composite with ratios of polymers PVA: PEG (90:10) demonstrates agglomerates of silica that claim the feasibility of graft PVA:PEG (70:30), where PEG functions as a good dispersant. The increased PEG content prevents the greater distribution of silica nanoparticles in the core fiber.

#### **4.5 Contact angle and Fiber Diameter after Methanol Treatment**

The wettability of shell fiber and core-shell samples were assessed to trace the impact of GO and NPs of silica on the fiber composites (Table 5). The mean contact angle was calculated after the drop stabilized for 10 s before the drop was fully absorbed by the thin sample. The mean contact angle for PVA-GO 5% and PVA-GO 10% changes from  $48 \pm 7^\circ$  to  $39 \pm 5^\circ$  with the higher loading of GO fraction. The high hydrophilicity of graphene oxide results in the rapid absorption of fibers during the contact angle measurements. Being rearranged inside the fibers, GO nanoflakes form a high hydrophilic structured surface of PVA-GO composite due to their high hydrophilicity related to oxygen-containing functional groups of GO. The incorporation of GO showed the increased contact angle for PVA-GO 10% in comparison with the pure PVA fiber. The contact angle for PVA-GO fiber mats with the GO loading of 10 wt. % is reduced due to the higher surface area characterized by the diminished diameter of fibers  $174 \pm 31$  nm (Table 5).

Figure 8a and Figure 8b demonstrate the slightly increased contact angle for the PVA 10% and core-shell PVA-PEG-SiO<sub>2</sub>@PVA-GO, where the shell made of PVA-GO. The

negligible increase of the contact angle is noticed for pure PVA 10 wt.% and PVA-PEG-SiO<sub>2</sub>@PVA-GO core-shell fibers with the shell made of PVA-GO.

Table 5. The contact angle of PVA-GO 5%, PVA-GO 10%, and PVA-PEG-SiO<sub>2</sub>@PVA-GO before and after crosslinking

Name of Sample	Average Diameter, nm	Contact Angle, °
As-received		
PVA 10%	386 ± 81	28 ± 3
PVA-GO 10%	174 ± 31	40 ± 3
PVA-PEG-SiO <sub>2</sub> @PVA-GO	261 ± 51	26 ± 3
Crosslinked		
PVA 10%	415 ± 88	37 ± 4
PVA-GO 10%	344 ± 114	39 ± 2
PVA-PEG-SiO <sub>2</sub> @PVA-GO	503 ± 137	34 ± 1

Water uptake of PVA-GO 10% was assessed after incubation of samples in the distilled water for 9 days. In Figure 8c the results show the massively increased mass of samples due to the high absorption of GO. The value of water uptake is near 288 % after 1 day of incubation. Notably, the PVA-GO composite was stable in water after the swelling and preserved the integrity after 9 days.

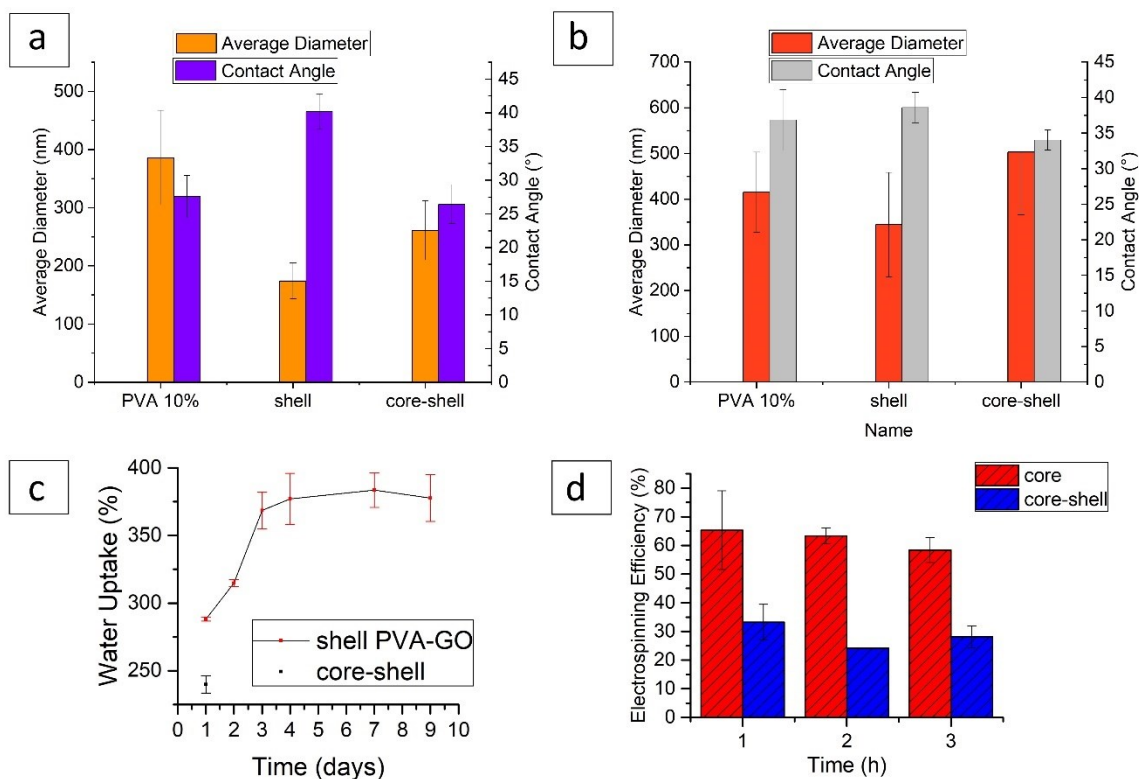


Figure 8. The contact angle of **(a)** as-received fibers and **(b)** methanol crosslinked fiber mats; **(c)** water uptake of shell PVA-GO 10% and core-shell fibers; **(d)** electrospinning efficiency

The methanol crosslinking alters the morphology of fibers containing GO. The morphology of as-received and crosslinked fibers was compared. The diameter growth by over 90% demonstrates the swelling behavior of the GO-based shell and core-shell fibers. The referenced work supposed the dependence of fiber diameter and wettability in case of thermally crosslinked PVA based composite [77]. Despite the increased diameter of fiber, the crosslinked fibers show the same contact angle relatively to as-received ones, that is expected to prolong the fiber degradation time. The control of the fiber diameter and wettability is aimed to alter the time of fiber mat dissolution that is important in terms of the drug release.

The electrospinning efficiency of core and core-shell fiber mats reveals the difference in performance with uniaxial and coaxial spinning. The productive efficiency of core composition is about 65.3 % that is much higher in comparison with the 32.7 % for core-shell fibers synthesized for 1 h (Figure 8d).

#### 4.6 Raman Spectroscopy

The sample of as-received graphene oxide was monitored with Raman spectroscopy. The spectra of PVA-GO composites and GO were observed to find out the characteristic D and G bands of graphene oxide, where the D band is in charge of the defects and vacancies of  $sp^2$  carbon hybridization, and the G band indicates the stretching C–C bonds. D (ca.  $1346\text{ cm}^{-1}$ ) and G (ca.  $1588\text{ cm}^{-1}$ ) bands indicated  $sp^2$  hybridization of the carbon atoms while the following ratio of  $I_D/I_G$  mainly defines the graphene oxide, [120], [140], [141]. Figure 9 shows the spectrum of GO in range of  $500\text{--}3200\text{ cm}^{-1}$ , where the broad bands of doublets are located at ca.  $2904\text{ cm}^{-1}$  and ca.  $2692\text{ cm}^{-1}$  in the so-called 2D band. The shift of 2D bands defines the quality of stacking GO layers. The found peak position corresponds to the referenced studies [141], where the centers of D and G bands are located at  $1347.8$  and  $1583.07\text{ cm}^{-1}$  with the ratio of  $I_D/I_G$  (1.02). In Figure 10, the 2D band of the GO is located at ca.  $2692\text{ cm}^{-1}$  defining the GO layered organization. Due to the referenced data, the monolayered GO has a 2D band that occurs at  $2679\text{ cm}^{-1}$ ; the shifted 2D band seems to indicate a multilayered structure of GO.

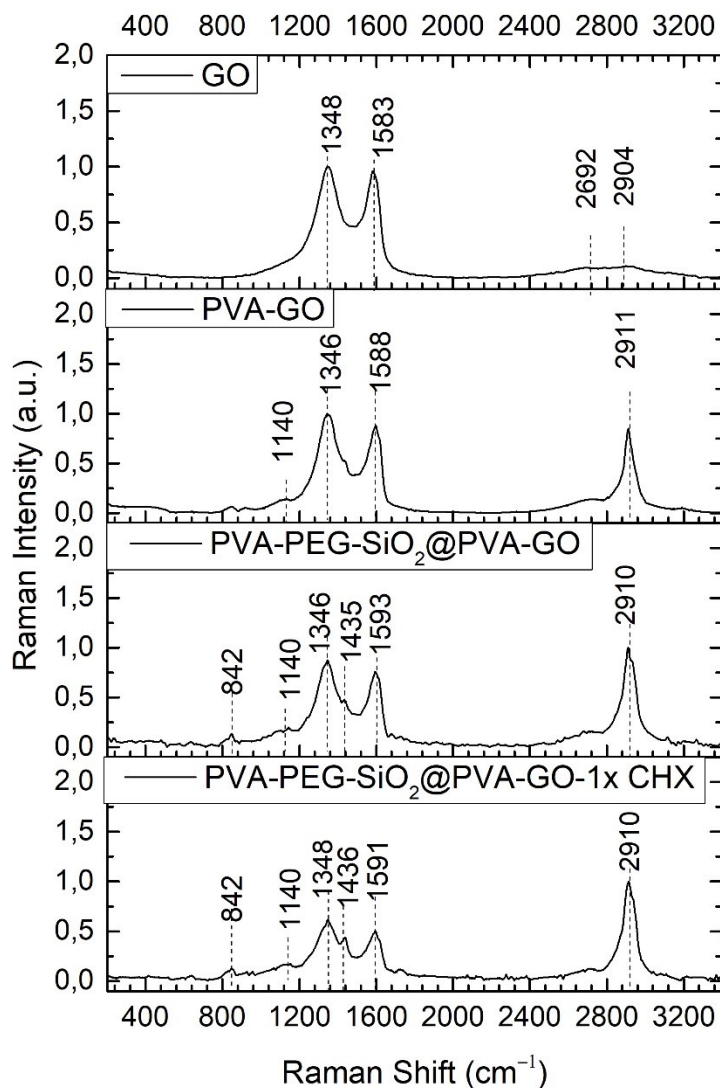


Figure 9. Raman spectra of PVA-based and GO-derived fiber mats in the range of 200 – 3400  $\text{cm}^{-1}$

In Figure 9, the spectra of PVA-GO present the most prominent peak of PVA occurring at ca. 2911  $\text{cm}^{-1}$  due to the  $-\text{CH}_2$  bond vibrations. For the pure PVA spectrum, the peak of  $-\text{CH}$  stretching vibrations was monitored at 1435  $\text{cm}^{-1}$ [142]. The broad band

at the regions of  $1140\text{ cm}^{-1}$  is related to the stretching C–O and C–C stretching bonds within the structure of PVA.

The PVA-GO shell composite shows the peaks of D and G occurred at ca.  $1348\text{ cm}^{-1}$  and  $1595\text{ cm}^{-1}$ , respectively. The obtained peaks relate to the reported studies of GO [143]. The presence of these three peaks in the Raman spectra of PVA-GO composites indicates the distribution of the GO flakes in the PVA-GO fibers. Additionally, a slight shift of 2D bands attributed to the GO is observed at ca.  $2700\text{ cm}^{-1}$  for PVA-GO.

Defining GO,  $I_D/I_G = 1.03$  indicates that the defects of structure for GO with the high reduction degree. Reduced Graphene oxide (rGO) differs in higher conductivity and  $sp^2$  clusters organization that is important to consider for electrospinning process [122], [123]. The ratios of  $I_D/I_G = 1.07$  for PVA-GO and  $I_D/I_G = 1.14$  for core-shell fibers were compared with  $I_D/I_G = 1.03$  for GO, where the higher presence of covalent bonds formed in the electrospun fibers cause the gradual increase of  $I_D/I_G$  [144].

Table 6. Raman bands assignments of GO, PVA, PEG, CHX,  $\text{SiO}_2$

	<b>Raman Shift, <math>\text{cm}^{-1}</math></b>	<b>Band</b>	<b>Ref.</b>
<b>GO</b>	1348	D band	[120], [140], [141], [143]
	1583	G band	[143]
	2692, 2904	2D band	[143]
<b>PVA</b>	1140	C–O and C–C stretching	[135], [144]
	1435	CH stretching	
	2911	CH <sub>2</sub> stretching bond	
<b><math>\text{SiO}_2</math></b>	416	Si–O–Si stretching R band	[145]
	799	Si–O– Si symmetric stretching $\omega_3$	[146]
	976	Si–OH symmetric stretching groups	[146], [147]
	1087	Si–O–Si bending $\omega_4$	

<b>PEG</b>	842	CH <sub>2</sub> rocking	[148], [149]
	1130	C-O, C-C stretching	
	1289	CH twisting	
	2890	CH stretching	
<b>CHX</b>	1600	NH bending	[143], [150]

Figure 10 demonstrates the spectra of PVA-PEG-SiO<sub>2</sub> fiber and contained additives in the range of 200 – 3400 cm<sup>-1</sup>. The spectrum of nanosilica contains the main features such as the broad band centered at 416 cm<sup>-1</sup> and peak at 799 cm<sup>-1</sup>, 976 cm<sup>-1</sup>, 1087 cm<sup>-1</sup>. The band is located at the range 313 – 480 cm<sup>-1</sup> and named R-band, indicating the Si–O–Si stretching vibration bonds. The width of this band is related to the dispersion of the Si–O–Si bond angle [145]. The asymmetric peak of 799 cm<sup>-1</sup> is considered as  $\omega_3$  attributed to the random network of Si–O bonds and the following peak at 976 cm<sup>-1</sup> is attributed to the symmetric stretching vibrations of silanols in SiO<sub>2</sub> ( $\equiv$ Si–OH groups) [146], [147]. The peak  $\omega_4$  located in the frequency of 1087 cm<sup>-1</sup> corresponds to the Si-O-Si bridging bond angle changes. Hence, the found frequencies of freeze-dried silica solution correlate with the referenced studies of nanosilica. However, its presence in the core fiber was not detected clearly, that is a reason to monitor the silica-based composition with help of FTIR method provided in Chapter 4.7.

Figure 10 claims the fingerprints of PEG corresponded to the core composite from the characteristic peak 842, 1289 cm<sup>-1</sup> found in the references [148], [149]. The high-intensive peak of the PEG spectrum located at 2887 cm<sup>-1</sup> relates to the vibrations of

symmetric  $\text{-CH}$  stretching bonds. In conclusion, the presence of NPs of silica could be monitored in the spectrum of the PVA-PEG- $\text{SiO}_2$  fibers by the R-band.

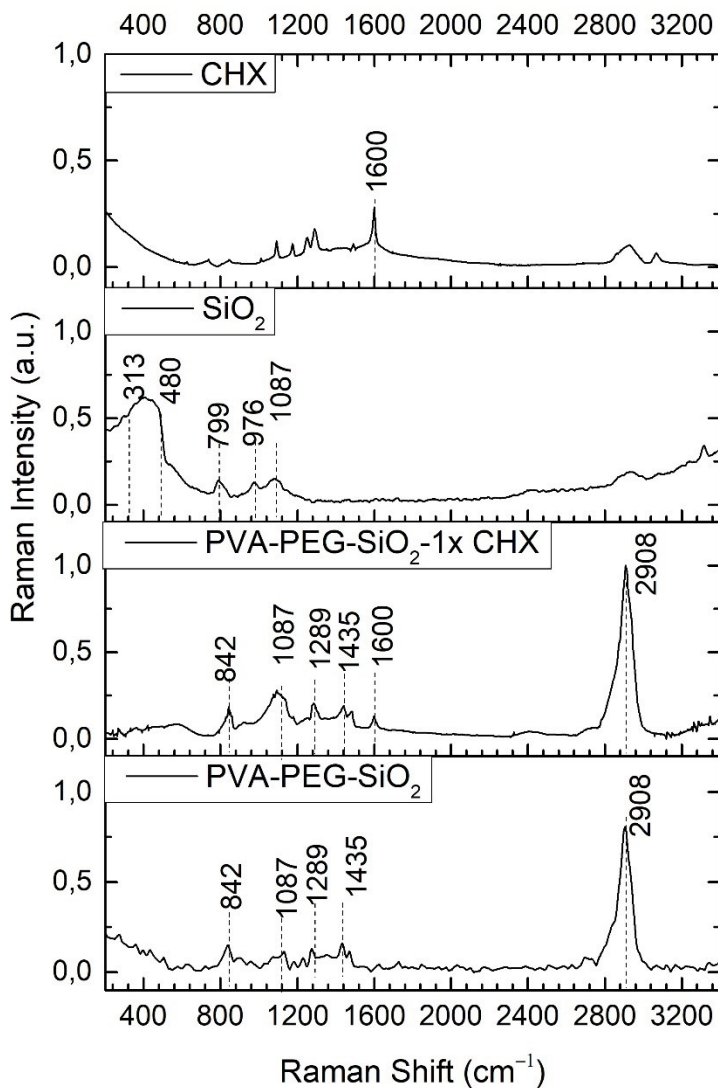


Figure 10. Raman spectroscopy of the synthesized core fiber PVA-PEG- $\text{SiO}_2$  and the constituents of spinning solutions in the range of  $200\text{--}3400\text{ cm}^{-1}$

The spectrum of core fiber loaded with CHX showed the presence of a strong peak at  $1600\text{ cm}^{-1}$  [150], [151]. This peak is assigned to the presence of CHX locally within the

core, however, it is challenging to observe it in the spectrum of core-shell fiber previously given in Figure 9. The G band of GO based material prevents monitoring the encapsulated CHX in the core-shell. Thus, the additional characterization method of encapsulated core-shell fiber is required that should eliminate the input of components.

#### 4.7 FTIR spectroscopy

FTIR spectra of samples were collected in Figure 11. According to the studies, PVA is characterized by the presence of peaks located at  $3331\text{ cm}^{-1}$ ,  $1735\text{ cm}^{-1}$ , and  $842\text{ cm}^{-1}$  for  $\text{-OH}$ ,  $\text{C=O}$ , and  $\text{C-H}$  rocking bonds, respectively [152]. Additionally, the peak located at ca.  $1090\text{ cm}^{-1}$  is attributed to the  $\text{C-O}$  stretching bonds, and the peak of  $\text{C-C}$  stretching bonds at  $1145\text{ cm}^{-1}$  indicates the degree of crystallinity of PVA [128], [153], [154].

In Figure 11, the spectrum of GO has two strong absorption peaks at  $3417\text{ cm}^{-1}$  and  $1735\text{ cm}^{-1}$  assigned to the stretching vibrations of GO as  $\text{-OH}$  and  $\text{C=O}$  bonds attributed to the carboxyl groups of GO [120], [155].

The spectrum of PVA-GO shows the diminished massively peak at  $1735\text{ cm}^{-1}$  and the obvious shift of peak to  $1087\text{ cm}^{-1}$  corresponding to the  $\text{C-O}$  stretching bonds. This shift reports the crosslinking effect of GO by the hydrogen bonds of the GO to the  $\text{-OH}$  groups of PVA. That claims the successful intercalations of GO flakes within the polymer framework.

After the silica addition to the PVA fiber composite, there is a visible shift of peak centered at  $1103\text{ cm}^{-1}$  in the region of  $1100 - 1090\text{ cm}^{-1}$  in Figure 11e. The FTIR spectrum of the PVA-PEG-SiO<sub>2</sub> shows the characteristic peak of asymmetric stretching bonds  $\text{Si-O}$

at  $1103\text{ cm}^{-1}$ , which is mentioned in the references as the presence of Si–O–Si bonds [133]. Following the referenced studies about the silica, the characteristic peaks of silica nanospheres occurred at  $1020 - 1110\text{ cm}^{-1}$  define the asymmetric stretching vibration of Si–O–Si bonds, when the peak of PVA-PEG-SiO<sub>2</sub> fiber mat at  $962\text{ cm}^{-1}$  proves the formation of asymmetric bending and stretching vibration of silanol groups Si–OH [156].

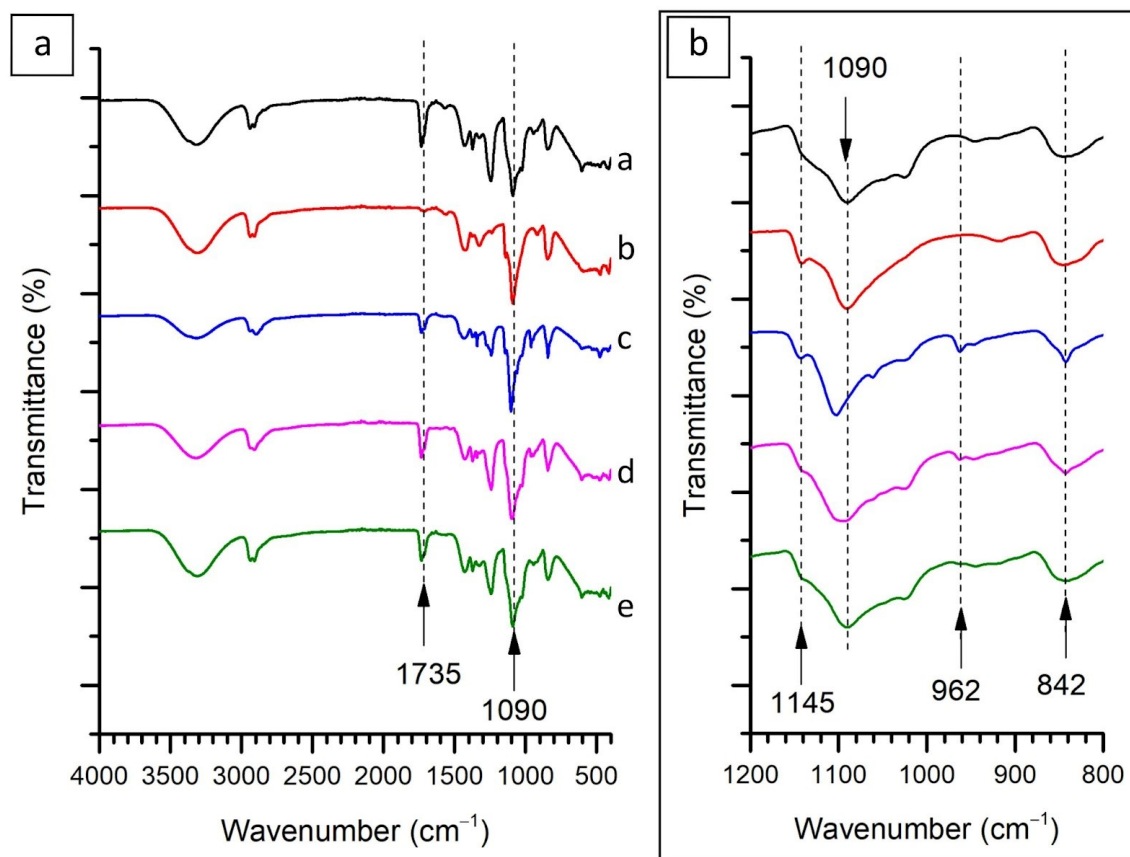


Figure 11. FTIR spectra of the fiber mats: **(a)** PVA 10 wt.% fiber; **(b)** shell PVA-GO; **(c)** core PVA-PEG-SiO<sub>2</sub>; **(d)** core-shell PVA-PEG-SiO<sub>2</sub>@PVA-GO; **(e)** PVA-PEG-SiO<sub>2</sub>@PVA-GO-1x CHX

The spectrum of core PVA-PEG-SiO<sub>2</sub> fiber was given in Figure 11. The increased shoulder (ca.  $1145\text{ cm}^{-1}$ ) defines the silica-polymer interaction in composite, where the Si–O–C bond formed [128]. This bridge effect of silica particles is considered in the

references as the crosslinking approach to establish Si–O–C bonds between the surface of nanosilica and the terminal hydroxyl groups of PVA.

As a result, the FTIR measurements indicate the formation of Si–O–C bonds in the core fiber that affects the mechanical properties of synthesized fibers. FTIR spectra of core-shell fiber PVA-PEG-SiO<sub>2</sub>@PVA-GO and PVA-PEG-SiO<sub>2</sub>@PVA-GO loaded with CHX were compared to find out the crystalline peaks attributed to the CHX. No differences between loaded and pristine fibers were observed that claim that the drug was evenly distributed in the specific core fiber.

Table 7 FTIR bands attributed to the silica, graphene oxide and PVA

	Wavenumber, cm <sup>-1</sup>	Band	Ref.
<b>SiO<sub>2</sub></b>	1108	Si–O asymmetric vibration bonds	[133]
	962	Si–OH asymmetric bending and stretching vibration	[156]
	815	Si–O symmetric vibration	[133]
	460	Si–O rocking motions	[133]
<b>GO</b>	3404	OH stretching	[120],
	2915	CH stretching	[157]
	1733	C=O stretching of carbonyl groups	[157]
	1585-1622	C=C stretching vibration of an aromatic sp <sup>2</sup> carbon bond	[157], [158], [159]
	1622	O-H bending vibration from absorbed water	[123]
	1352	CH deformation of CH <sub>2</sub> and CH <sub>3</sub> groups	[160]
	1225	COH bending deformation of COOH	[157]
	1075	C–O–C stretching of epoxy groups	[157]
	975	CH out-of-plane bending vibrations in the epoxy ring deformation	[157]
<b>PVA</b>	3331	–OH stretching	[152]
	2940	CH asymmetric stretching	[153]
	2910	CH symmetric stretching	[161]
	1415	CH <sub>2</sub> bending	[161]
	1320	CH wagging	[161]
	1145	C=C stretching bond	[128]

	1090	C=O stretching	[153], [154]
	921	CH <sub>2</sub> rocking	[152]
	842	CC stretching	[152], [162]

#### 4.8 ToF-SIMS of Fiber Loaded with Drug

Time of flight (ToF)–secondary-ion mass spectrometry (SIMS) has many potential applications and was used to find out the chemical composition of drug-loaded fibers. Due to the multicomponent composition and dual layered structure, this technique was aimed to trace the CHX encapsulated in the core-shell fiber PVA-PEG-SiO<sub>2</sub>@PVA-GO. The C<sub>22</sub>H<sub>30</sub>Cl<sub>2</sub>N<sub>10</sub> (CHX) is characterized by the several fingerprint peaks occurred at the m/z of 35, 37, 151, 505 [163].

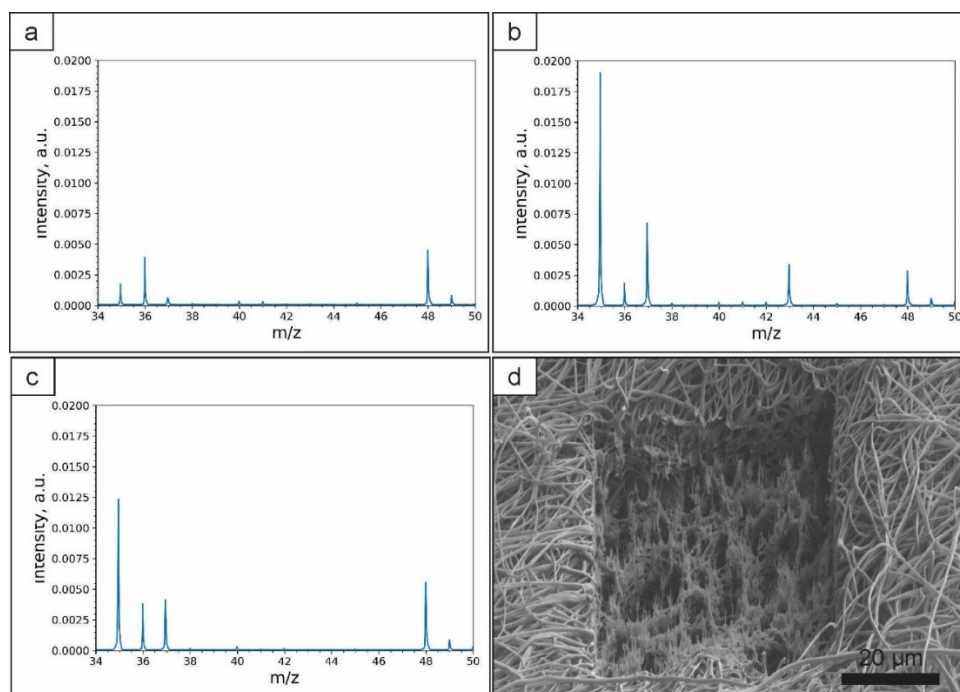


Figure 12. ToF-SIMS spectra obtained in the negative ion mode of core-shell PVA-PEG-SiO<sub>2</sub>@PVA-GO (a); core fibers PVA-PEG-SiO<sub>2</sub>-1x CHX loaded with CHX (b); core-shell PVA-PEG-SiO<sub>2</sub>@PVA-GO-1x CHX (c); SEM image of ion beam-milled PVA-PEG-SiO<sub>2</sub>@PVA-GO sample(d)

The ion of  $C_7H_4N_2Cl$  ( $m/z=151$ ) and the chlorhexidine molecular ion ( $m/z=505$ ) are considered as the most distinctive peaks of CHX [164]. However, the mode of scanning prevents to collect the enough data for a high  $m/z$  ratio (505). In Figure 12 we observe that the chlorine ion intensity ( $m/z = 35$ ) for the CHX-loaded core fiber was higher in 10.7 times than the ‘empty’ core-shell sample. Comparing with the PVA-PEG-SiO<sub>2</sub>-1x CHX core fiber (Figure 12b), the signal ( $m/z = 35$ ) of core-shell fiber with encapsulated CHX performed slight decrease of intensity in 1,6 times.

#### 4.9 XRD

Figure 13 demonstrates the components of the fiber composite. The X-ray diffraction pattern of PVA powder exhibits a sharp peak of crystalline phase located at  $2\theta$  22.71, 26.44 and 47.82° attributed to (101), (200), (102) diffraction planes, respectively [123], [165], [166]. The crystalline regions of PVA-derived fiber mats are defined by the intramolecular and intermolecular hydrogen bonds formed between the hydroxyl groups of PVA and the incorporated components of composite [152], [167]. The main peak of GO is centered at 9.51° corresponding to the (001) plane that reports the intercalation of oxide containing groups such as epoxy, hydroxyl, carbonyl, and carboxyl ones during the chemical oxidation reaction of graphite [123], [141], [168]. Figure 13b shows that the as-received SiO<sub>2</sub> exists in an amorphous phase due to the broad peak (100) centered at  $2\theta = 25.19^\circ$  as mentioned in the references [169], [170], [171].

The XRD spectrum of PVA-GO indicates the existence of the reduced GO by the obvious shift of peak to  $2\theta = 24.91^\circ$  and peak at  $20.68^\circ$  indicating PVA [123], [168]. The

massively diminished GO band at  $9.51^\circ$  demonstrates the great distribution of GO within the PVA-GO composite claiming the inference of FTIR results. That band is assigned to the increased interplanar spacings of GO flakes caused by the PVA intercalation in GO structure [172,173].

The core composition shows the characteristic peaks of PEG located at  $22.25^\circ$  and  $27.16^\circ$  that are correspondent to (120) and (032), respectively [174]. Silica presents in the spectrum with the shift to  $24.84^\circ$  for core PVA-PEG-SiO<sub>2</sub> fiber.

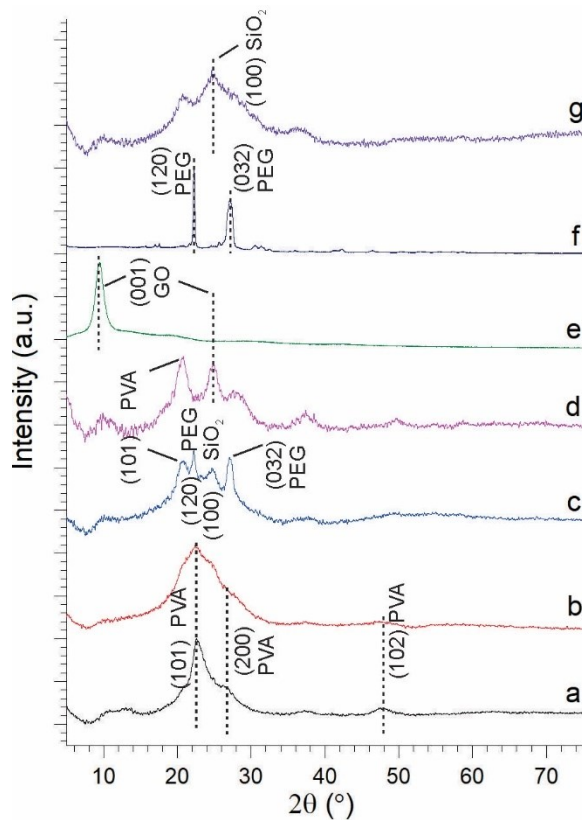


Figure 13. XRD spectra of the components of **(a)** PVA powder; **(b)** PVA fiber; **(c)** core PVA-PEG-SiO<sub>2</sub> fiber; **(d)** shell PVA-GO fiber; **(e)** GO; **(f)** PEG powder; **(g)** Silica

In Figure 13 there was observed the amorphous nature of produced fiber composites. The sharpness of PVA crystalline peak decreases after the addition of

nanomaterials. The peak parameters with addition of nanomaterials are included in Table 8. In the next Chapter, the DSC measurements were conducted to define the crystallinity of composites.

Table 8. Diffraction peaks of fibers and components

Name	2 $\theta$ , °	FWHM, Rad
PVA fiber	22.38	0.0353
PVA-GO fiber	20.67	0.0135
PVA-PEG-SiO <sub>2</sub> fiber	20.71	0.0118
PVA powder	22.84	0.0275
GO	9.42	0.0094
Silica	25.07	0.0852

#### 4.10 Differential Scanning Calorimetry (DSC)

Due to the availability of the DSC method to trace the phase transformation temperatures and the quantification of transformation enthalpies, DSC curves provide information about the phase transition temperature of samples given in Figure 14.

DSC measurements of PVA-based fiber mats indicated the glass transition and melting point peaks occurred at ca. 57 °C and ca. 230 °C, respectively [82], [175], [176]. PVA-GO fiber mat demonstrated two endothermic peaks located at 57.3 °C and 227.4 °C. DSC curve of PVA-PEG-SiO<sub>2</sub> showed the highest peak at 57 °C and low intensive peak at 201.7 °C. The core-shell fiber mat consisting of the core PVA-PEG-SiO<sub>2</sub> and shell PVA-GO demonstrates a narrowed peak at 57.4 °C and a broad peak at 201.7 °C. The melting temperature for core and core-shell composition seems to be reduced from 227.4 °C to ca. 202 °C due to the amorphous silica and PEG presence.

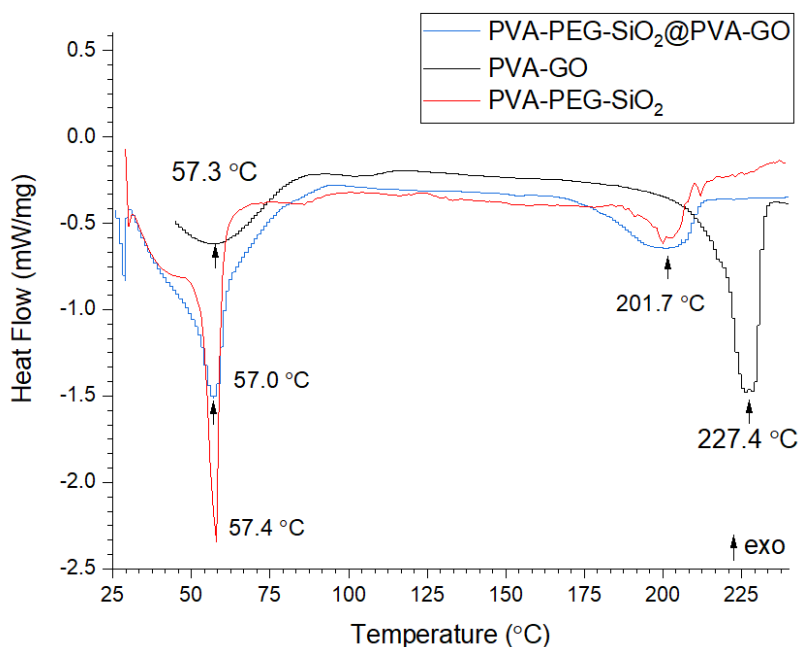


Figure 14. DSC curves of samples with the following compositions: shell PVA-GO fiber mat; core PVA-PEG-SiO<sub>2</sub> fiber mat; core-shell PVA-PEG-SiO<sub>2</sub>@PVA-GO fiber mat

The calculated results of the degree of crystallinity for samples and melting temperature are demonstrated in Table 9.

Table 9. Degree of crystallinity and melting temperature of fiber mats

Name	T <sub>m</sub> , °C	T <sub>g</sub> , °C	Heat of melting (ΔH <sub>m</sub> ), J/g	Degree of crystallinity, %
Shell PVA-GO	227.4	57.3	83.02	59.90
Core PVA-PEG-SiO <sub>2</sub>	201.7	57.0	24.49	17.67
Core-shell PVA-PEG-SiO <sub>2</sub> @PVA-GO	201.7	57.4	48.18	33.32

During the thermal characterization of shell, core and core-shell fiber mats, the growth of melting temperature is noted for the PVA-GO composite. The melting temperature is associated with the coordinated movement of several polymeric molecules defining the state of structure flexibility [25]. After adding of crosslinking agent such as

GO, the movement of molecules becomes limited that requires the higher energy input to promote the spatial movement of the monomer chains. That demonstrates the impact of GO to the increase of crystallinity degree of polymer composite. In the relevant study, the PCL-GO based composite showed the higher degree of crystallinity compared to the pristine PCL which confirmed the efficient function of GO as the modifying agent towards the higher mechanical resistance [177]. Our results show the chemical structure modification with GO results in the increased degree of crystallinity and melting temperature. In the following Chapter the mechanical properties of GO derived composites were studied with the micro tensile tests.

#### **4.11 Mechanical Tests**

The stress-strain curves of tested samples are shown in Figure 15. The results of tensile measurements and elastic modulus of the core, shell, and core-shell fiber mats are included in Table 10. The double-notched samples were cut from the composites: PVA-GO 10% as a shell, PVA-PEG-SiO<sub>2</sub> as a core, and PVA-PEG-SiO<sub>2</sub>@PVA-GO core-shell fiber mat. The tensile test of core (PVA-PEG-SiO<sub>2</sub>) fibers demonstrates the reduced value of elongation at break in comparison with the PVA-GO shell. The presence of silica nanoparticles exerts the discontinuity in composite to cause faster failure at  $1.49 \pm 0.25$  % of strain.

Table 10. The tensile properties of PVA-PEG-SiO<sub>2</sub>@PVA-GO, PVA-PEG-SiO<sub>2</sub> (core), and PVA-GO (shell) fibers

Name of Sample	Thickness, $\mu\text{m}$	Average Diameter, nm	Density, $\text{mg}\cdot\text{cm}^{-3}$	Elastic Modulus, MPa	Strength, MPa	Elongation at Break, %
shell PVA-GO 10%	50	$174 \pm 31$	$114 \pm 20$	$19.91 \pm 1.67$	$0.62 \pm 0.10$	$7.07 \pm 2.29$
core PVA-PEG-SiO <sub>2</sub>	55	$381 \pm 131$	$147 \pm 22$	$263.17 \pm 96.24$	$3.65 \pm 1.75$	$1.49 \pm 0.25$
core-shell PVA-PEG-SiO <sub>2</sub> @PVA-GO	32	$261 \pm 51$	$119 \pm 7$	$35.89 \pm 9.70$	$0.77 \pm 0.29$	$3.97 \pm 1.37$

However, the PVA-GO fiber mat shows an extended period of tensile deformation, where the fracture occurred at  $7.07 \pm 2.29$  % of elongation. The core-shell fiber mat demonstrates the damage of samples starting at  $3.97 \pm 1.37$  % of strain.

The mechanical performance of core-shell fibers is complex, thus attributed to the input of core and shell parts. Tensile strength of PVA-GO fibers was the highest among the tested sample. Notably, the mean diameter of tested PVA-GO fibers is  $174 \pm 31$  nm that correlates with the references reporting that nanofibers with smaller dimension have a greater tensile strength [178], [179]. The increased resistance of tensile stress performs the synergetic impact of GO in the shell of core-shell composite with the inner core diameter  $173 \pm 25$  nm (Section 4.2 Confocal Laser Fluorescence Microscopy Characterization). The result of core-shell fiber presents that the nanomaterials create the well-bonded system which evenly exerted the applied load along the composite.

The dimension and density of PVA-PEG-SiO<sub>2</sub> mat should be noted, where the bulkiest sample with the highest fiber dimension performs the brittle glassy behavior with the elastic modulus of  $263.17 \pm 96.24$  MPa with the break at  $1.49 \pm 0.25$  % of strain. When the core-shell PVA-PEG-SiO<sub>2</sub>@PVA-GO fibers with the associated GO crosslinkers showed the elastic modulus of  $35.89 \pm 9.70$  MPa with the break of sample prolonged at  $3.97 \pm 1.37$  % of strain.

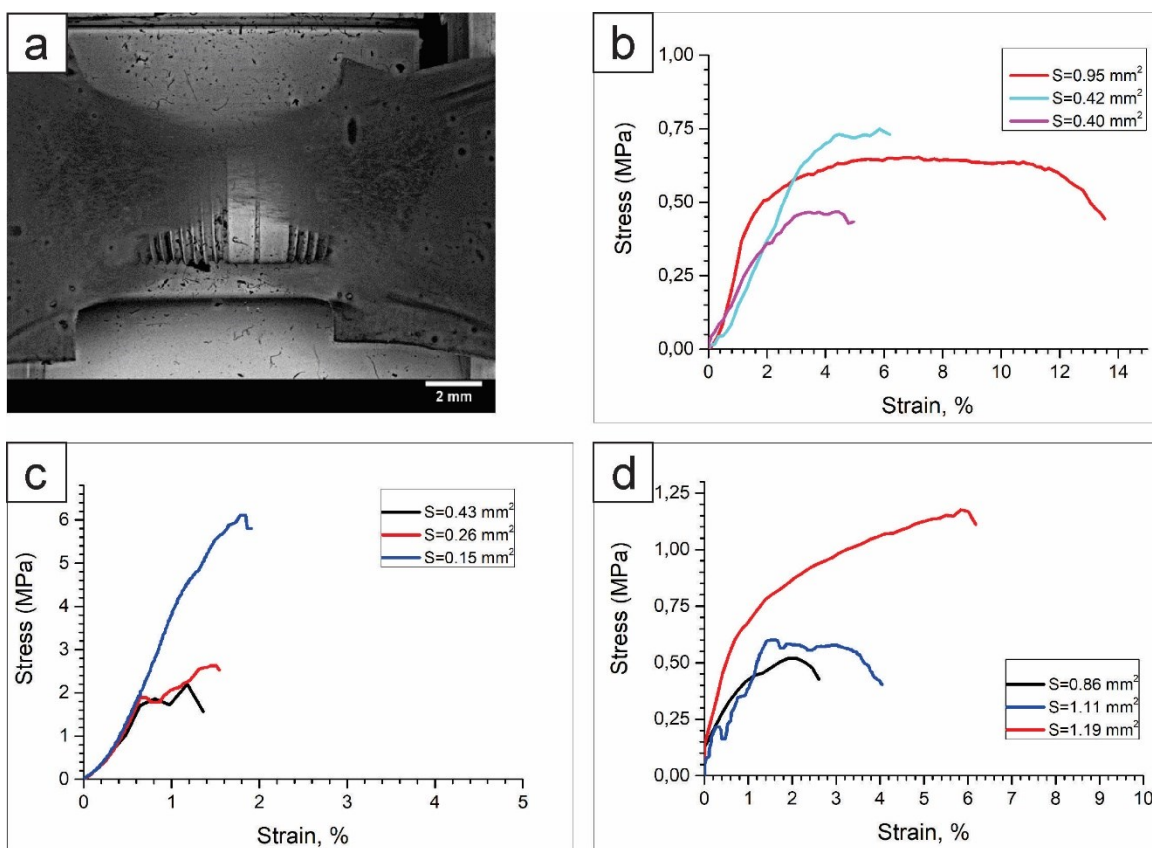


Figure 15. Core-shell fiber mat mounted in Deben device (a); stress-strain curves with the cross-sectional areas of fiber mats: PVA-GO shell (b); PVA-PEG-SiO<sub>2</sub> core (c), PVA-PEG-SiO<sub>2</sub>@PVA-GO core-shell (d)

The PVA-GO composite serves as a protective shield for the core fiber and demonstrates higher resistance to the tensile stress. Incorporation of GO based shell in the core-shell structure with its potential drug loading capacity is speculated as a direction to the functionality of coaxial electrospinning [180], [181]. Considering the wound healing application, among the requirements to the chemical composition, there are certain requirements to mechanical properties of fiber matrix. Since the cell affinity and attachment are sensitive to the morphology and have tendency to proliferate in the areas

with a higher stiffness [65], [66]. On the way to the selection of suitable scaffold materials, the fiber mats need to present the certain stiffness and dimension.

#### **4.12 UV-Vis Spectral Analysis of Fiber Mats**

##### *Analysis of Fluorescence Spectra*

The obtained shell, core and core-shell PVA-PEG-SiO<sub>2</sub>@PVA-GO fiber mats were studied to trace their degradation in a medium close to the body conditions. There are the spectra of samples dissolved in PBS medium in Figure 16. GO is pH-sensitive photoluminescent material that could be monitored with UV spectroscopy. The spectrum of the GO is characterized by the prominent peaks occurring at the blue band (ca. 440 nm) and long-wavelength band (ca. 700 nm) in the solution pH 2.5. It is reported that, the higher pH of medium facilitates the increase of peak intensity in the blue band [182]. The blue band is merely observed for the GO contained fibers in the PBS buffer solution (pH 7.4). Due to the higher pH 7.4 used in our experiments, the presence of GO after the crosslinking with methanol was claimed by the blue band emission at ca. 400 – 415 nm, 425 nm, 480 nm excited with 295 nm, 330 nm, 415 nm, respectively. After the excitation with the laser wavelength 330 nm, there are strong blue bands centered at 425 nm and clearly observed for all GO-based samples. When in case of 295 nm there was a shift of spectra in the region with the low accessible region of observations. In case of 415 nm, there was a strong shift of blue band emission to the 480 nm. Hence, the direct dependence of the spectra intensity from the laser source excitation was traced.

In Figure 16c, the secondary emission at 580 nm is observed for the as-received core-shell PVA-PEG-SiO<sub>2</sub>@PVA-GO fibers. The peak (580 nm) of the non-crosslinked core-shell sample can be attributed to the oxidized debris potentially formed after the fiber degradation [183]. The dissolution of PVA and PEG increased the number of oxidized chemical bonds such as –COOH on the GO surface affecting the size of GO sheets. According to the mentioned above reference, the optical properties of oxidized debris in core-shell fibers are close to GO-originated quantum dots. That fluorescence effect develops another application as bioimaging and photocatalysts [118].

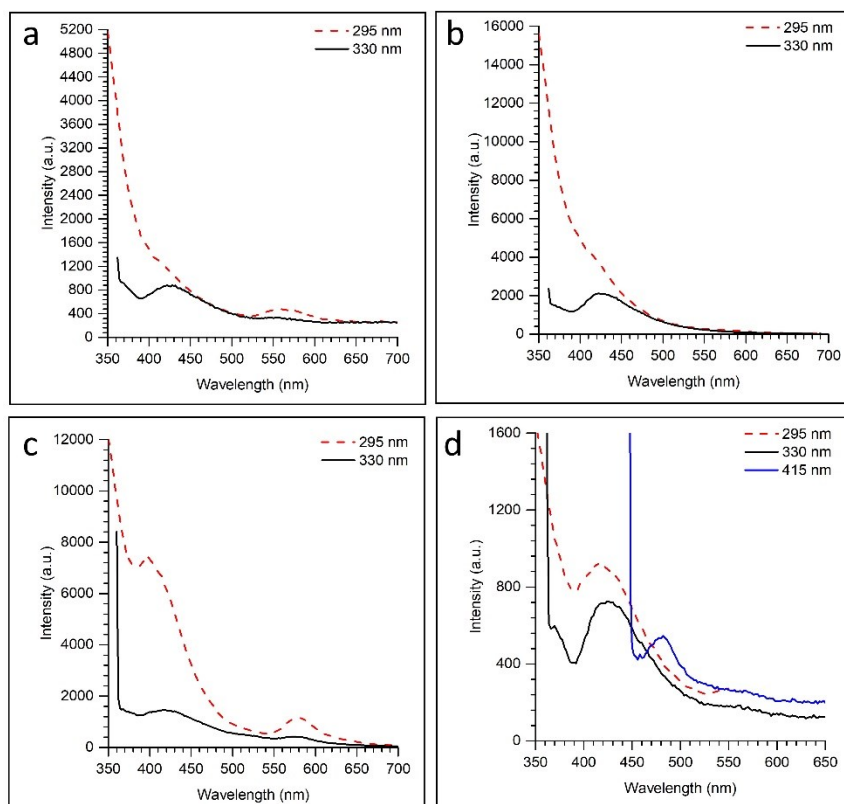


Figure 16. Fluorescence spectra excited with the different sources for the shell PVA-GO 5 % fibers (a); shell PVA-GO 10 % (b); core-shell PVA-PEG-SiO<sub>2</sub>@PVA-GO (c); crosslinked core-shell PVA-PEG-SiO<sub>2</sub>@PVA-GO (d)

The fluorescent emission of GO is sensitive to the pH of medium and the excitation wavelength. The consideration of these parameters is crucial to study the degradation behavior of GO-based composite.

#### *Analysis of Absorbance Spectra*

The *in vitro* release of medicated fiber mats was studied. The absorption spectra were used to calculate the drug release. The magnitude of absorption is governed by the Lambert – Beer law, where  $\epsilon$  is an extinction coefficient depending on sample,  $c$  is the molar concentration of solution,  $l$  is a path that light passes through.

$$A = \epsilon cl \quad (16)$$

The concentration of released agents ( $C_t$ ) was calculated from the given equation, where the optic density ( $O.D.$ ) was gained from the absorbance spectra of fiber mats incubated in the test tubes within the time.  $C_t$  is the calculated concentration of drug (mg/mL) released for the time.

$$C_t = \frac{O.D.-intercept}{slope} \quad (17)$$

The calibration curves were built using the absorbance spectra to calculate the slope and intercept. A linear regression for each loading agent was obtained in the calibration curves (Supplementary materials, Figure S6-S10). UV-Vis spectrophotometer confirmed the absorption peak of chlorhexidine at 255 nm as mentioned in the studies [184], the absorption peak of GO at 295 nm [185], ICG at 790 nm [186], DOX at 482 nm [187], MB at 608 nm [188]. The absorption spectra of GO composites have a strong intensive band at 230 nm and shoulder at 295 nm attributed to the  $\pi$ - $\pi^*$  and  $n$ - $\pi^*$  interactions, respectively

[189]. In the GO release calculations, the optic density at 295 nm was used due to the operational parameters of spectrophotometer.

The optic density of the characterization bands was used to calculate the concentration of the loaded agents and GO release as a parameter of fiber degradation.

The drug release profiles were obtained by plotting the cumulative release versus time:

$$Q_t = \frac{M_t}{M_\infty} \quad (18)$$

$Q_t$  is the cumulative fraction,  $M_t$  is the amount of released drug at time  $t$ , and  $M_\infty$  is the total amount of loaded drug.

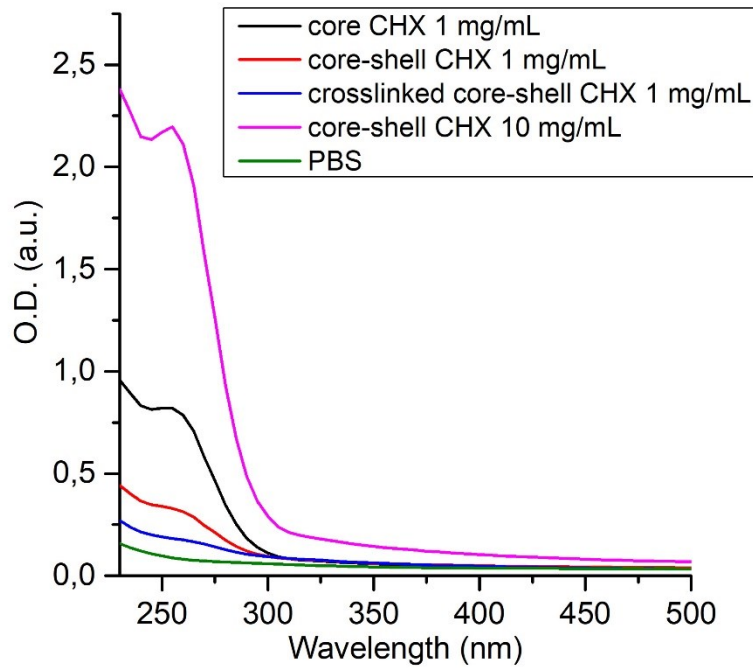


Figure 18. Absorbance spectra of core, core-shell, methanol crosslinked core-shell fiber loaded with CHX

The loading and encapsulation efficiency was calculated from the concentration of loaded agent found from optic density of absorbance spectra in Figure 19.

Figure 19a gives the linear dependence of the CHX loaded in core and the released drug concentration from PVA-PEG-SiO<sub>2</sub>@PVA-GO fiber mats. Where the initial drug concentration is known in the core solution, and the pristine concentration of CHX is calculated from the full dissolved the core-shell fibers.

Silica based of PVA-PEG-SiO<sub>2</sub>@PVA-GO-1x CHX core-shell showed higher encapsulation efficiency of  $1.02 \pm 0.27$  %, where silica nanoparticles capture chlorhexidine more efficiently supporting higher codelivery function. When core-shell with no silica PVA-PEG@PVA-GO-1x CHX presents the encapsulation efficiency with  $0.16 \pm 0.05$  % in Figure 19b.

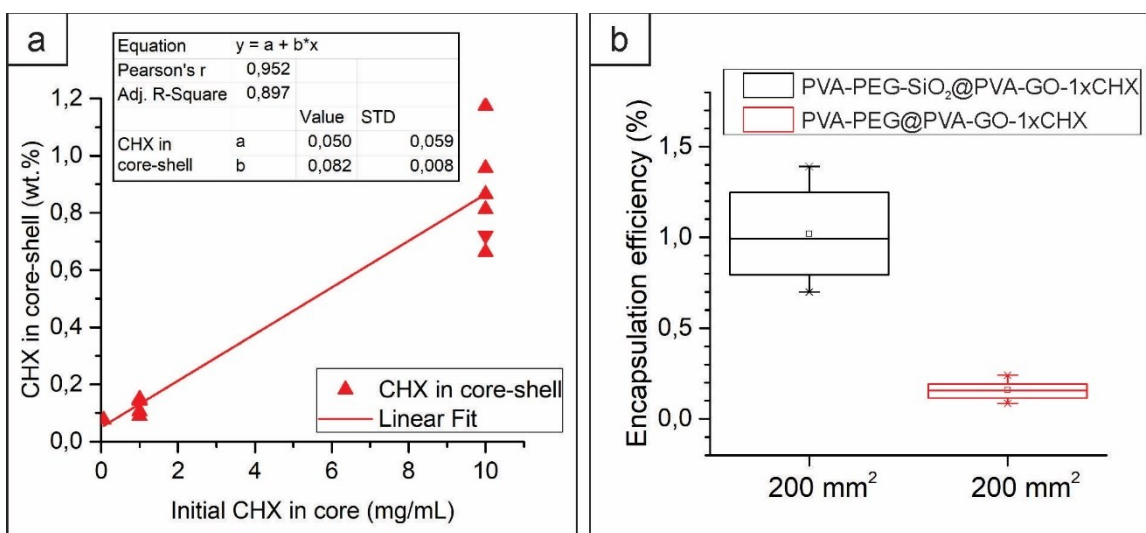


Figure 19. Loading efficiency of PVA-PEG-SiO<sub>2</sub>@PVA-GO core-shell with the initial loading of CHX in the core (a); Encapsulation efficiency of PVA-PEG-SiO<sub>2</sub>@PVA-GO-1x CHX against PVA-PEG@PVA-GO-1x CHX core-shell fibers

The release rate of core and PVA-PEG-SiO<sub>2</sub>@PVA-GO-0.1x CHX core-shell with the loading of CHX 1 mg/mL was compared in Figure S11, Supplementary Materials. The data showed the good fitting to the Korsmeyer – Peppas model. The *n* values were 0.61 and 0.54 for core and core-shell, respectively.

The release profiles of CHX loaded fibers were studied by fitting to Zero-order, First-order, Higuchi, and Korsmeyer – Peppas kinetic models. Figure 20 and Figure 21 demonstrated the CHX release from PVA-PEG-SiO<sub>2</sub>@PVA-GO-1x CHX core-shell fibers and PVA-PEG@PVA-GO-1x CHX coated samples with initial loading of 10 mg/mL in the core. Core-shell fibers provided the 100 % cumulative release after 5 h.

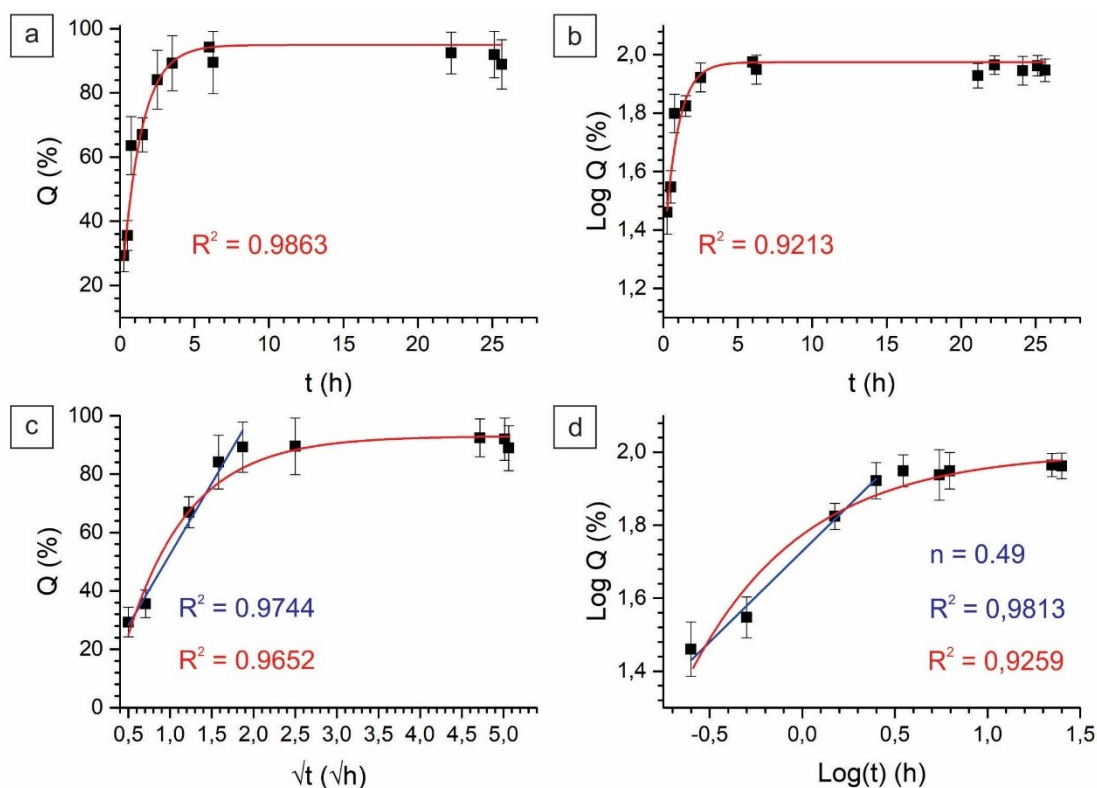


Figure 20. CHX release of PVA-PEG-SiO<sub>2</sub>@PVA-GO-1x CHX fitted to (a) Zero Order; (b) First Order; (c) Higuchi model; (d) Korsmeyer – Peppas model

Table 11 Release mechanisms of medicated nanofibers

	Release exponent $n$	Diffusion Mechanism	Substance Released	Concentration, mg/mL
core-shell PVA-PEG-SiO <sub>2</sub> @PVA-GO-1x CHX	0.49	Non -Fickian	CHX	10
core-shell PVA-PEG @PVA-GO-1x CHX	1.43	Erosion/Relaxation	CHX	10

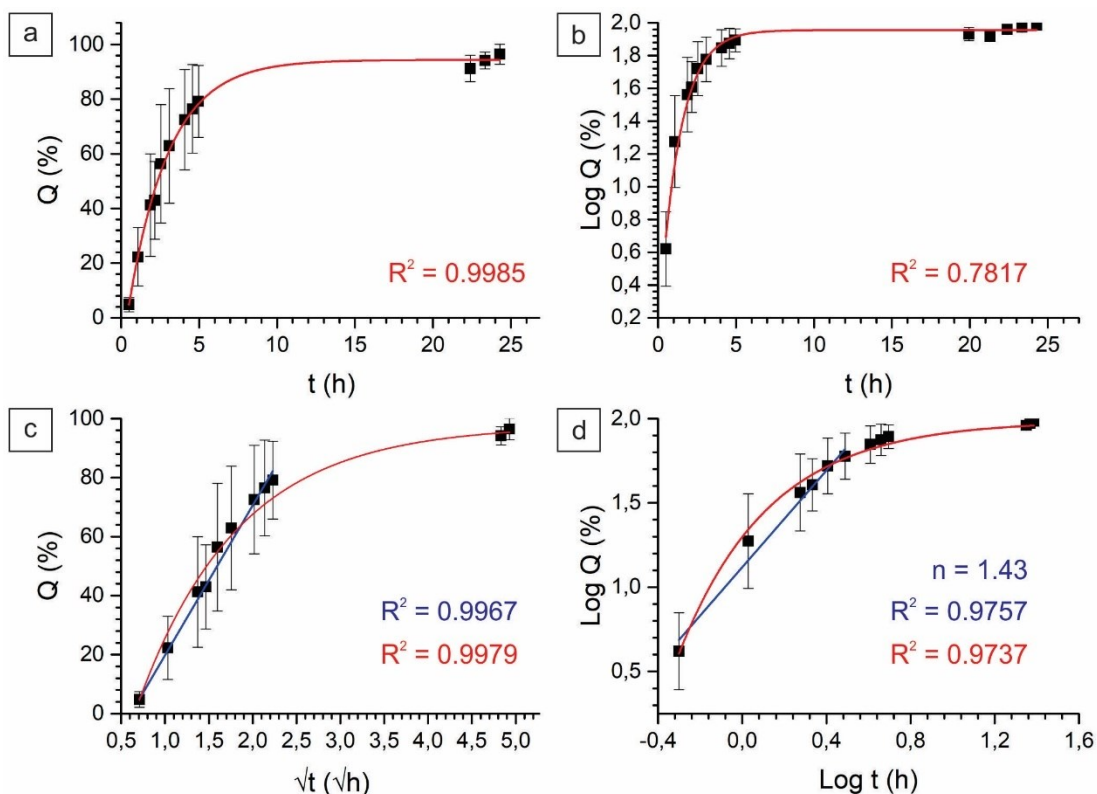


Figure 21. CHX release of PVA-PEG @PVA-GO-1x CHX core-shell fibers fitted to **(a)** Zero Order; **(b)** First Order; **(c)** Higuchi model; **(d)** Korsmeyer – Peppas model

In the relevant study, *Cui et al.* investigated the drug kinetics of PVA based films that was fitted to Korsmeyer – Peppas equation and exponential factor  $n$  demonstrated a Fickian mechanism [190]. Thus, the drug release mechanism of pure PVA films was ruled by the Fickian diffusion, while the produced PVA-PEG-SiO<sub>2</sub>@PVA-GO core-shell fiber mats demonstrated non-Fickian mechanism of release with  $n = 0.49$  (Table 11).

It should be mentioned that the release of water-soluble drugs loaded in the non-swelling matrix mostly performs the First Order model [191]. In Figure 20 and Figure 21, the release profiles of produced fiber samples were better correlated with the Korsmeyer – Peppas and Higuchi models as in the relevant studies [12], [192]. Good correlation to the

Higuchi model indicates the case where drug release is provided by the diffusion within the pore heterogeneous matrix. The release exponent value of PVA-PEG@PVA-GO ( $n=1.43$ ) indicates the high rate of erosion of polymer matrix in Figure 21.

Non-Fickian diffusion of silica containing hydrogel depicts the case where the rate of the polymer chain relaxations is significantly slower than the rate of the molecule diffusion within the polymer hydrogel [193]. That provides the sustainable drug release of PVA-PEG-SiO<sub>2</sub>@PVA-GO compared with the non-silica core-shell composite.

The mechanism of fiber degradation was assessed by the released GO concentration, where the data of PVA-PEG-SiO<sub>2</sub>@PVA-GO core-shell fibers were compared in Table S2. The R<sup>2</sup> value of GO release profiles shows good correlation with Higuchi and best fitted to the Korsmeyer – Peppas models (Supplementary Materials, Figure S12). The release exponent ( $n$ ) demonstrates that the fiber degradation is mostly controlled by the non-Fickian mechanism. Considering this, the presence of GO results in the swelling of core-shell fiber mat and facilitates the hydrogel formation in PBS medium. The GO based hydrogel with water uptake capacity alters the drug release mechanism. Summarizing the findings, we could conclude that the nanosized silica and graphene oxide make significant contribution to sustainable drug release.

### 4.13 Antibacterial Test

#### *Disk diffusion method*

All CHX encapsulated core-shell fiber mats showed antibacterial activity with the obviously traced inhibition halo in Figure 22. CHX loaded PVA-PEG@PVA-GO-CHX (P) performed the  $71.92 \pm 2.48$  % of inhibition zone when the control C+ was assumed as 100 %. Samples with silica PVA-PEG-SiO<sub>2</sub>@PVA-GO-CHX from separate groups (S1, S2) performed less inhibition zone. For S1 sample, the inhibition zone reached  $58.99 \pm 2.03$  %, when S2 with increased time of synthesis provided a bigger inhibition zone with  $65.32 \pm 1.66$  %.

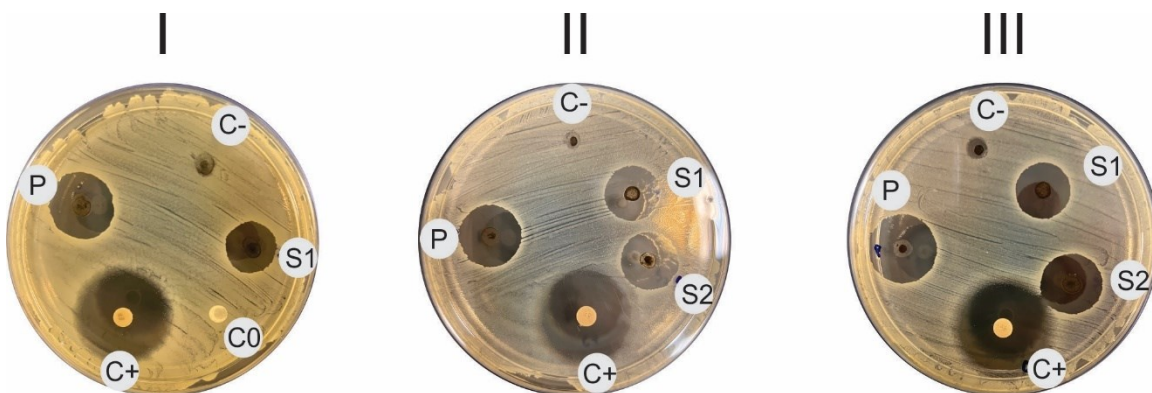


Figure 22. Disc diffusion assay of core-shell fibers PVA-PEG-SiO<sub>2</sub>@PVA-GO (C-); PVA-PEG-SiO<sub>2</sub>@PVA-GO-1x CHX (S1, S2); PVA-PEG@PVA-GO-1x CHX (P); cellulose disk (C0); cellulose control with doxycycline (C+) against *S. aureus*

The bacterial response was received, where the effective concentration of CHX (0.1x, 1x) was demonstrated using the optical density determination of bacterial cultures at OD = 600 nm (Supplementary Materials, S13).

According to the results of cultivation in PVA-PEG-SiO<sub>2</sub>@PVA-GO as a control C+, the adaptive *lag phase* lasted up to 2 h of the experiment. Based on the background of the formation and preparation of enzymatic complexes of bacterial cells, the exponential

transition phase was observed from 2 to 8 h, divided in the stages: P1 – a period of acceleration (2 – 4 h), P2 – a period of intensive logarithmic cell growth (4 – 6 h), P3 – a period of decaying growth (6 – 8 h).

By the sixth hour of the experiment, a key indicator of optical density ( $\alpha$ ) was achieved, characterizing the maximum value of colony-forming units in this period  $OD_{600\text{ nm}} = 3.25$ . The period of decaying growth (6 – 8) was marked by a decrease in the speed of generative processes. The second key point was reached with an optical density that corresponded to the M-concentration for microorganisms  $OD_{600\text{ nm}} = 3.78$  at 8 h. At the interval of 8–14 hours, the phase of the stationary position of the cells was observed, without significant fluctuations with the mean  $OD_{600\text{ nm}} = 3.88$  in this  $\beta$  segment (8–14 h). After 16 h, there was a phase of gradual death of bacterial cells.

Compared with the control C+, the studied sample PVA-PEG-SiO<sub>2</sub>@PVA-GO-0.1 CHX showed the increase of  $\alpha$  and  $\beta$  indicators by 13 % and 5.3 %, relatively without relapsed *lag phase*. The cultivation results of the sample PVA-PEG-SiO<sub>2</sub>@PVA-GO-1x CHX showed an extension of *lag phase* up to 30 h, followed by acceleration of bacterial growth relatively to control values with the indicators: the  $\alpha$  – increase by 30%, the  $\beta$  – increase by 16%.

Agar disc diffusion assay accompanied with the spectrophotometric method claims the antibacterial activity of core-shell samples encapsulated with the CHX against the Gram-positive bacteria *S. aureus*. Where PVA-PEG-SiO<sub>2</sub>@PVA-GO-1x CHX sample performed interesting results of extension of adaptive lag phase compared with PVA-PEG-SiO<sub>2</sub>@PVA-GO-0.1 CHX with the decreased concentration of CHX loading in 10 times.

#### 4.14 Cell Viability Assay

The cell viability of core-shell and core-shell fibers crosslinked with methanol was studied to assess biocompatibility of composites. The effect of GO-based biomaterials on viability of the primary human fibroblast cells was evaluated.

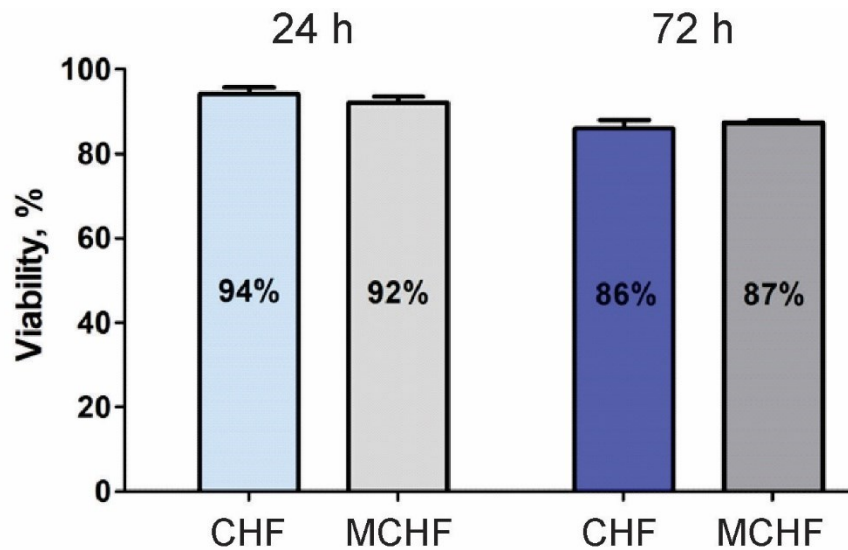


Figure 23. Cell viability assay of PVA-PEG-SiO<sub>2</sub>@PVA-GO core-shell fibers (CHF) and methanol crosslinked core-shell fiber mats (MCHF)

As-prepared and methanol processed core-shell fibers do not perform acute toxicity after 24 hours, but affect cell survival or proliferation after 72 hours. Considering the biocompatibility, we could conclude that the electrospun core-shell fiber mats could be potentially applied to develop the wound dressings.

## Chapter 5. Future Prospects

### *Patterned core-shell fiber mats*

To summarize the outcomes of study, we found out the dimension, core-shell structure of fibers is a defining parameter for the drug release. Considering wound dressing application, a micropatterned electrospun mat could be introduced to increase the concentration of drugs as suggested in the relevant studies by Prof. G. Sukhorukov's group [136,137]. Besides, patterning along with the alignment of fibers is an interesting direction toward the increased bulkiness of the synthesized material and topography to solve the tasks of cell affinity [65] and microfluidics [194].

### *Encapsulation with antibiotic DOX and fluorescent dyes*

The design concept of PVA-PEG-SiO<sub>2</sub>@PVA-GO core-shell is aimed to utilize fiber composite for varied drug encapsulation. To prove the concept, the medical agents were placed in the core solution PVA-PEG-SiO<sub>2</sub> such as antibiotic DOX, fluorescent labels MB, ICG with the concentration of 16 mg/mL, 0.1 mg/mL, 0.2 mg/mL, respectively. The obtained core solutions were used to synthesize the medicated core-shell fiber mats. The calibration curves were built from the UV absorbance spectra with the concentrations of DOX (0.10000 – 0.00625 mg/mL) and MB (0.0031 – 0.00020 mg/mL), ICG (10<sup>-6</sup> mg/ml – 10<sup>-2</sup> mg/ml) in 0.01 M of PBS medium, respectively.

Figure S14 demonstrates the absorbent efficiency of GO after the loading of fluorescent dyes ICG and MB in the core of layered fibers. The initial concentration of agents is vividly observed after ultrasound (US) sonication aimed to fully dissolve the fibers. The characteristic peaks of ICG and MB is seen at 790 and 609 nm of wavelength.

During the time of release, the complete disappear of dyes is noticed. Figure S14a claims that core-shell fiber with the initial concentration of ICG 0.2 mg/mL shows no presence of ICG peak instantly after 15 min during 240 min of test. When the spectrum of US treated fiber showed the presence of ICG with the calculated concentration 0.005 mg/mL.

Figure S14b shows the absorption spectra of core-shell fiber with a core loaded with MB released from time and a spectrum of the core with MB. The initial MB concentration is 0.1 mg/mL in the core fiber. The spectra of core-shell fibers with the same loading of MB demonstrate that there is no trace of MB peak from 17 min till 1144 min of experiment.

The release of antibiotic Doxorubicin (DOX) encapsulated in the core of PVA-PEG-SiO<sub>2</sub>@PVA-GO was studied. The regression coefficients ( $R^2$ ) of mathematical models and the release exponent  $n$  of the Korsmeyer – Peppas model were calculated from the experimental release data (Figure S15, Supplementary Materials). The release exponent  $n = 0.86$  indicated the non-Fickian diffusion of DOX as for CHX loading. The release profiles of DOX medicated fibers are characterized as the burst release of 90% at the first 6 h of release in Figure S16. The release profile of water swelling chitosan composite also demonstrates the same trend separated in two release stages [195]. Summarizing this, the swelling PVA-PEG-SiO<sub>2</sub>@PVA-GO fiber composite supports the encapsulation with antibiotics and fluorescent dyes, that broadens the application areas.

#### *Hydrophobic dip-coating to prolong the drug release*

One of interesting approaches is to prove the concept of dip-coating with hydrophobic polymer, aimed to relapse the drug release (Supplementary materials Figure

S17). The release of PHB dip-coated core-shell fibers was prolonged up to 50 h. Due to the hydrophobic coating, the diffusion rate was slowed down, that retarded the swelling and depletion of sample with the subsequent release.

## Chapter 6. Conclusion

In this work the morphology, chemical structure and physical properties of synthesized fibers were carefully investigated. The full characterization included the study of the composition and parameters of spinning solutions (e.g., such as viscosity and temperature) and their effects on the produced fibers. The results were summarized to assess the contribution of components such as SiO<sub>2</sub> and GO made to the coaxial electrospinning technology. This analysis allowed establishing the optimal operational window for the continuous electrospinning of coaxial fibers. The core and shell compositions were studied in terms of their utilization for the fiber production. The produced coaxial fiber consisted of the core PVA-PEG-SiO<sub>2</sub> as a drug carrier and protective shell PVA-GO compositions.

The electrospinning set up developed in the current project resulted in the single material (core) fibers being collected with the efficiency up to 66 %, whilst the core-shell fibers were collected with the efficiency up to 33 % (evaluated based on 1 h synthesis). Despite this apparent decrease for core-shell coaxial fibers compared to the monoaxial fiber formation, this decrease was considered to be a minor disadvantage in view of the major improvements in the resulting mechanical and functional properties of the fiber mats. The efficiency of the electrospinning process depends on the laboratory set up and affords the further improvements.

Based upon the spectroscopic measurements, the mechanism of interface reactions was proposed as schematically illustrated in Figure 24. The analysis of Raman and FTIR spectra contributed to elucidating the interactions within the fiber, where the crosslinking

effects were detected following the addition of silica and graphene oxide (GO). Nano silica and graphene oxide were found to affect the fiber dimensions by forming new bonds within the polymer matrix affecting the fiber formation. Silanol groups at the surface of silica support the polymer-nanoparticle interactions via bonding with the hydroxyl groups of PVA. Colloidal silica nanoparticles are characterized by the high surface to volume ratio that promote the release of ionized groups from the drugs.

Carbonyl and hydroxyl groups of GO facilitate the crosslinking of PVA molecules. The bridging effect of GO-containing composite was confirmed through the observed effects on the fiber morphology and the water uptake. Graphene oxide extended the characteristic degradation period of fiber mats by the mechanism of massive swelling and hydrogel formation after being stored in deionized water for 9 days. The increase in the nanofiber mat crystallinity by the addition of GO was confirmed by the DSC data.

The fabricated fiber diameters were affected by the increased internal interactions within composite. Shell composition with GO resulted in the reduction of fiber diameter to  $174 \pm 31$  nm while the PVA-PEG-SiO<sub>2</sub> core composition produced the fiber with diameter of  $381 \pm 131$  nm. While the diameter of pristine PVA was  $386 \pm 81$  nm, the modification with silica has a mild effect on fiber diameter.

The melting temperature measurements confirmed the impact of GO addition on the fiber crystallinity. The increased melting temperature was caused by the restriction of the molecular movement due to the GO addition. The effect of silica was negligible compared with GO in terms of altering the physical properties, but the addition of silica affected the viscosity of the electrospinning solution and resulted in the reduction of the

fiber diameter from  $685 \pm 145$  nm of PVA-PEG composition to  $381 \pm 131$  nm of PVA-PEG-SiO<sub>2</sub>. Hence it was demonstrated that fiber modification by nanomaterial addition allows excellent control over both fiber dimensions as well as their mechanical and physical properties.

Pharmacokinetic analysis of core-shell fibers presents the importance of silica incorporation in the core PVA-PEG-SiO<sub>2</sub> that provides higher drug loading capacity compared with PVA-PEG core.

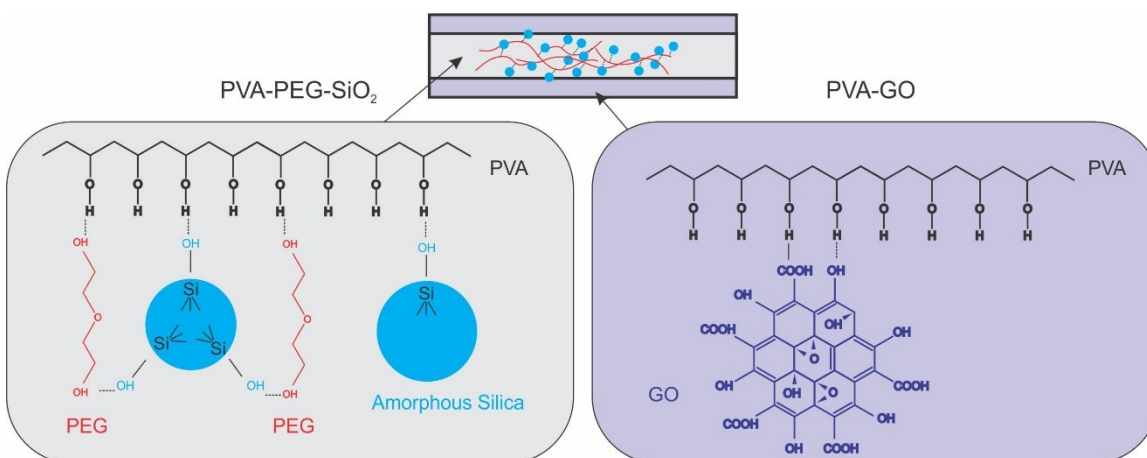


Figure 24. Interaction mechanisms within electrospun fibers.

Synthesized fiber mats were extensively studied within the scope of their application for drug loading and delivery. The antibacterial (CHX) was encapsulated within the core of fiber. The drug release behavior of fiber mats was found to depend on the drug dispersed, as well as the nanofiber morphology and diameter. The spinnable polymers used for nanofiber fabrication often have sufficient miscibility with hydrophilic or lipophilic drugs. Complex of characterization techniques (FTIR, Absorbance spectroscopy, ToF-SIMS) showed the presence of CHX placed within the core of core-shell fiber. Notably,

confocal microscopy were used to demonstrate efficient drug encapsulation solely within the core, without mixing with the shell material.

In the swelling-controlled drug delivery systems, the drug is dispersed in the hydrophilic polymer fiber. The fabricated PVA-based fibers create a semicrystalline polymer matrix. In an aqueous solution, molecules of water penetrate in the water-soluble matrix causing it to swell and undergo gelation with the relaxation of polymer chains. This transformation from semicrystalline polymer to hydrogel results in the drug release mechanism.

In this work, the drug release from the core-shell fiber composite showed the best correlation with the Higuchi and Korsmeyer – Peppas models. The exponential value ( $n$ ) found from Korsmeyer – Peppas model indicated non-Fickian transfer where the dissolution of fiber was found to be slower than the molecular diffusion from a medium into the matrix. It points out the importance of crosslinking modifications to control the drug release by fine tuning the fiber structure. The polymer-nanomaterials interactions allow obtaining prolonged drug release by the transformation mechanism from semicrystalline fiber mat to a hydrogel.

Along with the inner fiber modification, the coating with the hydrophobic polymer (PHB) was found to be capable of extending the diffusion time for the PVA-based material. Hydrophobic coating is an interesting approach that allows protecting the sample from water that results in prolonging the release process to 50 h (Supplementary Materials S17).

The choice of polymer and the nature of drugs dictate the physicochemical properties and drug-in-polymer interactions. A representative set of *in vitro* release

experiments was conducted for encapsulation of the fluorescence dyes, antibiotics and an antibacterial drug. The UV-Vis spectroscopy demonstrated the absorption properties of GO-based shell whereby the fluorescent dyes were completely removed after the fiber dissolution. In complex, this demonstrates the potential of medicated core-shell fiber composite for medical practice.

The medicated textile made from the water-swelling polymer composite will find application in the pharmaceutical context as a part of anti-cancer and antibacterial therapy, as well as for purifying photocatalysts to remove dyes. The results of pharmacokinetics studies open the pathway to the use of medicated fibers for therapeutical application. The findings of this study provide the platform for designing and building transdermal patches for the treatment of localized lesions [196].

In summary, the following principal outcomes were obtained.

- The fabrication route of fiber mat with medicated functions was developed. The detailed analysis of fiber morphology, physical properties of composite, and drug delivery was provided.
- The tensile strength was inversely correlated with the size of fibers, with the smaller fiber dimension being associated with higher tensile strength.
- Drug encapsulation of core-shell fibers were changed significantly for the modification of core composition with negligible amount of silica (0.005 wt. %), where the encapsulation efficiency of silica loading core-shell performed higher encapsulation efficiency  $1.02 \pm 0.27$  % against  $0.16 \pm 0.05$  % for PVA-PEG-SiO<sub>2</sub>@PVA-GO and PVA-PEG@PVA-GO, respectfully.

- Crosslinked with silica PVA-PEG-SiO<sub>2</sub>@PVA-GO core-shell fibers loaded with CHX performed non-Fickian model of drug diffusion as more a sustainable model of release. When the PVA-PEG @PVA-GO performed drug release kinetics based on the depletion of polymer matrix.
- The techniques as dip-coating with hydrophobic polymers and additive technologies supported by patterning proposed allow extending the drug release significantly beyond the initial burst release stage.

## Supplementary Materials

Table S1. The reference table of PVA-derived compositions of fibers

Polymer	Solvent	MW, kg/mol	Polymer Ratio, wt. %	Viscosity, Pa·s	Conductivity, $\mu\text{S/cm}$	Distance, cm	Voltage, kV	Flow rate, mL/h	d, nm	Ref.
<b>PVA</b>	H <sub>2</sub> O : EtOH (9:1)	146–186	8	0.01	470	15	13	0.3	469±77	[12]
<b>PVA</b>	H <sub>2</sub> O : EtOH (9:1)	146–186	8.5	0.06	442	15	13	1.3	489±78	[12]
<b>PVA</b>	H <sub>2</sub> O : EtOH (9:1)	89–98	16 w/v %	-	-	12	12	0.54	283±188	[197]
<b>Gelatin</b>	EtOH: PBS (1:1)		15 w/v %	-	-	12	12	1.8	229±94	[197]
<b>PVA: Gelatin</b>	H <sub>2</sub> O : EtOH (9:1)	89–98	1:1	-	-	12	15–19	0.42	256±99	[198]
<b>PVA: Gelatin</b>	H <sub>2</sub> O : EtOH (9:1)	89–98	1:3	-	-	15	15–20	0.18-0.54	182±81	[198]
<b>PVA: Chitosan</b>	H <sub>2</sub> O	80	10	0.25	2400	15	15	0.5	287	[190]
<b>PVA: cellulose (8:2)</b>	H <sub>2</sub> O	145	10	-	420	15	65–70		225	[199]

<b>PVA</b>	H <sub>2</sub> O	145	10	-	380	12	65–70		505	[199]
<b>PVA: Hydroxyapatite (1:2)</b>	H <sub>2</sub> O	205	10	-	-	10	18	0.47	508	[200]
<b>PVA: Hydroxyapatite (1:4)</b>	H <sub>2</sub> O	205	10	-	-	10	18	0.47	484	[200]
<b>PVA: Hydroxyapatite (1:9)</b>	H <sub>2</sub> O	205	10	-	-	10	18	0.47	514	[200]
<b>PVA- Collagen- Hydroxyapatite HA: PVA (1:2)</b>	H <sub>2</sub> O	205	10	-	-	10	18	0.47	552	[200]
<b>PANI/PVA</b>	H <sub>2</sub> O	1.799	14.3	-	-	16	23	0.36	117± 3	[201]
<b>PANI/PVA/RGO</b>	H <sub>2</sub> O	44	14.3	-	-	16	23	0.36	163± 4	[201]
<b>PVA</b>	DMSO: H <sub>2</sub> O	89–98	10	-	-	16	23	0.36	163± 5	[202]
<b>PVA-GO</b>	DMSO: H <sub>2</sub> O	89–98	10	-	-	16	23	0.36	163± 6	[202]
<b>PVA- dopamine- GO</b>	DMSO: H <sub>2</sub> O	89–98	10	-	-	16	23	0.36	163± 7	[202]

<b>rGO-coated PVA/dGO 5</b>	DMSO: H <sub>2</sub> O	89–98	10	-	-	16	23	0.36	163± 8	[202]
<b>PVA-PVP-PEG-Diatomite</b>	H <sub>2</sub> O	67	15	-	-	12	16.6	1	200- 400	[203]
<b>Chitosan/Polyethylene Oxide (PEO)</b>	Acetic Acid: H <sub>2</sub> O	2000	25	-	-	10	27	0.1	294± 64	[204]
<b>PVA-SiO<sub>2</sub></b>	H <sub>2</sub> O	125	5	-	-	12	30	1	100- 500	[205]
<b>PCL</b>	DCM: DMF (4:1)	80	12	1.36	537 ± 4	15	17	2	3160 ± 1050	[57]
<b>PVP + PVP-I 1:1 w/w</b>	EtOH	360	10	0.08	12100 ± 050			4		
<b>PEG</b>	DCM	35	25	1.61	290 ± 2			7		
<b>Coaxial PVA</b>	H <sub>2</sub> O: EtOH (9:1)	146– 186	8	0.01	470	15	13	0.3	469 ± 77	[72]
<b>Monoaxial PVA</b>	H <sub>2</sub> O: EtOH (9:1)	146– 186	8	0.06	442	15	13	0.4	489 ± 78	[72]
<b>PVA</b>	H <sub>2</sub> O (7:3)	-	15	-	-	14	15	0.8	500 ± 100	[36]
<b>PVA-Poly(acrylic acid) (PAA)</b>	H <sub>2</sub> O: EtOH (5:5)	196	5	-	-	13.5	8	-	341 ± 220	[77]

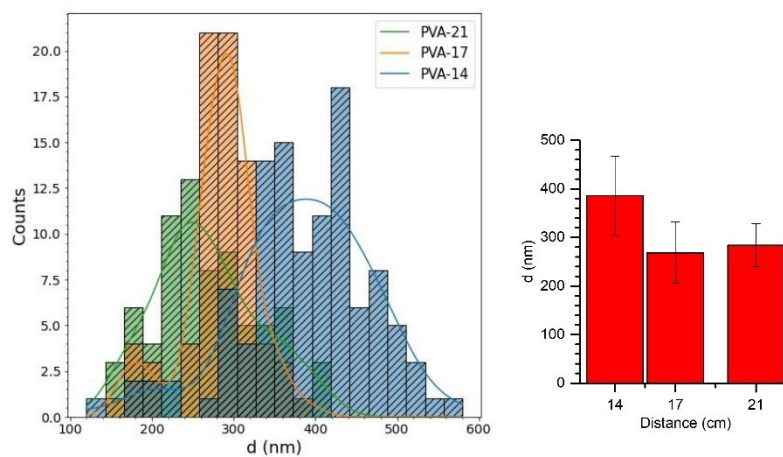


Figure S1. Dependence of the tip-to-target distance and mean diameter of PVA fibers

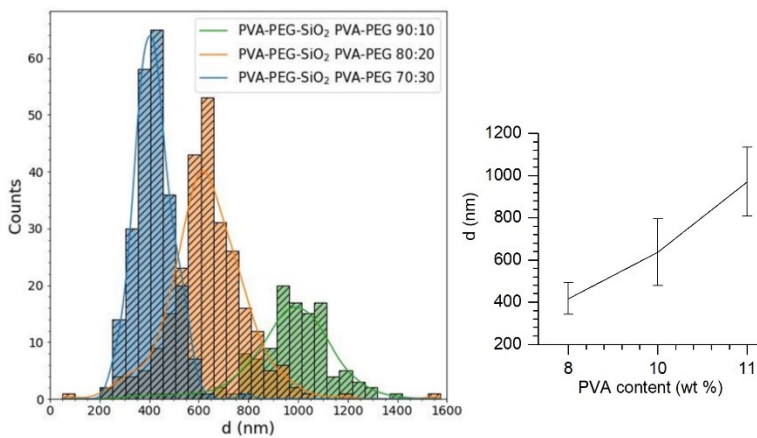


Figure S2. Dependence of PVA-PEG-SiO<sub>2</sub> core composition and mean diameter of fiber

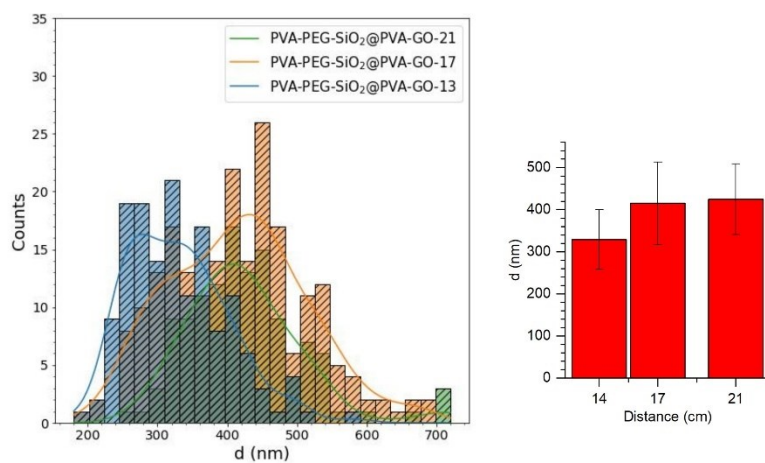


Figure S3. Dependence of tip-to-target distance and mean diameter of the PVA-PEG-SiO<sub>2</sub>@PVA-GO core-shell fiber

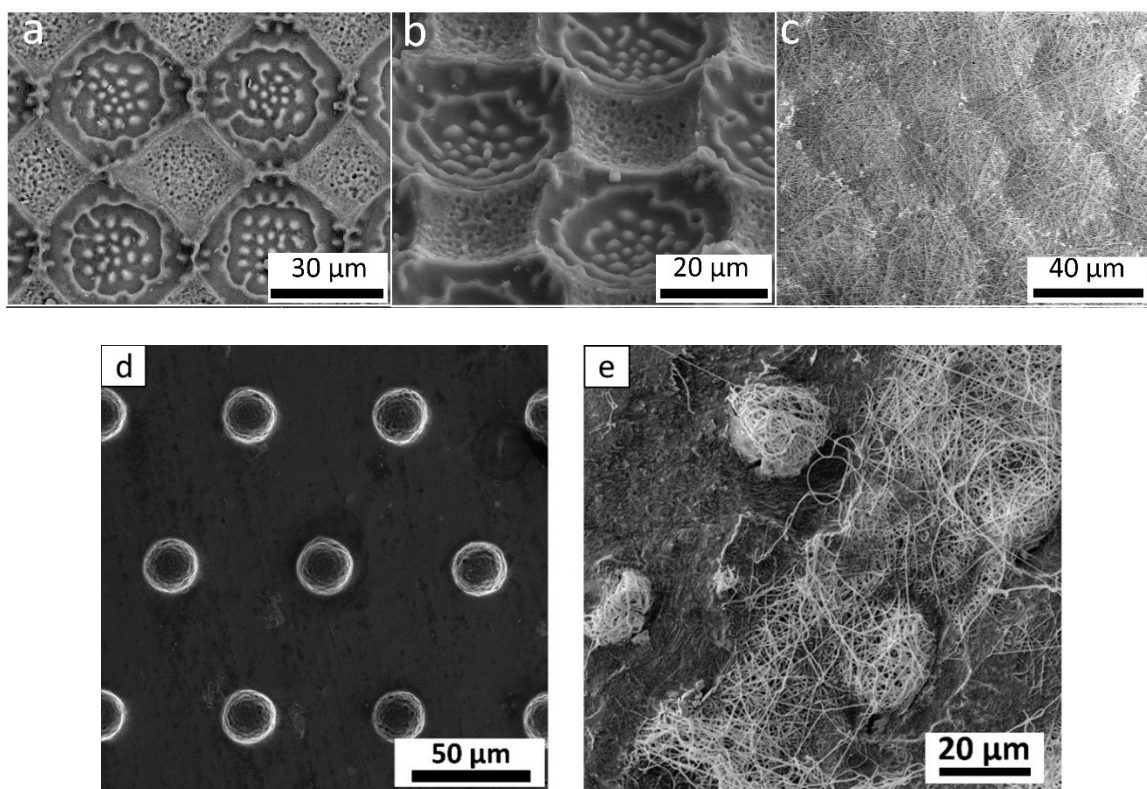


Figure S4. SEM imaging of patterned fiber mat core-shell fibers: (a), (b) etched pattern on Si wafer; (c) patterned fiber mat; (d) laser ablated aluminum plate; (e) patterned fiber basket mat

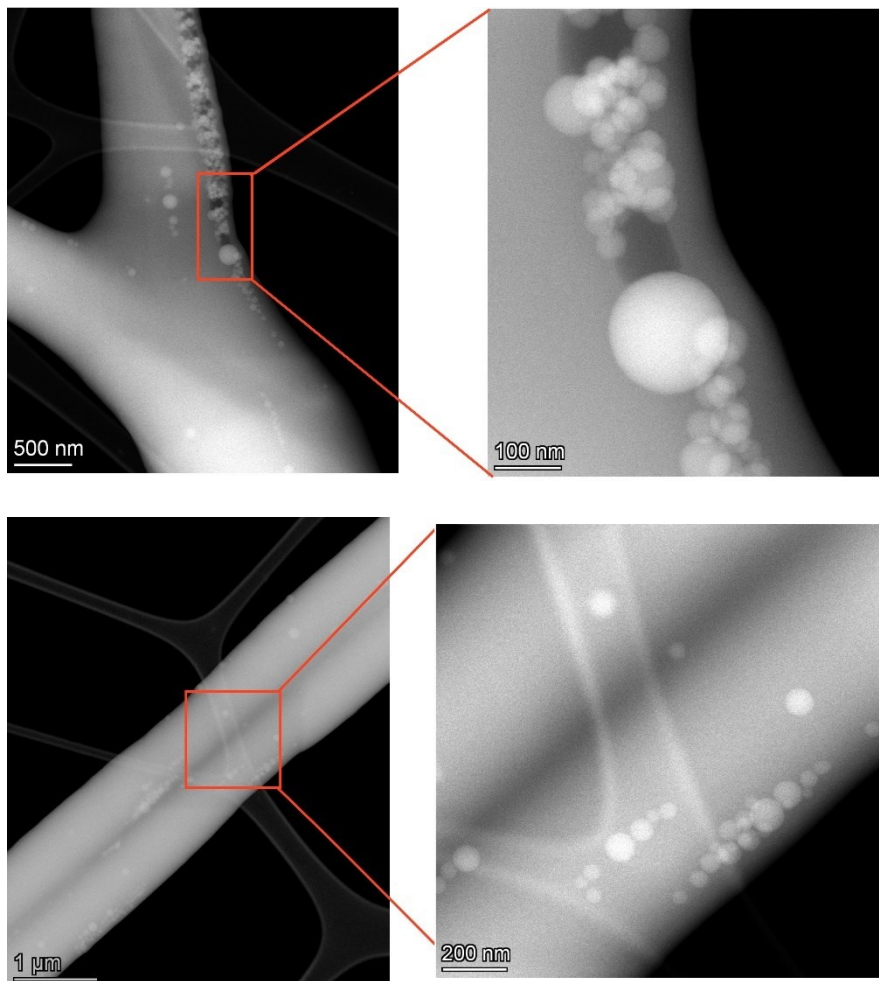


Figure S5. HAADF-STEM images of PVA-PEG-SiO<sub>2</sub> with PVA to PEG (90:10) ratios

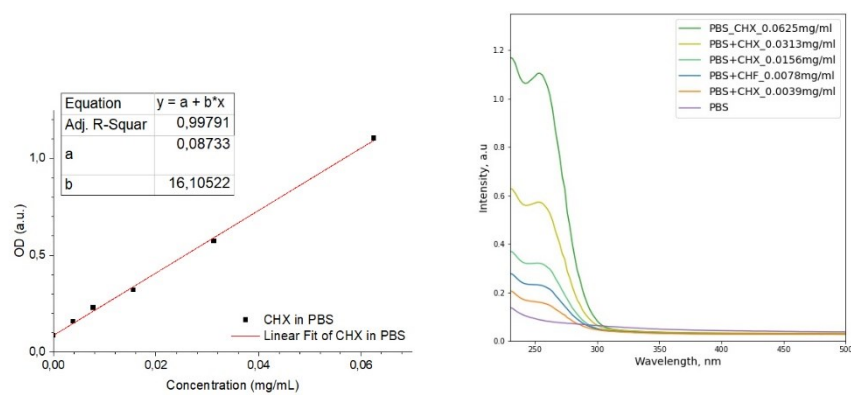


Figure S6. Calibration curve of CHX in the medium of 0.01 M PBS (pH 7.4)

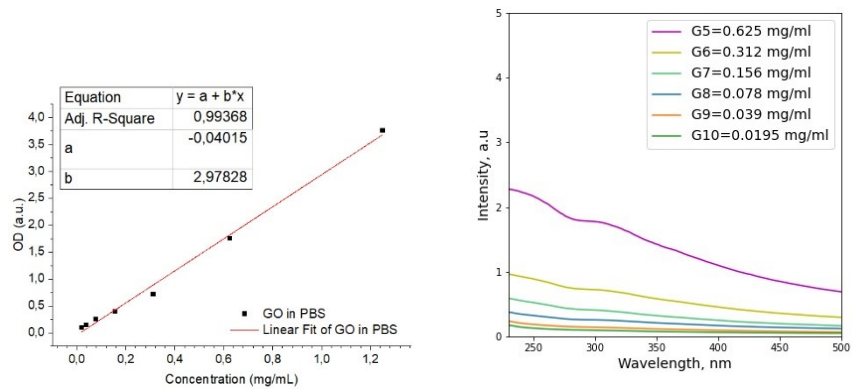


Figure S7. Calibration curve of GO in the medium of 0.01 M PBS (pH 7.4)

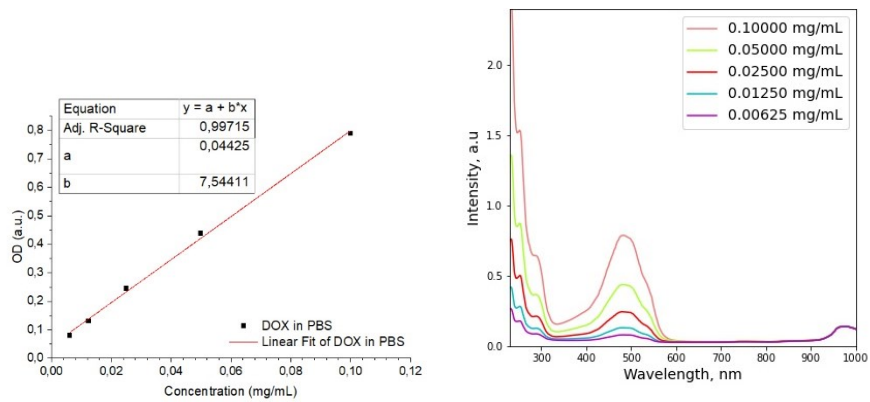


Figure S8. Calibration curve of DOX in the medium of 0.01 M PBS (pH 7.4)

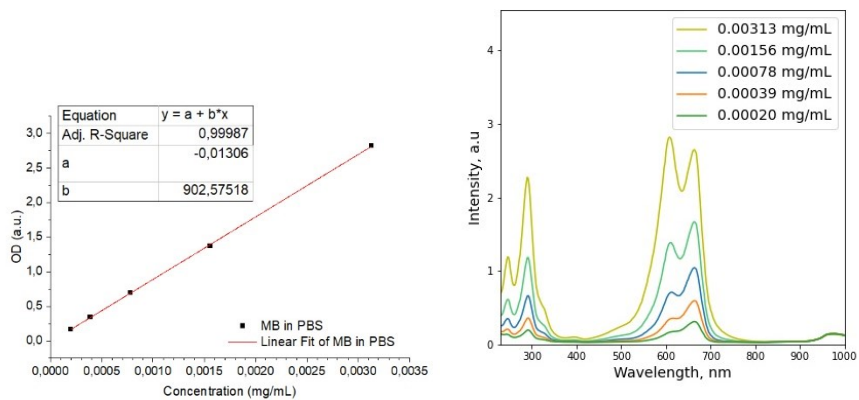


Figure S9. Calibration curve of MB in the medium of 0.01 M PBS (pH 7.4)

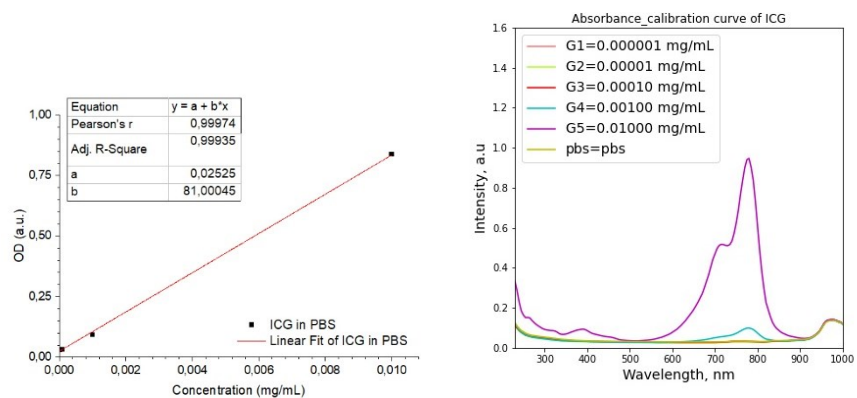


Figure S10. Calibration curve of ICG in the medium of 0.01 M PBS (pH 7.4)

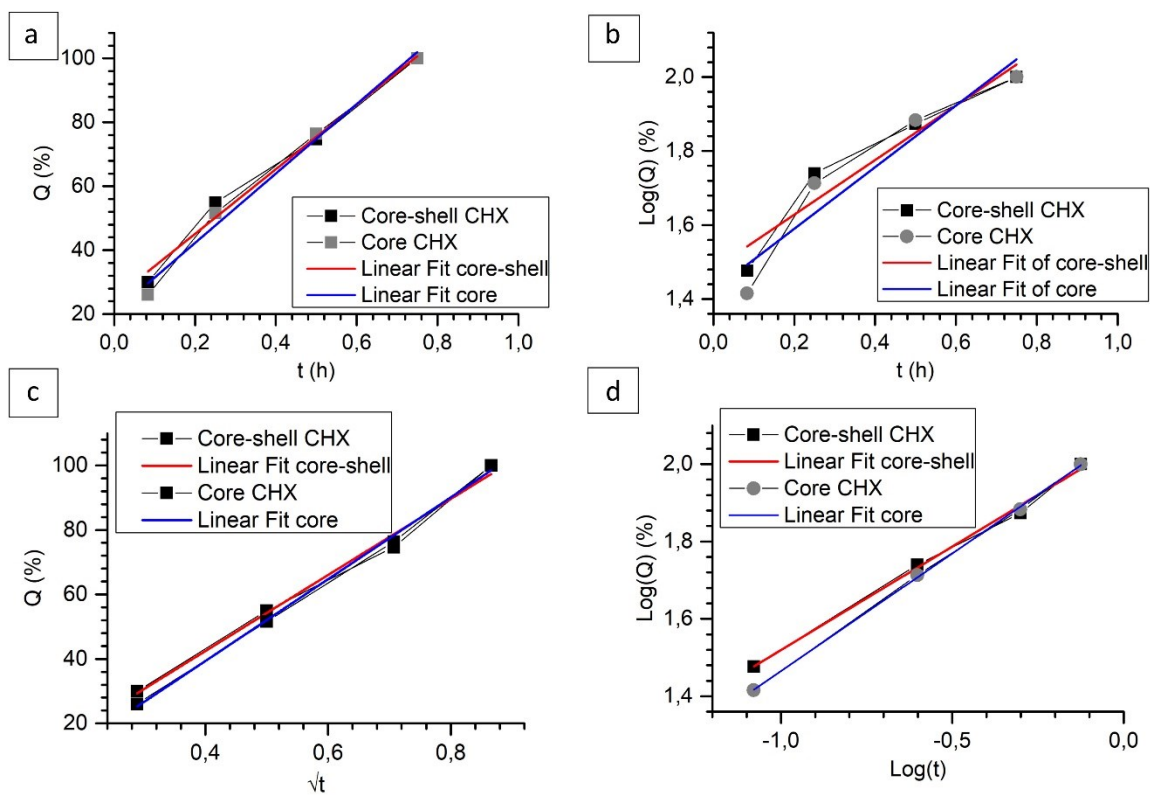


Figure S11. CHX release of PVA-PEG-SiO<sub>2</sub>-0.1x CHX core fiber and PVA-PEG-SiO<sub>2</sub>@PVA-GO-0.1x CHX core-shell fiber in the medium of 0.01 M PBS (pH 7.4): **(a)** Zero Order; **(b)** First Order; **(c)** Higuchi; **(d)** Korsmeyer – Peppas models

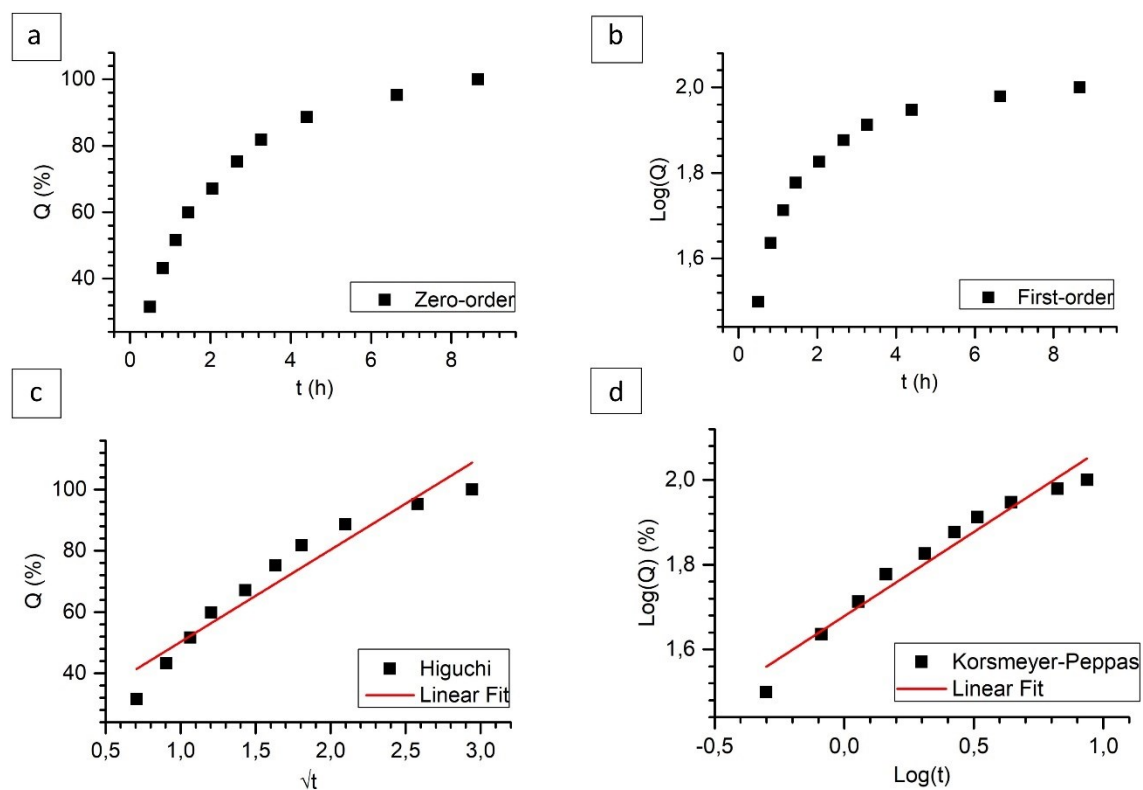


Figure S12. GO release of PVA-PEG-SiO<sub>2</sub>@PVA-GO core-shell fibers fitted to: **(a)** Zero Order; **(b)** First Order; **(c)** Higuchi model; **(d)** Korsmeyer – Peppas model

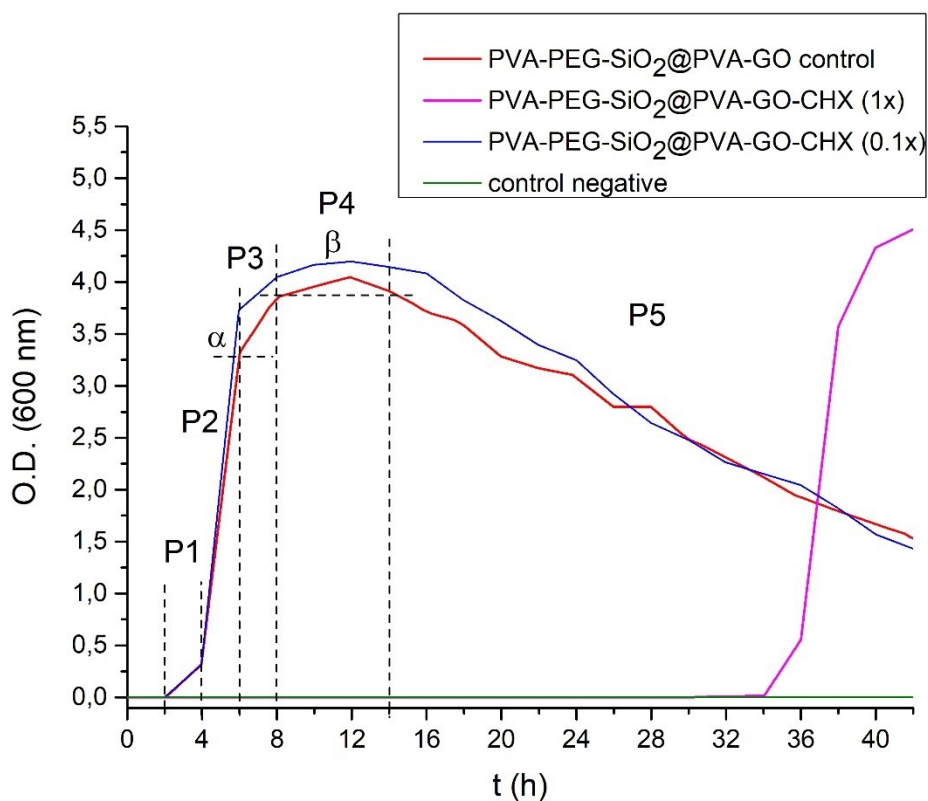


Figure S13 Antibacterial activity of CHX loaded core-shell PVA-PEG-SiO<sub>2</sub>@PVA-GO with concentration (0.1x, 1x)

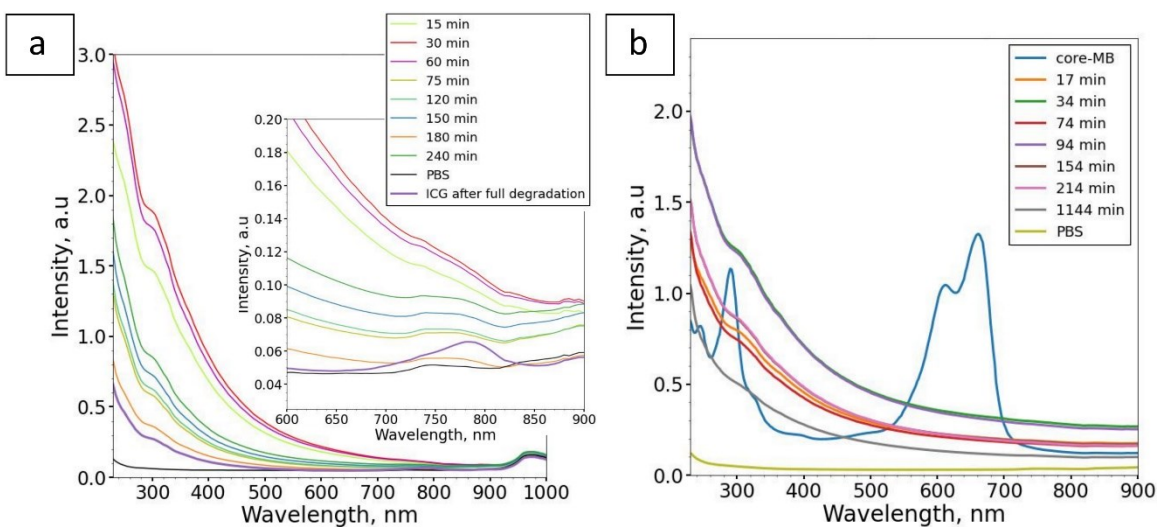


Figure S14. Absorbent property of GO observed in the core-shell fibers loaded with ICG (a); fluorescent label MB (b)

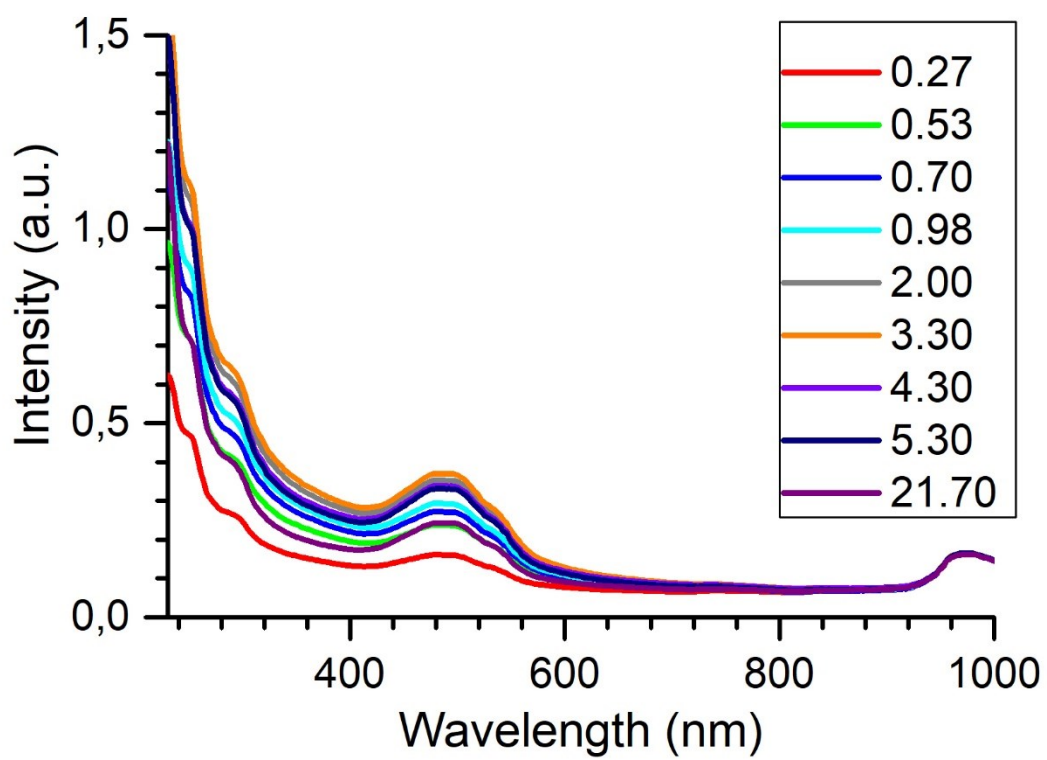


Figure S15. DOX release of core-shell DOX fiber mats during 22 h

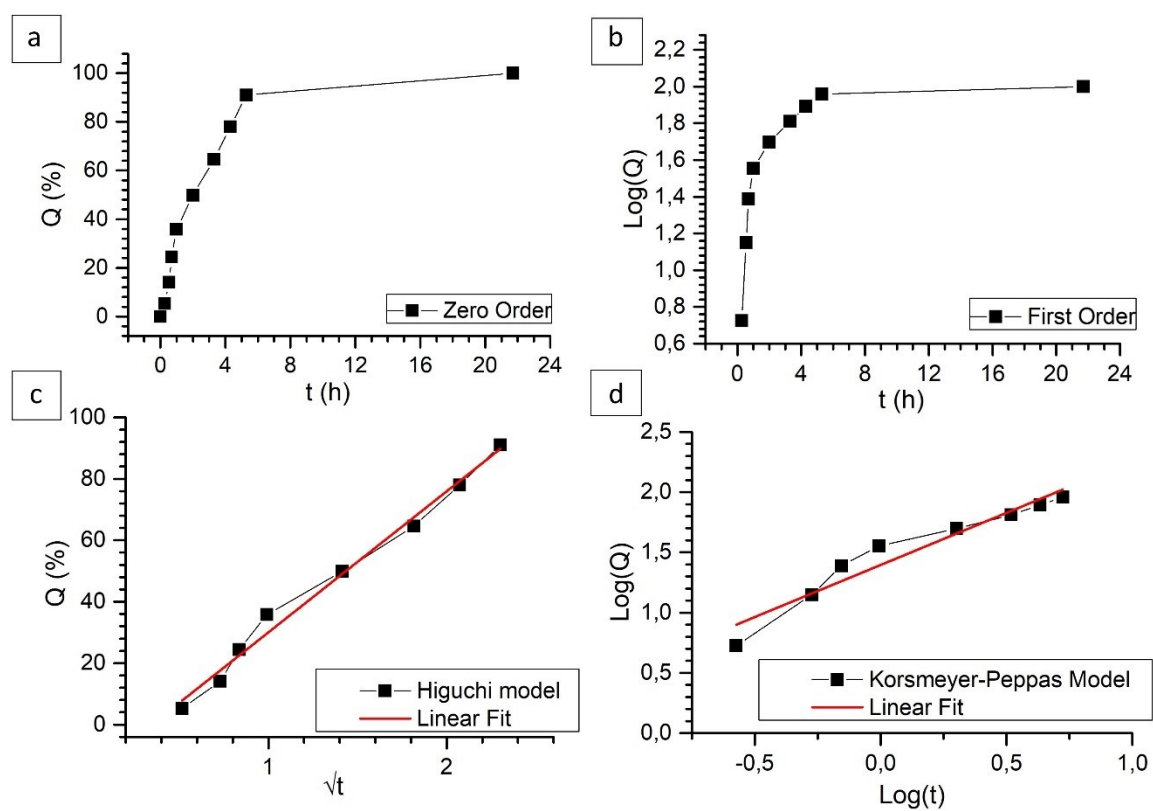


Figure S16. DOX release of core-shell fibers fitted to the models: **(a)** Zero Order; **(b)** First Order; **(c)** Higuchi model; **(d)** Korsmeier – Peppas model

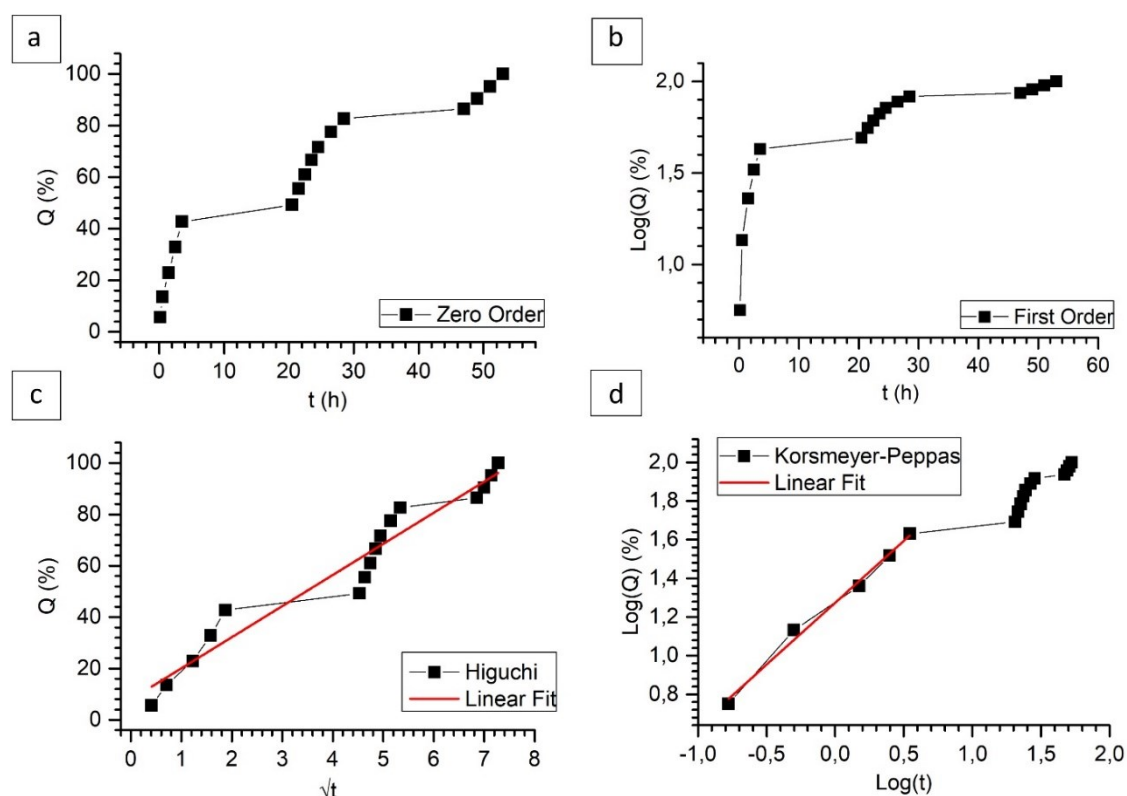


Figure S17. CHX release of dip-coated crosslinked core-shell fibers fitted to the models: **(a)** Zero Order; **(b)** First Order; **(c)** Higuchi model; **(d)** Korsmeier – Peppas model

Table S2 Release mechanisms of medicated nanofibers

		Zero Order	First Order	Higuchi	Korsmeier-Peppas	n	Diffusion Mechanism	Substance Released	Concentration, mg/mL
core CHX	R <sup>2</sup>	0,9830	0,8701	0,9966	0,9993	0,61	Non - Fickian	CHX	1
core-shell CHX	R <sup>2</sup>	0,9801	0,8844	0,9866	0,9938	0,54	Non - Fickian	CHX	1
crosslinked core-shell CHX-PHB (dip-coated sample)	R <sup>2</sup>	-	-	0,9407	0,9884	0,64	Non - Fickian	CHX	10
core-shell DOX	R <sup>2</sup>	-	-	0,9873	0,9215	0,86	Non - Fickian	DOX	16

core-shell	R <sup>2</sup>	-	-	0.9184	0.9484	0.40	Quasi-Fickian	GO	-
core-shell DOX	R <sup>2</sup>	-	-	0.9840	0.9218	0.81	Non - Fickian	GO	-
core-shell CHX	R <sup>2</sup>	-	-	0.9727	0.9844	0.47	Non - Fickian	GO	-

## Bibliography

1. Pisani, S.; Genta, I.; Modena, T.; Dorati, R.; Bruni, G.; Benazzo, M.; Conti, B. A Proof of Concept to Define the Parameters Affecting Poly-l-Lactide-Co-Poly- $\epsilon$ -Caprolactone Shape Memory Electrospun Nanofibers for Biomedical Applications. *Drug Delivery and Translational Research* **2022**, 1–15, doi:10.1007/S13346-022-01218
2. Rwei, S.P.; Huang, C.C. Electrospinning PVA Solution-Rheology and Morphology Analyses. *Fibers and Polymers* **2012**, *13*, 44–50, doi:10.1007/S12221-012-0044-9.
3. Wu, J.; Xie, L.; Lin, W.Z.Y.; Chen, Q. Biomimetic Nanofibrous Scaffolds for Neural Tissue Engineering and Drug Development. *Drug Discovery Today* **2017**, *22*, 1375–1384, doi:10.1016/j.drudis.2017.03.007.
4. Ye, K.; Kuang, H.; You, Z.; Morsi, Y.; Mo, X. Electrospun Nanofibers for Tissue Engineering with Drug Loading and Release. *Pharmaceutics* **2019**, *11*, doi:10.3390/pharmaceutics11040182.
5. Luraghi, A.; Peri, F.; Moroni, L. Electrospinning for Drug Delivery Applications: A Review. *Journal of Controlled Release* **2021**, *334*, 463–484, doi:10.1016/J.JCONREL.2021.03.033.
6. Sun, Y.; Cheng, S.; Lu, W.; Wang, Y.; Zhang, P.; Yao, Q. Electrospun Fibers and Their Application in Drug Controlled Release, Biological Dressings, Tissue Repair, and Enzyme Immobilization. *RSC Advances* **2019**, *9*, 25712–25729, doi:10.1039/C9RA05012D.

7. Adepu, S.; Ramakrishna, S. Controlled Drug Delivery Systems: Current Status and Future Directions. *Molecules* **2021**, *26*, doi:10.3390/MOLECULES26195905.
8. Abdullah, M.F.; Nuge, T.; Andriyana, A.; Ang, B.C.; Muhamad, F. Core-Shell Fibers: Design, Roles, and Controllable Release Strategies in Tissue Engineering and Drug Delivery. *Polymers (Basel)* **2019**, *11*, doi:10.3390/POLYM11122008.
9. Yu, D.G.; Li, J.J.; Williams, G.R.; Zhao, M. Electrospun Amorphous Solid Dispersions of Poorly Water-Soluble Drugs: A Review. *Journal of Controlled Release* **2018**, *292*, 91–110, doi:10.1016/J.JCONREL.2018.08.016.
10. Feng, X.; Li, J.; Zhang, X.; Liu, T.; Ding, J.; Chen, X. Electrospun Polymer Micro/Nanofibers as Pharmaceutical Repositories for Healthcare. *Journal of Controlled Release* **2019**, *302*, 19–41, doi:10.1016/J.JCONREL.2019.03.020.
11. Saraf, A.; Baggett, L.S.; Raphael, R.M.; Kasper, F.K.; Mikos, A.G. Regulated Non-Viral Gene Delivery from Coaxial Electrospun Fiber Mesh Scaffolds. *Journal of Controlled Release* **2010**, *143*, 95–103, doi:10.1016/J.JCONREL.2009.12.009.
12. Barani, H.; Khorashadizadeh, M.; Haseloer, A.; Klein, A. Characterization and Release Behavior of a Thiosemicarbazone from Electrospun Polyvinyl Alcohol Core-Shell Nanofibers. *Polymers (Basel)* **2020**, *12*, doi:10.3390/POLYM12071488.
13. Singh, B.; Kim, K.; Park, M.H. On-Demand Drug Delivery Systems Using Nanofibers. *Nanomaterials* **2021**, *11*, doi:10.3390/NANO11123411.
14. Lipsky, B.A.; Senneville, É.; Abbas, Z.G.; Aragón-Sánchez, J.; Diggie, M.; Embil, J.M.; Kono, S.; Lavery, L.A.; Malone, M.; van Asten, S.A.; et al. Guidelines on the

- Diagnosis and Treatment of Foot Infection in Persons with Diabetes (IWGDF 2019 Update). *Diabetes/Metabolism Research and Reviews* **2020**, *36*, e3280, doi:10.1002/DMRR.3280.
15. Nuutila, K.; Eriksson, E. Moist Wound Healing with Commonly Available Dressings. *Advances in Wound Care (New Rochelle)* **2021**, *10*, 685–698, doi:10.1089/wound.2020.1232.
16. Chen, H.; Cheng, R.; Zhao, X.; Zhang, Y.; Tam, A.; Yan, Y.; Shen, H.; Zhang, Y.S.; Qi, J.; Feng, Y.; et al. An Injectable Self-Healing Coordinative Hydrogel with Antibacterial and Angiogenic Properties for Diabetic Skin Wound Repair. *NPG Asia Materials* **2019**, *11*, 1–12, doi:10.1038/s41427-018-0103-9.
17. Chadwick, P.; McCardle, J. Open, Non-Comparative, Multi-Centre Post Clinical Study of the Performance and Safety of a Gelling Fibre Wound Dressing on Diabetic Foot Ulcers. *Journal of Wound Care* **2016**, *25*, 290–300, doi:10.12968/JOWC.2016.25.5.290.
18. Ahmed, A.S.; Mandal, U.K.; Taher, M.; Susanti, D.; Jaffri, J.M. PVA-PEG Physically Cross-Linked Hydrogel Film as a Wound Dressing: Experimental Design and Optimization. *Pharmaceutical Development and Technology* **2017**, *23*, 751–760, doi:10.1080/10837450.2017.1295067.
19. Hu, Y.; Yan, P.; Fu, L.; Zheng, Y.; Kong, W.; Wu, H.; Yu, X. Polyvinyl Alcohol/Polyvinyl Pyrrolidone Crosslinked Hydrogels Induce Wound Healing Through Cell Proliferation and Migration. *Journal of Biomaterials and Tissue Engineering* **2017**, *7*, 310–318, doi:10.1166/JBT.2017.1574.

20. Wen, S.; Hu, Y.; Zhang, Y.; Huang, S.; Zuo, Y.; Min, Y. Dual-Functional Core-Shell Electrospun Mats with Precisely Controlled Release of Anti-Inflammatory and Anti-Bacterial Agents. *Materials Science and Engineering: C* **2019**, *100*, 514–522, doi:10.1016/J.MSEC.2019.02.076.
21. Kataria, K.; Gupta, A.; Rath, G.; Mathur, R.B.; Dhakate, S.R. In Vivo Wound Healing Performance of Drug Loaded Electrospun Composite Nanofibers Transdermal Patch. *International Journal of Pharmaceutics* **2014**, *469*, 102–110, doi:10.1016/J.IJPHARM.2014.04.047.
22. Engineer, C.; Parikh, J.; Raval, A. Review on Hydrolytic Degradation Behavior of Biodegradable Polymers from Controlled Drug Delivery System. *Trends in Biomaterials and Artificial Organs* **2011**, *25*.
23. Vimalasruthi, N.; Vigneshkumar, G.; Esakkimuthu, S.; Sivakumar, K.; Stalin, T. Electrospun Nanofibers for Industrial and Energy Applications. *Electrospun Nanofibers* **2022**, 693–720, doi:10.1007/978-3-030-99958-2\_24.
24. Hassiba, A.J.; el Zowalaty, M.E.; Webster, T.J.; Abdullah, A.M.; Nasrallah, G.K.; Khalil, K.A.; Luyt, A.S.; Elzatahry, A.A. Synthesis, Characterization, and Antimicrobial Properties of Novel Double Layer Nanocomposite Electrospun Fibers for Wound Dressing Applications. *International Journal of Nanomedicine* **2017**, *12*, 2205–2213, doi:10.2147/IJN.S123417.
25. Flores-Arriaga, J.C.; Chavarría-Bolaños, D.; Pozos-Guillén, A. de J.; Escobar-Barrios, V.A.; Cerda-Cristerna, B.I. Synthesis of a PVA Drug Delivery System for Controlled Release of a Tramadol–Dexketoprofen Combination. *Journal of*

- Materials Science: Materials in Medicine* **2021**, *32*, 1–11, doi:10.1007/S10856-021-06529-3.
26. Guan, Y.; Li, W.; Zhang, Y.; Shi, Z.; Tan, J.; Wang, F.; Wang, Y. Aramid Nanofibers and Poly (Vinyl Alcohol) Nanocomposites for Ideal Combination of Strength and Toughness via Hydrogen Bonding Interactions. *Composite Science and Technology* **2017**, *144*, 193–201, doi:10.1016/J.COMPSCITECH.2017.03.010.
27. Kan, Y.; Salimon, A.I.; Korsunsky, A.M. On the Electrospinning of Nanostructured Collagen-PVA Fiber Mats. *Materials Today: Proceedings* **2020**, doi:10.1016/j.matpr.2020.07.621.
28. Rivera-Hernández, G.; Antunes-Ricardo, M.; Martínez-Morales, P.; Sánchez, M.L. Polyvinyl Alcohol Based-Drug Delivery Systems for Cancer Treatment. *International Journal of Pharmaceutics* **2021**, *600*, 120478, doi:10.1016/J.IJPHARM.2021.120478.
29. Ahmed, R.; Tariq, M.; Ali, I.; Asghar, R.; Noorunnisa Khanam, P.; Augustine, R.; Hasan, A. Novel Electrospun Chitosan/Polyvinyl Alcohol/Zinc Oxide Nanofibrous Mats with Antibacterial and Antioxidant Properties for Diabetic Wound Healing. *International Journal of Biological Macromolecules* **2018**, *120*, 385–393, doi:10.1016/j.ijbiomac.2018.08.057.
30. Fathi, A.; Khanmohammadi, M.; Goodarzi, A.; Foroutani, L.; Mobarakeh, Z.T.; Saremi, J.; Arabpour, Z.; Ai, J. Fabrication of Chitosan-Polyvinyl Alcohol and Silk Electrospun Fiber Seeded with Differentiated Keratinocyte for Skin Tissue

- Regeneration in Animal Wound Model. *Journal of Biological Engineering* **2020**, *14*, 27, doi:10.1186/s13036-020-00249-y.
31. Inozemtseva, O.A.; Salkovskiy, Y.E.; Severyukhina, A.N.; Vidyasheva, I. V.; Petrova, N. V; Metwally, H.A.; Stetciura, I.Y.; Gorin, D.A. Electrospinning of Functional Materials for Biomedicine and Tissue Engineering. *Russian Chemical Reviews* **2015**, *84*, 251–274, doi:10.1070/rcr4435.
32. Sun, J.; Wang, F.; Liu, L. Electrospinning Nanofiber onto Chitosan Nonwoven Fabric for Hemostasis and Disinfection Treatment. *2021 IEEE International Conference on Manipulation, Manufacturing and Measurement on the Nanoscale, 3M-NANO 2021 - Proceedings* **2021**, 421–425, doi:10.1109/3M-NANO49087.2021.9599762.
33. Alopaeus, J.F.; Hagesæther, E.; Tho, I. Micellisation Mechanism and Behaviour of Soluplus®–Furosemide Micelles: Preformulation Studies of an Oral Nanocarrier-Based System. *Pharmaceuticals (Basel)* **2019**, *12*, doi:10.3390/PH12010015.
34. Paaver, U.; Tamm, I.; Laidmäe, I.; Lust, A.; Kirsimäe, K.; Veski, P.; Kogermann, K.; Heinämäki, J. Soluplus Graft Copolymer: Potential Novel Carrier Polymer in Electrospinning of Nanofibrous Drug Delivery Systems for Wound Therapy. *Biomed Research International* **2014**, *2014*, doi:10.1155/2014/789765.
35. Hossen, S.; Hossain, M.K.; Basher, M.K.; Mia, M.N.H.; Rahman, M.T.; Uddin, M.J. Smart Nanocarrier-Based Drug Delivery Systems for Cancer Therapy and Toxicity Studies: A Review. *Journal of Advanced Research* **2019**, *15*, 1–18, doi:10.1016/j.jare.2018.06.005.

36. Józó, M.; Simon, N.; Yi, L.; Móczó, J.; Pukánszky, B. Improved Release of a Drug with Poor Water Solubility by Using Electrospun Water-Soluble Polymers as Carriers. *Pharmaceutics* **2021**, *2022*, *34*, doi:10.3390/pharmaceutics.
37. Gerardo Nava, J.L.; Rose, J.C.; Altinova, H.; Dalton, P.D.; de Laporte, L.; Brook, G.A. Nanofibers and Nanostructured Scaffolds for Nervous System Lesions. *Neuromethods* **2021**, *157*, 61–101, doi:10.1007/978-1-0716-0838-8\_3.
38. Matschegewski, C.; Kohse, S.; Markhoff, J.; Teske, M.; Wulf, K.; Grabow, N.; Schmitz, K.P.; Illner, S. Accelerated Endothelialization of Nanofibrous Scaffolds for Biomimetic Cardiovascular Implants. *Materials* **2022**, *15*, doi:10.3390/MA15062014.
39. Agarwal, A.; Rao, G.K.; Majumder, S.; Shandilya, M.; Rawat, V.; Purwar, R.; Verma, M.; Srivastava, C.M. Natural Protein-Based Electrospun Nanofibers for Advanced Healthcare Applications: Progress and Challenges. *3 Biotech* **2022**, *12*, 1–27, doi:10.1007/S13205-022-03152-Z.
40. Sell, S.A.; McClure, M.J.; Garg, K.; Wolfe, P.S.; Bowlin, G.L. Electrospinning of Collagen/Biopolymers for Regenerative Medicine and Cardiovascular Tissue Engineering. *Advanced Drug Delivery Reviews* **2009**, *61*, 1007–1019, doi:10.1016/J.ADDR.2009.07.012.
41. Sell, S.A.; Wolfe, P.S.; Garg, K.; McCool, J.M.; Rodriguez, I.A.; Bowlin, G.L. The Use of Natural Polymers in Tissue Engineering: A Focus on Electrospun Extracellular Matrix Analogues. *Polymers (Basel)* **2010**, *2*, 522–553, doi:10.3390/POLYM2040522.

42. Tsai, R.Y.; Hung, S.C.; Lai, J.Y.; Wang, D.M.; Hsieh, H.J. Electrospun Chitosan–Gelatin–Polyvinyl Alcohol Hybrid Nanofibrous Mats: Production and Characterization. *Journal of the Taiwan Institute of Chemical Engineers* **2014**, *45*, 1975–1981, doi:10.1016/J.JTICE.2013.11.003.
43. Celebioglu, A.; Saporito, A.F.; Uyar, T. Green Electrospinning of Chitosan/Pectin Nanofibrous Films by the Incorporation of Cyclodextrin/Curcumin Inclusion Complexes: PH-Responsive Release and Hydrogel Features. *ACS Sustainable Chemistry and Engineering* **2022**, *10*, 4758–4769, doi:10.1021/ACSSUSCHEMENG.2C00650.
44. Kan, Y.; Salimon, A.I.; Korsunsky, A.M. On the Electrospinning of Nanostructured Collagen-PVA Fiber Mats. *Materials Today: Proceedings* **2020**, doi:10.1016/j.matpr.2020.07.621.
45. Paaver, U.; Tamm, I.; Laidmäe, I.; Lust, A.; Kirsimäe, K.; Veski, P.; Kogermann, K.; Heinämäki, J. Soluplus Graft Copolymer: Potential Novel Carrier Polymer in Electrospinning of Nanofibrous Drug Delivery Systems for Wound Therapy. *Biomed Research International* **2014**, *2014*, doi:10.1155/2014/789765.
46. Pisani, S.; Friuli, V.; Conti, B.; Bruni, G.; Maggi, L. Tableted Hydrophilic Electrospun Nanofibers to Promote Meloxicam Dissolution Rate. *Journal of Drug Delivery Science and Technology* **2021**, *66*, doi:10.1016/J.JDDST.2021.102878.
47. Friuli, V.; Pisani, S.; Conti, B.; Bruni, G.; Maggi, L. Tablet Formulations of Polymeric Electrospun Fibers for the Controlled Release of Drugs with PH-

- Dependent Solubility. *Polymers (Basel)* **2022**, *14*, 2127, doi:10.3390/polym14102127.
48. Tawfik, E.A.; Alshamsan, A.; Abul Kalam, M.; Raish, M.; Alkholief, M.; Stapleton, P.; Harvey, K.; Craig, D.Q.M.; Barker, S.A. In Vitro and in Vivo Biological Assessment of Dual Drug-Loaded Coaxial Nanofibers for the Treatment of Corneal Abrasion. *International Journal of Pharmaceutics* **2021**, *604*, doi:10.1016/J.IJPHARM.2021.120732.
49. Mirzaeei, S.; Taghe, S.; Asare-Addo, K.; Nokhodchi, A. Polyvinyl Alcohol/Chitosan Single-Layered and Polyvinyl Alcohol/Chitosan/Eudragit RL100 Multi-Layered Electrospun Nanofibers as an Ocular Matrix for the Controlled Release of Ofloxacin: An In Vitro and In Vivo Evaluation. *AAPS PharmSciTech* **2021**, *22*, doi:10.1208/S12249-021-02051-5.
50. Marin, E.; Yoshikawa, O.; Boschetto, F.; Honma, T.; Adachi, T.; Zhu, W.; Xu, H.; Kanamura, N.; Yamamoto, T.; Pezzotti, G. Innovative Electrospun PCL/Fibroin/l-Dopa Scaffolds Supporting Bone Tissue Regeneration. *Biomedical Materials* **2022**, *17*, 045010, doi:10.1088/1748-605X/AC6C68.
51. Dikici, B.A.; Dikici, S.; Reilly, G.C.; MacNeil, S.; Claeysens, F. A Novel Bilayer Polycaprolactone Membrane for Guided Bone Regeneration: Combining Electrospinning and Emulsion Templating. *Materials (Basel)* **2019**, *12*, doi:10.3390/MA12162643.
52. Kwon, G.W.; Gupta, K.C.; Jung, K.H.; Kang, I.K. Lamination of Microfibrous PLGA Fabric by Electrospinning a Layer of Collagen-Hydroxyapatite Composite

- Nanofibers for Bone Tissue Engineering. *Biomaterials Research* **2017**, *21*, doi:10.1186/S40824-017-0097-3.
53. Yadav, M.; Paritosh, K.; Pareek, N.; Vivekanand, V. Composites Based on Bioderived Polymers: Potential Role in Tissue Engineering: Vol VI: Resorbable Polymer Fibers. *Materials for Biomedical Engineering* **2019**, *Vol. VI*, doi: doi.org/10.1016/B978-0-12-816901-8.00009-2.
54. Kitsara, M.; Joanne, P.; Boitard, S.E.; ben Dhiab, I.; Poinard, B.; Menasché, P.; Gagnieu, C.; Forest, P.; Agbulut, O.; Chen, Y. Fabrication of Cardiac Patch by Using Electrospun Collagen Fibers. *Microelectronic Engineering* **2015**, *144*, 46–50, doi:10.1016/j.mee.2015.02.034.
55. Ramos, D.M.; Abdulmalik, S.; Arul, M.R.; Sardashti, N.; Banasavadi-Siddegowda, Y.K.; Nukavarapu, S.P.; Drissi, H.; Kumbar, S.G. Insulin-Functionalized Bioactive Fiber Matrices with Bone Marrow-Derived Stem Cells in Rat Achilles Tendon Regeneration. *ACS Applied Bio Materials* **2022**, doi:10.1021/acsabm.2c00243.
56. Li, W.; Wu, P.; Zhang, Y.; Midgley, A.C.; Yuan, X.; Wu, Y.; Wang, L.; Wang, Z.; Zhu, M.; Kong, D. Bilayered Polymeric Micro- and Nanofiber Vascular Grafts as Abdominal Aorta Replacements: Long-Term in Vivo Studies in a Rat Model. *ACS Applied Bio Materials* **2019**, *2*, 4493–4502, doi:10.1021/ACSABM.9B00641.
57. Brako, F.; Luo, C.; Matharu, R.K.; Ciric, L.; Harker, A.; Edirisinghe, M.; Craig, D.Q.M. A Portable Device for the Generation of Drug-Loaded Three-Compartmental Fibers Containing Metronidazole and Iodine for Topical Application. *Pharmaceutics* **2020**, *12*, doi:10.3390/PHARMACEUTICS12040373.

58. Huo, P.; Han, X.; Zhang, W.; Zhang, J.; Kumar, P.; Liu, B. Electrospun Nanofibers of Polycaprolactone/Collagen as a Sustained-Release Drug Delivery System for Artemisinin. *Pharmaceutics* **2021**, *Vol. 13*, Page 1228, 13, 1228, doi:10.3390/PHARMACEUTICS13081228.
59. Ramos, D.M.; Abdulmalik, S.; Arul, M.R.; Rudraiah, S.; Laurencin, C.T.; Mazzocca, A.D.; Kumbar, S.G. Insulin Immobilized PCL-Cellulose Acetate Micro-Nanostructured Fibrous Scaffolds for Tendon Tissue Engineering. *Polymers for Advanced Technologies* **2019**, *30*, 1205–1215, doi:10.1002/PAT.4553.
60. Baker, B.M.; Chen, C.S. Deconstructing the Third Dimension: How 3D Culture Microenvironments Alter Cellular Cues. *Journal of Cell Science* **2012**, *125*, 3015–3024, doi:10.1242/JCS.079509.
61. Obata, A.; Hotta, T.; Wakita, T.; Ota, Y.; Kasuga, T. Electrospun Microfiber Meshes of Silicon-Doped Vaterite/Poly(Lactic Acid) Hybrid for Guided Bone Regeneration. *Acta Biomaterials* **2010**, *6*, 1248–1257, doi:10.1016/J.ACTBIO.2009.11.013.
62. Liao, S.; Nguyen, L.T.H.; Ngiam, M.; Wang, C.; Cheng, Z.; Chan, C.K.; Ramakrishna, S. Biomimetic Nanocomposites to Control Osteogenic Differentiation of Human Mesenchymal Stem Cells. *Advanced Healthcare Materials* **2014**, *3*, 737–751, doi:10.1002/ADHM.201300207.
63. Du, Y.; Guo, J.L.; Wang, J.; Mikos, A.G.; Zhang, S. Hierarchically Designed Bone Scaffolds: From Internal Cues to External Stimuli. *Biomaterials* **2019**, *218*, doi:10.1016/J.BIOMATERIALS.2019.119334.

64. Jenkins, T.L.; Little, D. Synthetic Scaffolds for Musculoskeletal Tissue Engineering: Cellular Responses to Fiber Parameters. *npj Regenerative Medicine* **2019**, *4*, 1–14, doi:10.1038/s41536-019-0076-5.
65. Sharma, P.; Ng, C.; Jana, A.; Padhi, A.; Szymanski, P.; Lee, J.S.H.; Behkam, B.; Nain, A.S. Aligned Fibers Direct Collective Cell Migration to Engineer Closing and Nonclosing Wound Gaps. *Molecular Biology of the Cell* **2017**, *28*, 2579–2588, doi:10.1091/MBC.E17-05-0305.
66. Sheets, K.; Wang, J.; Meehan, S.; Sharma, P.; Ng, C.; Khan, M.; Koons, B.; Behkam, B.; Nain, A.S. Cell-Fiber Interactions on Aligned and Suspended Nanofiber Scaffolds. *Journal of Biomimetics Biomaterials and Tissue Engineering* **2013**, *3*, 355–368, doi:10.1166/JBT.2013.1105.
67. Li, H.; Chen, X.; Lu, W.; Wang, J.; Xu, Y.; Guo, Y. Application of Electrospinning in Antibacterial Field. *Nanomaterials* **2021**, *Vol. 11*, Page 1822 **2021**, *11*, 1822, doi:10.3390/NANO11071822.
68. Haider, A.; Haider, S.; Kang, I.-K. A Comprehensive Review Summarizing the Effect of Electrospinning Parameters and Potential Applications of Nanofibers in Biomedical and Biotechnology. *Arabian Journal of Chemistry* **2018**, *11*, 1165–1188, doi:10.1016/j.arabjc.2015.11.015.
69. Liu, P.; Chen, W.; Liu, C.; Tian, M.; Liu, P. A Novel Poly (Vinyl Alcohol)/Poly (Ethylene Glycol) Scaffold for Tissue Engineering with a Unique Bimodal Open-Celled Structure Fabricated Using Supercritical Fluid Foaming. *Scientific Reports* **2019**, *9*, 1–12, doi:10.1038/s41598-019-46061-7.

70. Song, W.; Yu, X.; Markel, D.C.; Shi, T.; Ren, W. Coaxial PCL/PVA Electrospun Nanofibers: Osseointegration Enhancer and Controlled Drug Release Device. *Biofabrication* **2013**, *5*, doi:10.1088/1758-5082/5/3/035006.
71. Asran, A.S.; Razghandi, K.; Aggarwal, N.; Michler, G.H.; Groth, T. Nanofibers from Blends of Polyvinyl Alcohol and Polyhydroxy Butyrate as Potential Scaffold Material for Tissue Engineering of Skin. *Biomacromolecules* **2010**, *11*, 3413–3421, doi:10.1021/bm100912v.
72. Barani, H.; Khorashadizadeh, M.; Haseloer, A.; Klein, A. Characterization and Release Behavior of a Thiosemicarbazone from Electrospun Polyvinyl Alcohol Core-Shell Nanofibers. *Polymers (Basel)* **2020**, *12*, doi:10.3390/POLYM12071488.
73. Bardoňová, L.; Kutláková, K.M.; Kotzianová, A.; Kulhánek, J.; Židek, O.; Velebný, V.; Tokarský, J. Electrospinning of Fibrous Layers Containing an Antibacterial Chlorhexidine/Kaolinite Composite. *ACS Applied Bio Materials* **2020**, *3*, 3028–3038, doi:10.1021/ACSABM.0C00088.
74. Massarelli, E.; Silva, D.; Pimenta, A.F.R.; Fernandes, A.I.; Mata, J.L.G.; Armês, H.; Salema-Oom, M.; Saramago, B.; Serro, A.P. Polyvinyl Alcohol/Chitosan Wound Dressings Loaded with Antiseptics. *International Journal of Pharmaceutics* **2021**, *593*, 120110, doi:10.1016/J.IJPHARM.2020.120110.
75. Pilloni, A.; Ceccarelli, S.; Bosco, D.; Gerini, G.; Marchese, C.; Marini, L.; Rojas, M.A. Effect of Chlorhexidine Digluconate in Early Wound Healing of Human

- Gingival Tissues. A Histological, Immunohistochemical and Biomolecular Analysis. *Antibiotics* **2021**, *10*, doi:10.3390/ANTIBIOTICS10101192.
76. Abdel-Sayed, P.; Tornay, D.; Hirt-Burri, N.; de Buys Roessingh, A.; Raffoul, W.; Applegate, L.A. Implications of Chlorhexidine Use in Burn Units for Wound Healing. *Burns* **2020**, *46*, doi:10.1016/j.burns.2019.12.008.
77. Chee, B.S.; de Lima, G.G.; de Lima, T.A.M.; Seba, V.; Lemarquis, C.; Pereira, B.L.; Bandeira, M.; Cao, Z.; Nugent, M. Effect of Thermal Annealing on a Bilayer Polyvinyl Alcohol/Polyacrylic Acid Electrospun Hydrogel Nanofibres Loaded with Doxorubicin and Clarithromycin for a Synergism Effect against Osteosarcoma Cells. *Materials Today Chemistry* **2021**, *22*, doi:10.1016/J.MTCHEM.2021.100549.
78. Ma, Y.; Li, D.; Xiao, Y.; Ouyang, Z.; Shen, M.; Shi, X. LDH-Doped Electrospun Short Fibers Enable Dual Drug Loading and Multistage Release for Chemotherapy of Drug-Resistant Cancer Cells. *New Journal of Chemistry* **2021**, *45*, doi:10.1039/d1nj02159a.
79. Moydeen, A.M.; Padusha, M.S.A.; Thamer, B.M.; Ahamed N, A.; Al-Enizi, A.M.; El-Hamshary, H.; El-Newehy, M.H. Single-Nozzle Core-Shell Electrospun Nanofibers of PVP/Dextran as Drug Delivery System. *Fibers and Polymers* **2019**, *20*, 2078–2089, doi:10.1007/S12221-019-9187-2.
80. Morimune, S.; Kotera, M.; Nishino, T.; Goto, K.; Hata, K. Poly(Vinyl Alcohol) Nanocomposites with Nanodiamond. *Macromolecules* **2011**, *44*, 4415–4421, doi:10.1021/ma200176r.

81. Jia, R.J.; Teng, K.Y.; Huang, J.Y.; Wei, X.; Qin, Z.Y. Hydrogen Bonding Crosslinking of Starch-Polyvinyl Alcohol Films Reinforced by Ultrasound-Assisted and Cellulose Nanofibers Dispersed Cellulose Nanocrystals. *Starch-Stärke* **2022**, *74*, doi:10.1002/STAR.202100227.
82. Miraftab, M.; Saifullah, A.N.; Çay, A. Physical Stabilisation of Electrospun Poly(Vinyl Alcohol) Nanofibres: Comparative Study on Methanol and Heat-Based Crosslinking. *Journal of Materials Science* **2015**, *50*, 1943–1957, doi:10.1007/s10853-014-8759-1.
83. Sau, S.; Pandit, S.; Kundu, S. Crosslinked Poly (Vinyl Alcohol): Structural, Optical and Mechanical Properties. *Surfaces and Interfaces* **2021**, *25*, 101198, doi:10.1016/J.SURFIN.2021.101198.
84. Liu, T.; Jiao, C.; Peng, X.; Chen, Y.N.; Chen, Y.; He, C.; Liu, R.; Wang, H. Super-Strong and Tough Poly(Vinyl Alcohol)/Poly(Acrylic Acid) Hydrogels Reinforced by Hydrogen Bonding. *Journal of Materials Chemistry B* **2018**, *6*, 8105–8114, doi:10.1039/C8TB02556H.
85. Park, M.J.; Gonzales, R.R.; Abdel-Wahab, A.; Phuntsho, S.; Shon, H.K. Hydrophilic Polyvinyl Alcohol Coating on Hydrophobic Electrospun Nanofiber Membrane for High Performance Thin Film Composite Forward Osmosis Membrane. *Desalination* **2018**, *426*, 50–59, doi:10.1016/J.DESAL.2017.10.042.
86. Elessawy, N.A.; Gouda, M.H.; Elnouby, M.; Ali, S.M.; Salerno, M.; Youssef, M.E. Sustainable Microbial and Heavy Metal Reduction in Water Purification Systems

- Based on PVA/IC Nanofiber Membrane Doped with PANI/GO. *Polymers (Basel)* **2022**, *14*, doi:10.3390/POLYM14081558.
87. Chen, C.; Tang, Y.; Vlahovic, B.; Yan, F. Electrospun Polymer Nanofibers Decorated with Noble Metal Nanoparticles for Chemical Sensing. *Nanoscale Research Letters* **2017**, *12*, 1–15, doi:10.1186/S11671-017-2216-4.
88. Díez, B.; Homer, W.J.A.; Leslie, L.J.; Kyriakou, G.; Rosal, R.; Topham, P.D.; Theodosiou, E. Chemically Cross-Linked Poly(Vinyl Alcohol) Electrospun Fibrous Mats as Wound Dressing Materials. *Journal of Chemical Technology and Biotechnology* **2022**, *97*, 620–632, doi:10.1002/JCTB.7006.
89. Kajdič, S.; Planinšek, O.; Gašperlin, M.; Kocbek, P. Electrospun Nanofibers for Customized Drug-Delivery Systems. *Journal of Drug Delivery Science and Technology* **2019**, *51*, 672–681, doi:10.1016/J.JDDST.2019.03.038.
90. Jacques, C.H.M.; Hopfenberg, H.B.; Stannett, V. Super Case II Transport of Organic Vapors in Glassy Polymers. *Polymer Science and Technology* **1974**, 73–86, doi:10.1007/978-1-4684-2877-3\_6.
91. Talevi, A.; Ruiz, M.E. Korsmeyer-Peppas, Peppas-Sahlin, and Brazel-Peppas: Models of Drug Release. *The ADME Encyclopedia* **2021**, 1–9, doi:10.1007/978-3-030-51519-5\_35-1.
92. Talevi, A.; Ruiz, M.E. Drug Dissolution: Fundamental Theoretic Models. *The ADME Encyclopedia* **2022**, 341–349, doi:10.1007/978-3-030-84860-6\_29.
93. Pratap Singh, A.; Siddiqui, J.; Diosady, L.L. Characterizing the PH-Dependent Release Kinetics of Food-Grade Spray Drying Encapsulated Iron Microcapsules for

- Food Fortification. *Food and Bioprocess Technology* **2018**, *11*, 435–446, doi:10.1007/S11947-017-2022-0.
94. Elmas, A.; Akyüz, G.; Bergal, A.; Andaç, M.; Andaç, Ö. Mathematical Modelling of Drug Release. *Research on Engineering and Structures of Materials* **2020**, *6*, 327–350, doi:10.17515/resm2020.178na0122.
95. Padmaa Paarakh, M.; Ani Jose, P.; Setty, C.M.; Christoper, G.V.P. Release Kinetics – Concepts and Applications. *International Journal of Pharmacy Research & Technology* **2018**, *8*, 12–20, doi:10.31838/ijprt/08.01.02.
96. Dash, S.; Murthy, P.N.; Nath, L.; Chowdwhury, P. Kinetic Modeling on Drug Release from Controlled Drug Delivery Systems. *Acta Poloniae Pharmaceutica – Drug Research* **2010**, *67*, 217–223.
97. Aguzzi, C.; Cerezo, P.; Salcedo, I.; Sánchez, R.; Viseras, C. Mathematical Models Describing Drug Release from Biopolymeric Delivery Systems. *Materials Technology* **2010**, *25*, 205–211, doi:10.1179/175355510X12723642365566.
98. Adepu, S.; Ramakrishna, S. Controlled Drug Delivery Systems: Current Status and Future Directions. *Molecules* **2021**, *26*, doi:10.3390/MOLECULES26195905.
99. Windolf, H.; Chamberlain, R.; Quodbach, J. Predicting Drug Release from 3D Printed Oral Medicines Based on the Surface Area to Volume Ratio of Tablet Geometry. *Pharmaceutics* **2021**, *13*, 1453, doi:10.3390/PHARMACEUTICS13091453/S1.
100. Brannon-Peppas, L.; Peppas, N.A. Solute and Penetrant Diffusion in Swellable Polymers. IX. The Mechanisms of Drug Release from Ph-Sensitive Swelling-

- Controlled Systems. *Journal of Controlled Release* **1989**, *8*, 267–274, doi:10.1016/0168-3659(89)90048-5.
101. Ritger, P.L.; Peppas, N.A. A Simple Equation for Description of Solute Release II. Fickian and Anomalous Release from Swellable Devices. *Journal of Controlled Release* **1987**, *5*, 37–42, doi:10.1016/0168-3659(87)90035-6.
102. Samavedi, S.; Joy, N. Identifying Specific Combinations of Matrix Properties That Promote Controlled and Sustained Release of a Hydrophobic Drug from Electrospun Meshes. *ACS Omega* **2020**, *5*, 15865–15876, doi:10.1021/ACSOMEGA.0C00954.
103. Pisani, S.; Dorati, R.; Chiesa, E.; Genta, I.; Modena, T.; Bruni, G.; Grisoli, P.; Conti, B. Release Profile of Gentamicin Sulfate from Polylactide-Co-Polycaprolactone Electrospun Nanofiber Matrices. *Pharmaceutics* **2019**, *Vol. 11*, Page 161 **2019**, *11*, 161, doi:10.3390/PHARMACEUTICS11040161.
104. Wang, C.; Yan, K.W.; Lin, Y.D.; Hsieh, P.C.H. Biodegradable Core/Shell Fibers by Coaxial Electrospinning: Processing, Fiber Characterization, and Its Application in Sustained Drug Release. *Macromolecules* **2010**, *43*, 6389–6397, doi:10.1021/ma100423x.
105. Zhang, Q.; Li, Y.; Lin, Z.Y. (William); Wong, K.K.Y.; Lin, M.; Yildirimer, L.; Zhao, X. Electrospun Polymeric Micro/Nanofibrous Scaffolds for Long-Term Drug Release and Their Biomedical Applications. *Drug Discovery Today* **2017**, *22*, 1351–1366, doi:10.1016/J.DRUDIS.2017.05.007.

106. Ewaldz, E.; Brettmann, B. Molecular Interactions in Electrospinning: From Polymer Mixtures to Supramolecular Assemblies. *ACS Applied Polymer Materials* **2019**, *1*, 298–308, doi:10.1021/ACSAPM.8B00073.
107. Nishiyabu, R.; Tomura, M.; Okade, T.; Kubo, Y. Boronic Acids as Molecular Inks for Surface Functionalization of Polyvinyl Alcohol Substrates. *New Journal of Chemistry* **2018**, *42*, 7392–7398, doi:10.1039/C8NJ00992A.
108. Nishiyabu, R.; Takahashi, Y.; Yabuki, T.; Gommori, S.; Yamamoto, Y.; Kitagishi, H.; Kubo, Y. Boronate Sol-Gel Method for One-Step Fabrication of Polyvinyl Alcohol Hydrogel Coatings by Simple Cast- And Dip-Coating Techniques. *RSC Advanced* **2020**, *10*, 86–94, doi:10.1039/C9RA08208E.
109. Zhong, Q.; Shi, G.; Sun, Q.; Mu, P.; Li, J. Robust PVA-GO-TiO<sub>2</sub> Composite Membrane for Efficient Separation Oil-in-Water Emulsions with Stable High Flux. *Journal of Membrane Science* **2021**, *640*, doi:10.1016/J.MEMSCI.2021.119836.
110. Falqi, F.H.; Bin-Dahman, O.A.; Hussain, M.; Al-Harhi, M.A. Preparation of Miscible PVA/PEG Blends and Effect of Graphene Concentration on Thermal, Crystallization, Morphological, and Mechanical Properties of PVA/PEG (10wt%) Blend. *International Journal of Polymer Science* **2018**, *2018*, doi:10.1155/2018/8527693.
111. Liu, C.; Liu, H.; Xiong, T.; Xu, A.; Pan, B.; Tang, K. Graphene Oxide Reinforced Alginate/PVA Double Network Hydrogels for Efficient Dye Removal. *Polymers* **2018**, *Vol. 10, Page 835* **2018**, *10*, 835, doi:10.3390/POLYM10080835.

112. Zhou, X.; Ding, C.; Cheng, C.; Liu, S.; Duan, G.; Xu, W.; Liu, K.; Hou, H. Mechanical and Thermal Properties of Electrospun Polyimide/RGO Composite Nanofibers via in-Situ Polymerization and in-Situ Thermal Conversion. *European Polymer Journal* **2020**, *141*, 110083, doi:10.1016/J.EURPOLYMJ.2020.110083.
113. Qian, H.; Wang, J.; Yan, L.; Qian, H.; Wang, J.; Yan, L. Synthesis of Lignin-Poly(N-Methylaniline)-Reduced Graphene Oxide Hydrogel for Organic Dye and Lead Ions Removal. *Journal of Bioresources and Bioproducts* **2020**, *Vol. 5, Issue 3, Pages: 213-219*, 5, 213–219, doi:10.1016/J.JOBAB.2020.07.006.
114. Paulista Neto, A.J.; Fileti, E.E. Elucidating the Amphiphilic Character of Graphene Oxide. *Physical Chemistry Chemical Physics* **2018**, *20*, 9507–9515, doi:10.1039/C8CP00797G.
115. Chakravarty, M.; Vora, A. Nanotechnology-Based Antiviral Therapeutics. *Drug Delivery and Translational Research* **2020**, *11*, 748–787, doi:10.1007/S13346-020-00818-0.
116. Al-Dhahebi, A.M.; Gopinath, S.C.B.; Saheed, M.S.M. Graphene Impregnated Electrospun Nanofiber Sensing Materials: A Comprehensive Overview on Bridging Laboratory Set-up to Industry. *Nano Convergence* **2020**, *7*, 1–23, doi:10.1186/S40580-020-00237-4.
117. Lund, A.; van der Velden, N.M.; Persson, N.K.; Hamed, M.M.; Müller, C. Electrically Conducting Fibres for E-Textiles: An Open Playground for Conjugated Polymers and Carbon Nanomaterials. *Materials Science and Engineering: R: Reports* **2018**, *126*, 1–29, doi:10.1016/J.MSER.2018.03.001.

118. Mousavi, S.M.; Hashemi, S.A.; Kalashgrani, M.Y.; Omidifar, N.; Bahrani, S.; Rao, N.V.; Babapoor, A.; Gholami, A.; Chiang, W.-H. Bioactive Graphene Quantum Dots Based Polymer Composite for Biomedical Applications. *Polymers (Basel)* **2022**, *14*, 617, doi:10.3390/POLYM14030617.
119. Cao, H.; Qi, W.; Gao, X.; Wu, Q.; Tian, L.; Wu, W. Graphene Quantum Dots Prepared by Electron Beam Irradiation for Safe Fluorescence Imaging of Tumor. *Nanotheranostics* **2022**, *6*, 205–214, doi:10.7150/NTNO.67070.
120. Yu, H.; Yang, P.; Jia, Y.; Zhang, Y.; Ye, Q.; Zeng, S. Regulation of Biphasic Drug Release Behavior by Graphene Oxide in Polyvinyl Pyrrolidone/Poly( $\epsilon$ -Caprolactone) Core/Sheath Nanofiber Mats. *Colloids Surfaces B: Biointerfaces* **2016**, *146*, doi:10.1016/j.colsurfb.2016.05.052.
121. Lee, H.; Xu, G.; Kharaghani, D.; Nishino, M.; Song, K.H.; Lee, J.S.; Kim, I.S. Electrospun Tri-Layered Zein/PVP-GO/Zein Nanofiber Mats for Providing Biphasic Drug Release Profiles. *International Journal of Pharmaceutics* **2017**, *531*, 101–107, doi:10.1016/J.IJPHARM.2017.08.081.
122. Somesh, T.E.; Siddaramaiah; Demappa, T. Tailoring of Ternary Nanocomposite Films of Poly(Vinyl Alcohol)/AgAlO<sub>2</sub>@reduced Graphene Oxide: An Active Material for Flexible Supercapacitors. *Journal of Solid State Chemistry* **2022**, *309*, doi:10.1016/J.JSSC.2021.122824.
123. Wadhwa, H.; Kandhol, G.; Deshpande, U.P.; Mahendia, S.; Kumar, S. Thermal Stability and Dielectric Relaxation Behavior of in Situ Prepared Poly(Vinyl

- Alcohol) (PVA)-Reduced Graphene Oxide (RGO) Composites. *Colloid and Polymer Science* **2020**, *298*, 1319–1333, doi:10.1007/S00396-020-04718-0.
124. Huang, C.L.; Lee, K.M.; Liu, Z.X.; Lai, R.Y.; Chen, C.K.; Chen, W.C.; Hsu, J.F. Antimicrobial Activity of Electrospun Polyvinyl Alcohol Nanofibers Filled with Poly[2-(Tert-Butylaminoethyl) Methacrylate]-Grafted Graphene Oxide Nanosheets. *Polymers* **2020**, *Vol. 12*, *Page 1449*, *12*, 1449, doi:10.3390/POLYM12071449.
125. Ahlinder, L.; Henych, J.; Lindström, S.W.; Ekstrand-Hammarström, B.; Stengl, V.; Österlund, L. Graphene Oxide Nanoparticle Attachment and Its Toxicity on Living Lung Epithelial Cells. *RSC Advances* **2015**, *5*, 59447–59457, doi:10.1039/C5RA09351A.
126. Liao, K.H.; Lin, Y.S.; MacOsko, C.W.; Haynes, C.L. Cytotoxicity of Graphene Oxide and Graphene in Human Erythrocytes and Skin Fibroblasts. *ACS Applied Materials and Interfaces* **2011**, *3*, 2607–2615, doi:10.1021/AM200428V.
127. Ahmad, A.L.; Ebenezer, O.I.; Shoparwe, N.F.; Ismail, S. Graphene Oxide-Doped Polymer Inclusion Membrane for Remediation of Pharmaceutical Contaminant of Emerging Concerns: Ibuprofen. *Membranes (Basel)* **2022**, *12*, doi:10.3390/membranes12010024.
128. Pirzada, T.; Arvidson, S.A.; Saquing, C.D.; Shah, S.S.; Khan, S.A. Hybrid Silica-PVA Nanofibers via Sol-Gel Electrospinning. *Langmuir* **2012**, *28*, 5834–5844, doi:10.1021/la300049j.

129. Nur Izzah, M.F.; Ahmad, H.; Rahman, M.F.A.; Rahman, N.A. Electrospun Poly (Vinyl Alcohol) Nanofibers Doped with Mesoporous Silica Nanoparticles for Controlled Release of Hydrophilic Model Drug. *Malaysian Journal of Analytical Sciences* **2019**, *23*, 212–218, doi:10.17576/MJAS-2019-2302-05.
130. Song, B.; Wu, C.; Chang, J. Controllable Delivery of Hydrophilic and Hydrophobic Drugs from Electrospun Poly(Lactic- Co -Glycolic Acid)/Mesoporous Silica Nanoparticles Composite Mats. *Journal of Biomedical Materials Research B Applied Biomaterials* **2012**, *100B*, 2178–2186, doi:10.1002/jbm.b.32785.
131. Catauro, M.; Bollino, F.; Papale, F.; Gallicchio, M.; Pacifico, S. Influence of the Polymer Amount on Bioactivity and Biocompatibility of SiO<sub>2</sub>/PEG Hybrid Materials Synthesized by Sol–Gel Technique. *Materials Science and Engineering: C* **2015**, *48*, 548–555, doi:10.1016/j.msec.2014.12.035.
132. Evlashin, S.A.; Svyakhovskiy, S.E.; Fedorov, F.S.; Mankelevich, Y.A.; Dyakonov, P. v.; Minaev, N. v.; Dagesyan, S.A.; Maslakov, K.I.; Khmelnitsky, R.A.; Suetin, N. v.; et al. Ambient Condition Production of High Quality Reduced Graphene Oxide. *Advanced Materials Interfaces* **2018**, *5*, 1800737, doi:10.1002/ADMI.201800737.
133. Bondareva, J. v.; Aslyamov, T.F.; Kvashnin, A.G.; Dyakonov, P. v.; Kuzminova, Y.O.; Mankelevich, Y.A.; Voronina, E.N.; Dagesyan, S.A.; Egorov, A. v.; Khmelnitsky, R.A.; et al. Environmentally Friendly Method of Silicon Recycling: Synthesis of Silica Nanoparticles in an Aqueous Solution. *ACS Sustainable*

- Chemistry and Engineering* **2020**, *8*, 14006–14012,  
doi:10.1021/acssuschemeng.0c03783.
134. Kan, Y.; Salimon, A.I.; Korsunsky, A.M. On the Electrospinning of Nanostructured Collagen-PVA Fiber Mats. *Materials Today: Proceedings* **2020**, doi:10.1016/j.matpr.2020.07.621.
135. Starkov, V.V.; Gosteva, E.A.; Zherebtsov, D.D.; Chichkov, M.V.; Alexandrov, N.V. Nanoporous Layers and the Peculiarities of Their Local Formation on a Silicon Wafer. *Processes* **2022**, *Vol. 10, Page 163* **2022**, *10*, 163, doi:10.3390/PR10010163.
136. 126. Abdurashitov, A.S.; Proshin, P.I.; Sindeeva, O.A.; Sukhorukov, G.B. Laser Microperforation Assisted Drug-Elution from Biodegradable Films. *Pharmaceutics* **2022**, *14*, doi:10.3390/PHARMACEUTICS14102144.
137. 127. Proshin, P.I.; Abdurashitov, A.S.; Sindeeva, O.A.; Ivanova, A.A.; Sukhorukov, G.B. Additive Manufacturing of Drug-Eluting Multilayer Biodegradable Films. *Polymers (Basel)* **2022**, *14*, doi:10.3390/POLYM14204318.
138. Guan, Y.; Li, W.; Zhang, Y.; Shi, Z.; Tan, J.; Wang, F.; Wang, Y. Aramid Nanofibers and Poly (Vinyl Alcohol) Nanocomposites for Ideal Combination of Strength and Toughness via Hydrogen Bonding Interactions. *Composites Science and Technology* **2017**, *144*, 193–201, doi:10.1016/J.COMPSCITECH.2017.03.010.

139. Blaber, J.; Adair, B.; Antoniou, A. Ncorr: Open-Source 2D Digital Image Correlation Matlab Software. *Experimental Mechanics* **2015**, *55*, 1105–1122, doi:10.1007/S11340-015-0009-1.
140. Evlashin, S.A.; Svyakhovskiy, S.E.; Fedorov, F.S.; Mankelevich, Y.A.; Dyakonov, P. V.; Minaev, N. V.; Dagesyan, S.A.; Maslakov, K.I.; Khmelnskiy, R.A.; Suetin, N. V.; et al. Ambient Condition Production of High Quality Reduced Graphene Oxide. *Advanced Materials Interfaces* **2018**, *5*, 1800737, doi:10.1002/ADMI.201800737.
141. Hidayah, N.M.S.; Liu, W.W.; Lai, C.W.; Noriman, N.Z.; Khe, C.S.; Hashim, U.; Lee, H.C. Comparison on Graphite, Graphene Oxide and Reduced Graphene Oxide: Synthesis and Characterization. *AIP Conference Proceedings* **2017**, *1892*, doi:10.1063/1.5005764.
142. Zubair, N.A.; Rahman, N.A.; Lim, H.N.; Zawawi, R.M.; Sulaiman, Y. Electrochemical Properties of PVA–GO/PEDOT Nanofibers Prepared Using Electrospinning and Electropolymerization Techniques. *RSC Advances* **2016**, *6*, 17720–17727, doi:10.1039/C5RA21230H.
143. Pawar, P.B.; Shukla, S.; Saxena, S. Graphene Oxide - Polyvinyl Alcohol Nanocomposite Based Electrode Material for Supercapacitors. *Journal of Power Sources* **2016**, *321*, 102–105, doi:10.1016/j.jpowsour.2016.04.127.
144. Kim, S.-G.; Park, O.-K.; Lee, J.H.; Ku, B.-C. Layer-by-Layer Assembled Graphene Oxide Films and Barrier Properties of Thermally Reduced Graphene

- Oxide Membranes. *Carbon letters* **2013**, *14*, 247–250, doi:10.5714/CL.2013.14.4.247.
145. Heili, M.; Poumellec, B.; Burov, E.; Gonnet, C.; le Losq, C.; Neuville, D.R.; Lancry, M. The Dependence of Raman Defect Bands in Silica Glasses on Densification Revisited. *Journal of Materials Science* **2016**, *51*, 1659–1666, doi:10.1007/S10853-015-9489-8.
146. Little, D.J.; Ams, M.; Dekker, P.; Marshall, G.D.; Dawes, J.M.; Withford, M.J. Femtosecond Laser Modification of Fused Silica: The Effect of Writing Polarization on Si-O Ring Structure. *Optics Express* **2008**, *16*, 20029, doi:10.1364/OE.16.020029.
147. Spallino, L.; Vaccaro, L.; Sciortino, L.; Agnello, S.; Cannas, M.; Gelardi, F.M.; Boscaino, R. Vibronic Structures in the Visible Luminescence of Silica Nanoparticles. *AIP Conference Proceedings* **2014**, *1624*, 135–140, doi:10.1063/1.4900469.
148. Sagitova, E.A.; Prokhorov, K.A.; Nikolaeva, G.Y.; Baimova, A. V.; Pashinin, P.P.; Yarysheva, A.Y.; Mendeleev, D.I. Raman Analysis of Polyethylene Glycols and Polyethylene Oxides. *Journal of Physics: Conference Series* **2018**, *999*, 012002, doi:10.1088/1742-6596/999/1/012002.
149. Koenig, J.; Angood, A.C. Raman Spectra of Poly(Ethylene Glycols) in Solution. *Journal of Polymer Science Part A-2 Polymer Physics* **1970**, *8*, 1787–1796, doi:10.1002/POL.1970.160081013.

150. Akram, Z.; Aati, S.; Ngo, H.; Fawzy, A. PH-Dependent Delivery of Chlorhexidine from PGA Grafted Mesoporous Silica Nanoparticles at Resin-Dentin Interface. *J Nanobiotechnology* **2021**, *19*, 1–16, doi:10.1186/s12951-021-00788-6.
151. Aljabo, A.; Abou Neel, E.A.; Knowles, J.C.; Young, A.M. Development of Dental Composites with Reactive Fillers That Promote Precipitation of Antibacterial-Hydroxyapatite Layers. *Materials Science and Engineering: C* **2016**, *60*, 285–292, doi:10.1016/J.MSEC.2015.11.047.
152. Lue, S.J.; Chen, J.Y.; Yang, J.M. Crystallinity and Stability of Poly(Vinyl Alcohol)-Fumed Silica Mixed Matrix Membranes. *Journal of Macromolecular Science, Part B* **2008**, *47*, 39–51, doi:10.1080/15568310701744133.
153. Omkaram, I.; Sreekanth Chakradhar, R.P.; Lakshmana Rao, J. EPR, Optical, Infrared and Raman Studies of VO<sub>2</sub><sup>+</sup> Ions in Polyvinyl alcohol Films. *Physica B: Condensed Matter* **2007**, *388*, 318–325, doi:10.1016/J.PHYSB.2006.06.134.
154. Tretinnikov, O.N.; Zagorskaya, S.A. Determination of the Degree of Crystallinity of Poly(Vinyl Alcohol) by FTIR Spectroscopy. *Journal of Applied Spectroscopy* **2012**, *79*, 521–526, doi:10.1007/S10812-012-9634-Y.
155. Setia Budi, H.; Javed Ansari, M.; Jasim, S.A.; Kamal Abdelbasset, W.; Bokov, D.; Fakri Mustafa, Y.; Najm, M.A.A.; Kazemnejadi, M. Preparation of Antibacterial Gel/PCL Nanofibers Reinforced by Dicalcium Phosphate-Modified Graphene Oxide with Control Release of Clindamycin for Possible Application in Bone Tissue Engineering. *Inorganic Chemistry Communications* **2022**, *139*, 109336, doi:10.1016/j.inoche.2022.109336.

156. Feifel, S.C.; Lisdat, F. Silica Nanoparticles for the Layer-by-Layer Assembly of Fully Electro-Active Cytochrome c Multilayers. *Journal of Nanobiotechnology* **2011**, *9*, 59, doi:10.1186/1477-3155-9-59.
157. Morimune, S.; Nishino, T.; Goto, T. Poly(Vinyl Alcohol)/Graphene Oxide Nanocomposites Prepared by a Simple Eco-Process. *Polymer Journal* **2012**, *44*, doi:10.1038/pj.2012.58.
158. Li, C.; Lu, Y.; Yan, J.; Yu, W.; Zhao, R.; Du, S.; Niu, K. Effect of Long-Term Ageing on Graphene Oxide: Structure and Thermal Decomposition. *Royal Society Open Science* **2021**, *8*, doi:10.1098/RSOS.202309.
159. Wadhwa, H.; Kandhol, G.; Deshpande, U.P.; Mahendia, S.; Kumar, S. Thermal Stability and Dielectric Relaxation Behavior of in Situ Prepared Poly(Vinyl Alcohol) (PVA)-Reduced Graphene Oxide (RGO) Composites. *Colloid and Polymer Science* **2020**, *298*, 1319–1333, doi:10.1007/S00396-020-04718-0.
160. Zhao, H.; Wang, J.; Zhang, D.; Dai, Q.; Han, Q.; Du, P.; Liu, C.; Xie, Y.; Zhang, Y.; Cao, H.; et al. Chloro-Benquinone Modified on Graphene Oxide as Metal-Free Catalyst: Strong Promotion of Hydroxyl Radical and Generation of Ultra-Small Graphene Oxide. *Scientific Reports* **2017**, *7*, 1–11, doi:10.1038/srep42643.
161. Sanchez Ramirez, D.O.; Cruz-Maya, I.; Vineis, C.; Tonetti, C.; Varesano, A.; Guarino, V. Design of Asymmetric Nanofibers-Membranes Based on Polyvinyl Alcohol and Wool-Keratin for Wound Healing Applications. *Journal of Functional Biomaterials* **2021**, *12*, doi:10.3390/jfb12040076.

162. Zidan, H.M.; Abdelrazek, E.M.; Abdelghany, A.M.; Tarabiah, A.E. Characterization and Some Physical Studies of PVA/PVP Filled with MWCNTs. *Journal of Materials Research and Technology* **2019**, *8*, 904–913, doi:10.1016/J.JMRT.2018.04.023.
163. Judd, A.M.; Scurr, D.J.; Heylings, J.R.; Wan, K.W.; Moss, G.P. Distribution and Visualisation of Chlorhexidine within the Skin Using ToF-SIMS: A Potential Platform for the Design of More Efficacious Skin Antiseptic Formulations. *Pharmaceutical Research* **2013**, *30*, 1896–1905, doi:10.1007/S11095-013-1032-5.
164. Bryant, J.A.; Riordan, L.; Watson, R.; Nikoi, N.D.; Trzaska, W.; Slope, L.; Tibbatts, C.; Alexander, M.R.; Scurr, D.J.; May, R.C.; et al. Developing Novel Biointerfaces: Using Chlorhexidine Surface Attachment as a Method for Creating Anti-Fungal Surfaces. *Global Challenges* **2022**, *6*, 2100138, doi:10.1002/GCH2.202100138.
165. Ningaraju, S.; Ravikumar, H.B. Studies on Electrical Conductivity of PVA/Graphite Oxide Nanocomposites: A Free Volume Approach. *Journal of Polymer Research* **2016**, *24*, 1–11, doi:10.1007/S10965-016-1176-1.
166. Li, G.; Jiang, L.Y. Fabrication of Crosslinkable Hollow Fiber Membranes for Pervaporation Dehydration Article Info. *Journal of Membrane Science and Research* **2017**, *3*, 281–290, doi:10.22079/jmsr.2016.20884.
167. Zhao, S.; Tsen, W.C.; Hu, F.; Zhong, F.; Liu, H.; Wen, S.; Zheng, G.; Qin, C.; Gong, C. Layered Double Hydroxide-Coated Silica Nanospheres with 3D Architecture-Modified Composite Anion Exchange Membranes for Fuel Cell

- Applications. *Journal of Materials Science* **2020**, *55*, 2967–2983, doi:10.1007/S10853-019-04178-0.
168. Stobinski, L.; Lesiak, B.; Malolepszy, A.; Mazurkiewicz, M.; Mierzwa, B.; Zemek, J.; Jiricek, P.; Bieloshapka, I. Graphene Oxide and Reduced Graphene Oxide Studied by the XRD, TEM and Electron Spectroscopy Methods. *Journal of Electron Spectroscopy and Related Phenomena* **2014**, *195*, 145–154, doi:10.1016/J.ELSPEC.2014.07.003.
169. Aisyiyah Jenie, S.N.; Krismastuti, F.S.H.; Ningrum, Y.P.; Kristiani, A.; Yuniati, M.D.; Astuti, W.; Petrus, H.T.B.M. Geothermal Silica-Based Fluorescent Nanoparticles for the Visualization of Latent Fingerprints. *Materials Express* **2020**, *10*, 258–266, doi:10.1166/MEX.2020.1551.
170. Fakhri, A.; Feizbakhsh, A.; Kono, E.; Niazi, A. Facile Synthesis and Characterization of CoS<sub>2</sub>–SiO<sub>2</sub>/Chitosan: The Photocatalysis in Real Samples, and Antimicrobial Evaluation. *Journal of Inorganic and Organometallic Polymers and Materials* **2019**, *29*, 1119–1129, doi:10.1007/S10904-019-01074-7.
171. Gao, W.; Razavi, R.; Fakhri, A. Preparation and Development of FeS<sub>2</sub> Quantum Dots on SiO<sub>2</sub> Nanostructures Immobilized in Biopolymers and Synthetic Polymers as Nanoparticles and Nanofibers Catalyst for Antibiotic Degradation. *International Journal of Biological Macromolecules* **2018**, *114*, 357–362, doi:10.1016/J.IJBIOMAC.2018.03.119.
172. Bian, Q.; Tian, H.; Wang, Y.; Liu, Q.; Ge, X.; Rajulu, A.V.; Xiang, A. Effect of Graphene Oxide on the Structure and Properties of Poly(Vinyl Alcohol) Composite

- Films. *Polymer Science - Series A* **2015**, *57*, 836–844, doi:10.1134/S0965545X15060048.
173. Abu Hurayra–Lizu, K.M.; Bari, M.W.; Gulshan, F.; Islam, M.R. GO Based PVA Nanocomposites: Tailoring of Optical and Structural Properties of PVA with Low Percentage of GO Nanofillers. *Heliyon* **2021**, *7*, doi:10.1016/J.HELIYON.2021.E06983.
174. Li, R.; Wu, Y.; Bai, Z.; Guo, J.; Chen, X. Effect of Molecular Weight of Polyethylene Glycol on Crystallization Behaviors, Thermal Properties and Tensile Performance of Polylactic Acid Stereocomplexes. *RSC Advances* **2020**, *10*, 42120–42127, doi:10.1039/D0RA08699A.
175. Alharbi, H.F.; Luqman, M.; Fouad, H.; Khalil, K.A.; Alharthi, N.H. Viscoelastic Behavior of Core-Shell Structured Nanofibers of PLA and PVA Produced by Coaxial Electrospinning. *Polymer Testing* **2018**, *67*, 136–143, doi:10.1016/J.POLYMERTESTING.2018.02.026.
176. Yang, X.; Zhu, Z.; Liu, Q.; Chen, X. Thermal and Rheological Properties of Poly(Vinyl Alcohol) and Water-Soluble Chitosan Hydrogels Prepared by a Combination of  $\gamma$ -Ray Irradiation and Freeze Thawing. *Journal of Applied Polymer Science* **2008**, *109*, 3825–3830, doi:10.1002/APP.28436.
177. Kołodziej, A.; Długoń, E.; Świętek, M.; Ziábka, M.; Dawiec, E.; Gubernat, M.; Michalec, M.; Weselucha-Birczyńska, A. A Raman Spectroscopic Analysis of Polymer Membranes with Graphene Oxide and Reduced Graphene Oxide. *Journal of Composites Science* **2021**, *5*, doi:10.3390/jcs5010020.

178. Chew, S.Y.; Hufnagel, T.C.; Lim, C.T.; Leong, K.W. Mechanical Properties of Single Electrospun Drug-Encapsulated Nanofibres. *Nanotechnology* **2006**, *17*, 3880, doi:10.1088/0957-4484/17/15/045.
179. Wong, S.C.; Baji, A.; Leng, S. Effect of Fiber Diameter on Tensile Properties of Electrospun Poly( $\epsilon$ -Caprolactone). *Polymer (Guildf)* **2008**, *49*, 4713–4722, doi:10.1016/J.POLYMER.2008.08.022.
180. Duan, G.; Jin, M.; Wang, F.; Greiner, A.; Agarwal, S.; Jiang, S. Core Effect on Mechanical Properties of One Dimensional Electrospun Core-Sheath Composite Fibers. *Composites Communications* **2021**, *25*, 100773, doi:10.1016/J.COCO.2021.100773.
181. Pant, B.; Park, M.; Park, S.J. Drug Delivery Applications of Core-Sheath Nanofibers Prepared by Coaxial Electrospinning: A Review. *Pharmaceutics* **2019**, *11*, 305, doi:10.3390/PHARMACEUTICS11070305.
182. Zhang, X.F.; Shao, X.; Liu, S. Dual Fluorescence of Graphene Oxide: A Time-Resolved Study. *Journal of Physical Chemistry A* **2012**, *116*, 7308–7313, doi:10.1021/JP301755B.
183. Thomas, H.R.; Vallés, C.; Young, R.J.; Kinloch, I.A.; Wilson, N.R.; Rourke, J.P. Identifying the Fluorescence of Graphene Oxide. *Journal of Materials Chemistry C* **2012**, *1*, 338–342, doi:10.1039/C2TC00234E.
184. Anusavice, K.J.; Zhang, N.Z.; Shen, C. Controlled Release of Chlorhexidine from UDMA-TEGDMA Resin. *Journal of Dental Research* **2006**, *85*, 950–954, doi:10.1177/154405910608501016.

185. Shaari, H.A.H.; Ramli, M.M.; Mohtar, M.N.; Razali, N.H.F. Characterization and Conductivity of Graphene Oxide (GO) Dispersion in Different Solvents. *AIP Conference Proceedings* **2021**, 2332, 060001, doi:10.1063/5.0042911.
186. Wang, F.; Tan, J.; Zhang, S.; Zhou, Y.; He, D.; Deng, L. Efficient Eradication of Bacterial Biofilms with Highly Specific Graphene-Based Nanocomposite Sheets. *ACS Biomaterials Science and Engineering* **2021**, 7, 5118–5128, doi:10.1021/acsbmaterials.1c00575.
187. Quagliarini, E.; di Santo, R.; Pozzi, D.; Tentori, P.; Cardarelli, F.; Caracciolo, G. Mechanistic Insights into the Release of Doxorubicin from Graphene Oxide in Cancer Cells. *Nanomaterials* **2020**, 10, 1–11, doi:10.3390/nano10081482.
188. Siong, V.L.E.; Tai, X.H.; Lee, K.M.; Juan, J.C.; Lai, C.W. Unveiling the Enhanced Photoelectrochemical and Photocatalytic Properties of Reduced Graphene Oxide for Photodegradation of Methylene Blue Dye. *RSC Advances* **2020**, 10, 37905–37915, doi:10.1039/d0ra06703b.
189. Yang, S.; Yue, W.; Huang, D.; Chen, C.; Lin, H.; Yang, X. A Facile Green Strategy for Rapid Reduction of Graphene Oxide by Metallic Zinc. *RSC Advances* **2012**, 2, 8827–8832, doi:10.1039/C2RA20746J.
190. Cui, Z.; Zheng, Z.; Lin, L.; Si, J.; Wang, Q.; Peng, X.; Chen, W. Electrospinning and Crosslinking of Polyvinyl Alcohol/Chitosan Composite Nanofiber for Transdermal Drug Delivery. *Advances in Polymer Technology* **2018**, 37, doi:10.1002/ADV.21850.

191. Simon, M.A.; Anggraeni, E.; Soetaredjo, F.E.; Santoso, S.P.; Irawaty, W.; Thanh, T.C.; Hartono, S.B.; Yuliana, M.; Ismadji, S. Hydrothermal Synthesize of HF-Free MIL-100(Fe) for Isoniazid-Drug Delivery. *Scientific Reports* **2019**, *9*, 1–11, doi:10.1038/s41598-019-53436-3.
192. Mirzaie, Z.; Reisi-Vanani, A.; Barati, M.; Atyabi, S.M. The Drug Release Kinetics and Anticancer Activity of the GO/PVA-Curcumin Nanostructures: The Effects of the Preparation Method and the GO Amount. *Journal of Pharmaceutical Sciences* **2021**, *110*, 3715–3725, doi:10.1016/J.XPHS.2021.07.016.
193. Peters, J.T.; Wechsler, M.E.; Peppas, N.A. Advanced Biomedical Hydrogels: Molecular Architecture and Its Impact on Medical Applications. *Regenerative Biomaterials* **2021**, *8*, 1–21, doi:10.1093/RB/RBAB060.
194. Kong, B.; Liu, R.; Guo, J.; Lu, L.; Zhou, Q.; Zhao, Y. Tailoring Micro/Nano-Fibers for Biomedical Applications. *Bioactive Materials* **2023**, *19*, 328–347, doi:10.1016/J.BIOACTMAT.2022.04.016.
195. Severyukhina, A.N.; Petrova, N. V.; Smuda, K.; Terentyuk, G.S.; Klebtsov, B.N.; Georgieva, R.; Bäumlner, H.; Gorin, D.A. Photosensitizer-Loaded Electrospun Chitosan-Based Scaffolds for Photodynamic Therapy and Tissue Engineering. *Colloids and Surfaces B: Biointerfaces* **2016**, *144*, 57–64, doi:10.1016/j.colsurfb.2016.03.081.
196. Rostamitabar, M.; Abdelgawad, A.M.; Jockenhoevel, S.; Ghazanfari, S. Drug-Eluting Medical Textiles: From Fiber Production and Textile Fabrication to Drug

- Loading and Delivery. *Macromolecular Bioscience* **2021**, *21*, 2100021, doi:10.1002/MABI.202100021.
197. Merkle, V.M.; Tran, P.L.; Hutchinson, M.; Ammann, K.R.; Decook, K.; Wu, X.; Slepian, M.J. Core-Shell PVA/Gelatin Electrospun Nanofibers Promote Human Umbilical Vein Endothelial Cell and Smooth Muscle Cell Proliferation and Migration. *Acta Biomaterials* **2015**, *27*, 77–87, doi:10.1016/J.ACTBIO.2015.08.044.
198. Merkle, V.M.; Zeng, L.; Slepian, M.J.; Wu, X. Core-Shell Nanofibers: Integrating the Bioactivity of Gelatin and the Mechanical Property of Polyvinyl Alcohol. *Biopolymers* **2014**, *101*, doi:10.1002/bip.22367.
199. Sutka, A.; Sutka, A.; Gaidukov, S.; Timusk, M.; Gravitis, J.; Kukle, S. Enhanced Stability of PVA Electrospun Fibers in Water by Adding Cellulose Nanocrystals. *Holzforschung* **2015**, *69*, doi:10.1515/hf-2014-0277.
200. Song, W.; Markel, D.C.; Wang, S.; Shi, T.; Mao, G.; Ren, W. Electrospun Polyvinyl Alcohol-Collagen-Hydroxyapatite Nanofibers: A Biomimetic Extracellular Matrix for Osteoblastic Cells. *Nanotechnology* **2012**, *23*, doi:10.1088/0957-4484/23/11/115101.
201. Chen, Z.; Jiang, Y.; Xin, B.; Jiang, S.; Liu, Y.; Lin, L. Electrochemical Analysis of Conducting Reduced Graphene Oxide/Polyaniline/Polyvinyl Alcohol Nanofibers as Supercapacitor Electrodes. *Journal of Materials Science: Materials in Electronics* **2020**, *31*, doi:10.1007/s10854-020-03204-1.

202. Kang, D.; Shin, Y.E.; Jo, H.J.; Ko, H.; Shin, H.S. Mechanical Properties of Poly(Dopamine)-Coated Graphene Oxide and Poly(Vinyl Alcohol) Composite Fibers Coated with Reduced Graphene Oxide and Their Use for Piezoresistive Sensing. *Particle and Particle Systems Characterization* **2017**, *34*, doi:10.1002/ppsc.201600382.
203. Zhu, H.; Gao, W.; Yan, S.; Niu, M.; Liu, G.; Hao, H. Electrospun Poly(Vinyl Alcohol) Sub-Micron Fibers Containing Superfine Diatomite for Dye Adsorption. *Materials Chemistry and Physics* **2019**, *234*, doi:10.1016/j.matchemphys.2019.03.044.
204. Boschetto, F.; Doan, H.N.; Vo, P.P.; Zanicco, M.; Zhu, W.; Sakai, W.; Adachi, T.; Ohgitani, E.; Tsutsumi, N.; Mazda, O.; et al. Antibacterial and Osteoconductive Effects of Chitosan/Polyethylene Oxide (PEO)/Bioactive Glass Nanofibers for Orthopedic Applications. *Applied Sciences (Switzerland)* **2020**, *10*, doi:10.3390/app10072360.
205. Sasipriya, K.; Suriyaprabha, R.; Prabu, P.; Rajendran, V. Synthesis and Characterisation of Polymeric Nanofibers Poly (Vinyl Alcohol) and Poly (Vinyl Alcohol)/Silica Using Indigenous Electrospinning Set Up. *Materials Research* **2013**, *16*, doi:10.1590/S1516-14392013005000050.